PUMPING CHAMBER DESIGN IN DIODE-PUMPED SOLID-STATE LASERS FOR
MAXIMUM SYSTEM EFFICIENCY AND MINIMUM OPTICAL DISTORTION

A THESIS SUBMITTED TO
THE GRADUATE SCHOOL OF NATURAL AND APPLIED SCIENCES
OF
MIDDLE EAST TECHNICAL UNIVERSITY

BY

KUBİLAY SEZGİN

IN PARTIAL FULFILLMENT OF THE REQUIREMENTS
FOR
THE DEGREE OF MASTER OF SCIENCE
IN
ELECTRICAL AND ELECTRONICS ENGINEERING

JANUARY 2013

Approval of the thesis:

PUMPING CHAMBER DESIGN IN DIODE-PUMPED SOLID-STATE LASERS FOR MAXIMUM SYSTEM EFFICIENCY AND MINIMUM OPTICAL DISTORTION

submitted by **KUBİLAY SEZGİN** in partial fulfillment of the requirements for the degree of **Master of Science in Electrical and Electronics Engineering Department, Middle East Technical University** by,

Prof. Dr. Canan Özgen   _____
Dean, Graduate School of **Natural and Applied Sciences**

Prof. Dr. İsmet Erkmen   _____
Head of Department, **Electrical and Electronics Engineering**

Prof. Dr. Gönül Turhan Sayan   _____
Supervisor, **Electrical and Electronics Engineering Dept., METU**

Dr. Kuthan Yelen   _____
Co-Supervisor, **ASELSAN**

Examining Committee Members:

Prof. Dr. Gülbin Dural   _____
Electrical and Electronics Engineering Dept., METU

Prof. Dr. Gönül Turhan Sayan   _____
Electrical and Electronics Engineering Dept., METU

Prof. Dr. Mete Severcan   _____
Electrical and Electronics Engineering Dept., METU

Dr. Kuthan Yelen   _____
ASELSAN

Dr. Oktay Onur Kuzucu   _____
ASELSAN

Date: 18.01.2013

I hereby declare that all information in this document has been obtained and presented in accordance with academic rules and ethical conduct. I also declare that, as required by these rules and conduct, I have fully cited and referenced all material and results that are not original to this work.

Name, Last Name :   Kubilay Sezgin

Signature   :

ABSTRACT

PUMPING CHAMBER DESIGN IN DIODE-PUMPED SOLID-STATE LASERS FOR MAXIMUM SYSTEM EFFICIENCY AND MINIMUM OPTICAL DISTORTION

Sezgin, Kubilay

M.S., Electrical and Electronics Engineering

Supervisor   : Prof. Dr. Gönül Turhan Sayan

Co-Supervisor   : Dr. Kuthan Yelen

January 2013, 85 pages

The beam quality and the system efficiency of a diode-pumped solid-state laser source are directly related to the thermal profile inside the laser crystal. The thermal profile in a laser crystal should be made uniform in order to reduce the negative effects of the thermal lens. However, the absorbed pump profile that forms a uniform thermal profile inside the gain medium may adversely affect the system efficiency. In this thesis, a computational and empirical method was developed for designing pumping chambers that results in a suitable thermal profile inside the gain medium, and thus desired laser beam quality was achieved while keeping the system efficiency at an acceptable level. Accomplishment of this thesis work will lead to the design of pumping chambers and resonators in high power laser systems operating at even higher thermal loads.

Keywords: Diode-Pumped Solid-State Laser, Pump Chamber Design in Solid-State Lasers, Laser Crystal, Thermal Lens, Laser Beam Quality

ÖZ

DİYOT POMPALI KATI HAL LASERLERİNDE MAKSİMUM VERİM VE MİNİMUM OPTİK BOZULMA SAĞLAYACAK POMPA ODASI TASARIM KRİTERLERİ VE METODU

Sezgin, Kubilay

Yüksek Lisans, Elektrik ve Elektronik Mühendisliği

Tez Yöneticisi   : Prof. Dr. Gönül Turhan Sayan

Ortak Tez Yöneticisi : Dr. Kuthan Yelen

Yandan diyot pompalı bir katı hal laser kaynağında ışın kalitesi ve sistem verimliliği, laser kristali içerisinde oluşan ısı dağılım profiliyle doğrudan ilişkilidir. Isı yükünden kaynaklanan odaklanmanın istenmeyen etkilerini azaltmak için laser kristali içerisinde oluşan ısı profili düzgün olmalıdır. Ancak bu düzgün ısı profilini oluşturacak, laser kristali içerisinden geçen pompa profili sistem verimliliğini negatif yönde etkileyebilir. Bu tezde, kazanç ortamında istenilen seviyede ısı profili, laser kaynağı çıkışında istenilen seviyede ışın kalitesi ve aynı zamanda istenilen seviyede sistem verimliliğini sağlayacak pompa odası tasarımı için hesaplamalı ve deneysel bir yöntem geliştirilmiştir. Bu tezin başarımı sayesinde, çok yüksek ısı yüküne maruz kalan yüksek güçlü laser sistemlerinin pompa odası ve rezonatör tasarımları gerçekleştirilecektir.

Anahtar Kelimeler: Diyot-Pompalı Katı-Hal Laseri, Katı-Hal Laserlerinde Pompa Odası Tasarımı, Laser Kristali, Thermal Lens, Laser Işın Kalitesi

to my family…

AKNOWLEDGEMENTS

TABLE OF CONTENTS

LIST OF TABLES

TABLES

LIST OF FIGURES

FIGURES

ABBREVIATIONS

LASER	Light Amplification by Stimulated Emission of Radiation
Nd:YAG	Neodymium-Doped Yttrium Aluminum Garnet; $Nd:Y_3Al_5O_{12}$
OPD	Optical Path Difference
HR	High Reflective
PR	Partial Reflective
AR	Anti Reflection
GLAD	(General Laser Analysis and Design) Laser and physical optics software
ZEMAX	Optical Design and Analysis Software
MATLAB	Programming environment for algorithm development and numerical computation
CFD	Computational Fluid Dynamics
FLUENT	A software to model and analyze flow, turbulence, heat transfer and reactions
CCD	Charge – Coupled Device
PIN Diode	A diode with a wide, lightly doped 'near' intrinsic semiconductor region between a p-type and an n-type semiconductors region
IR	Infrared
ORIGIN	Proprietary computer program for interactive scientific graphing and data analysis
OD(E)	Optical Density
TEC	Thermo – Electric Cooler
CAD	Computer Aided Design
TIR	Total Internal Reflection
He-Ne	Helium – Neon (Laser)

SYMBOLS

B_{12}	Stimulated Absorption Constant – Einstein B Coefficient
A_{21}	Spontaneous Emission Constant – Einstein A Coefficient
B_{21}	Stimulated Emission Constant – Einstein B Coefficient
k	Thermal Conductivity
n	Refractive Index
α	Linear Expansion Coefficient
dn/dT	Temperature Coefficient of Refractive Index
n_q	Quantum Yield (Efficiency)
η_H	Thermal Loading Coefficient
$N0$	Ground Level Ion Density
N_d	Doped Ground Level Ion Density
τ_{XY}	Transition Duration From X to Y
hv	Energy of a Photon
$\sigma_a\ \lambda$	Wavelength Dependent Absorption Cross Section
$\sigma_{a,eff}\ \lambda$	Wavelength Dependent Effective Absorption Cross Section
$\alpha\ \lambda$	Wavelength Dependent Absorption Coefficient
$\alpha_{eff}\ \lambda$	Wavelength Dependent Absorption Coefficient
ψ	Uniformity Term

CHAPTER 1

INTRODUCTION

1.1. Historical Progression of Diode Pumped Solid State Laser

Historically, laser researches began after the invention of stimulated amplification techniques used in microwave region. Arthur Schawlow and Charles Townes proposed utilizing maser idea for optical frequencies in 1958 [1]. The proper material, a pink ruby crystal, for lasing action was first found by Ted Maiman in 1960 and thus laser was invented by means of a solid state crystal [2]. Cylindrical ruby crystal was pumped by a flash lamp optically. The efficiency of implemented laser source was very low. Therefore after the invention of the first laser, lots of studies carried out to discover other materials for the gain medium. In a short time, lasing with other solids, gases, liquids and semiconductors with higher efficiencies was demonstrated. The most efficient active medium that is neodymium doped yttrium aluminum garnet, Nd:YAG, was discovered by Joseph Geusic and Richard Smith in 1964. Because the growth of Nd:YAG crystal is easier than other solids, and also it has a low threshold value, good optical, mechanical and thermal properties, it has been the most widely used solid state active medium since 1964. The system efficiency of the laser source with Nd:YAG crystal as the active medium was measured 10 times greater than that of ruby crystal.

By the improvement in epitaxial processes and junction structure of semiconductor devices laser diodes with high output power have became available commercially in the mid 1980s. The narrow band emission spectrum of laser diodes and the spectral match with absorption spectrum of solid state crystals increased system efficiency and reduced thermal load of the active medium. Pumping with laser diodes also results with more reliable and compact laser sources. However, since that time laser diodes have been very expensive as compared to flash lamps. Still the progression and evolution of laser diodes are going on in order to reduce the cost and increase the performance of laser diodes.

1.2. The Problem and Objective of the Present Study

In this study, the gain medium was pumped by laser diode-stacks. The general view of the laser diode-stack that was used throughout the study is shown in Figure 1.1. It has 7 laser diode-arrays each containing 40 emitters as shown in Figure 1.2 which shows emission at the near-field.
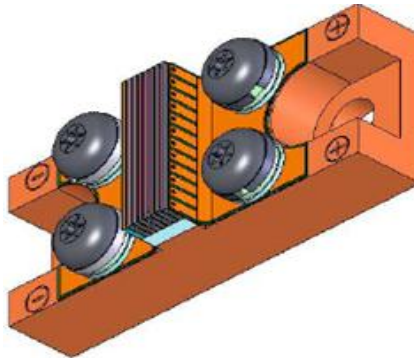
Figure 1.1: Laser Diode-Stack
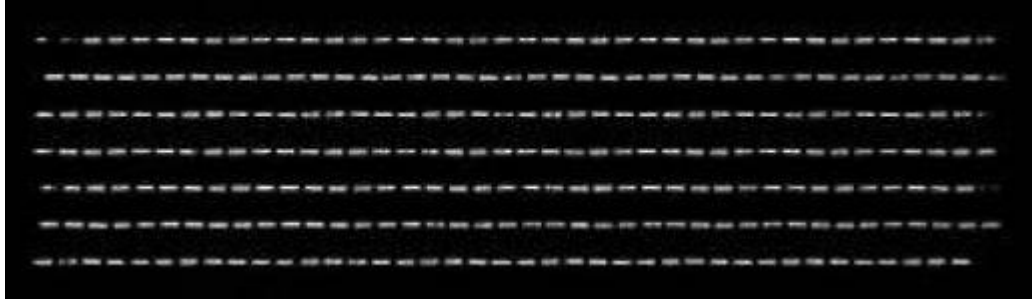
Figure 1.2: The Near-Field View of Laser Diode Array

Unless otherwise specified, the global coordinate axes will be as given in Figure 1.3 throughout this study. The dimensions of the crystal on x, y and z axes are called b, c, a, respectively.
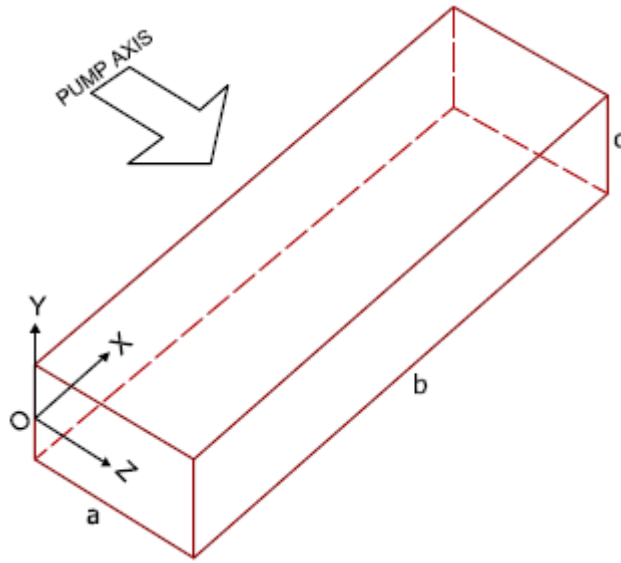
Figure 1.3: Global Coordinate Axes

In a laser diode-emitter, the emitting aperture on the horizontal (x-axis) is much greater than the emitting aperture on the vertical (y-axis) as demonstrated in Figure 1.4. Therefore, the divergence angle on the vertical is greater than the divergence angle on the horizontal axis. Because of this fast diverging, y-axis is called "fast-axis", whereas the x-axis is called "slow-axis" in the literature.
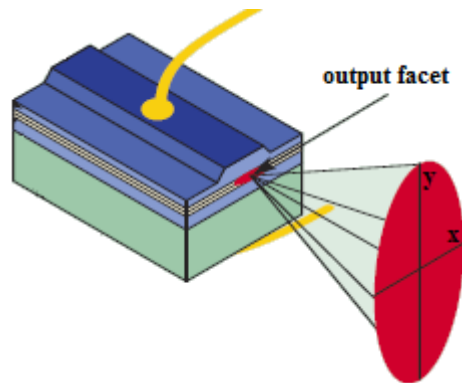
Figure 1.4: Emission from a Laser Diode-Emitter [3]

In a solid-state laser, if the gain medium is pumped with a laser diode-stack that includes emitters, a nonuniform pumping profile is formed on the fast-axis because of high divergence angle. Nonuniform pumping of the gain medium results in a nonuniform heat distribution across the crystal. Thus

2

temperature differences are induced between the regions inside the gain medium commensurate with the pump power density. As a result of this nonuniform temperature profile, the refractive index of the crystal varies inside the crystal and also the axial length of the crystal varies because of thermal expansion. Therefore the temperature differences results in a nonuniform optical path inside the crystal. Transverse optical path variation due to thermally induced refractive index change is called "thermal lens". Associated with the thermal differences are also stresses in the active material that lead to birefringence which is simply the dependency of the refractive index to the incident field polarization. All these negative effects distort the wavefront of the laser beam, introduce strong optical aberrations on the beam and depending on the induced thermal lens they causes the laser beam to diverge or focus as it emerges from the system.

For instance, a single-array one-side diode-pumped solid-state laser, as shown in Figure 1.5, yield a pump distribution on the y-axis as shown in Figure 1.6 and Figure 1.7 at the entrance surface of the crystal. The shape of given pump profile is conserved across the crystal even the beam width may vary.
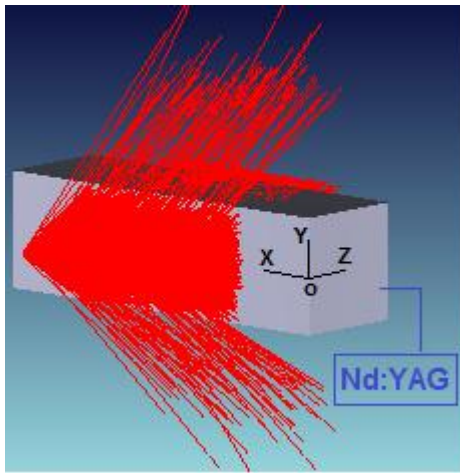
Figure 1.5: Side Pumped Model
(Red Lines Represents Pump Beams)
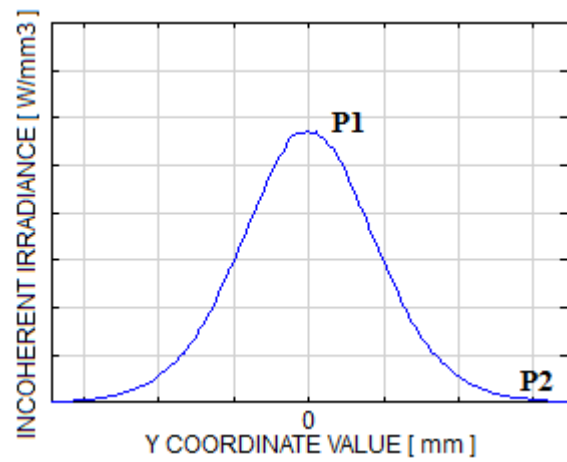
Figure 1.6: Y Axis Pump Profile on Z = 0
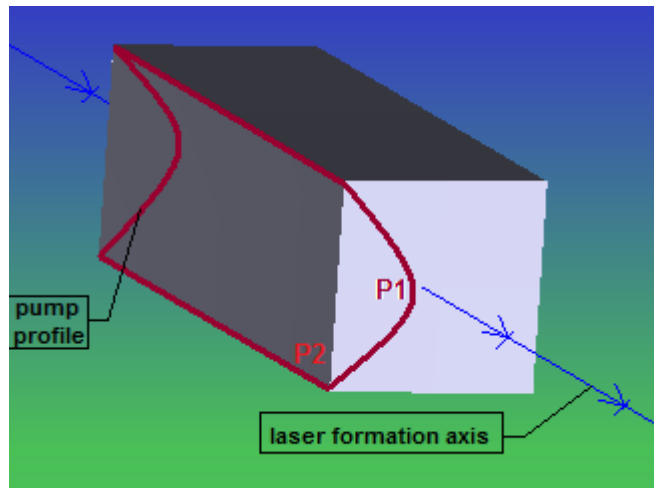
Figure 1.7: Y Axis Pump Profile along Z > 0 Inside the Crystal, P1 > P2

This nonuniform pumping causes a nonuniform temperature distribution as shown in Figure 1.8 which results in a nonuniform refractive index profile as given in Figure 1.9. As a result of this nonuniform refractive index, a positive thermal lens along the laser formation axis is induced, distorting the laser beam.

3

Uniform temperature distribution inside the crystal leads to uniform beam shape and better beam quality with low beam divergence. However, there is a quadratic relationship between the pump profile and generated temperature distribution inside the crystal. That means, a uniform temperature profile across the crystal can be obtained by pumping the gain medium with a nonuniform pump profile. Such a pump distribution adversely affects the system efficiency since it causes a nonuniform gain profile across the crystal. The objective is to obtain an optimum point to maximize the overall system efficiency and the beam quality together. In other words, the intention is to characterize and optimize the pump and temperature distributions across the gain medium to obtain desired system efficiency and beam quality simultaneously. To this end, one needs to characterize the laser diodes to obtain the spatial pump variation, compute temperature distribution across the gain medium and calculate resulting beam distortion and beam divergence resulting from the thermal lens. Thus one can design a pump chamber that gives the desired thermal profile across the gain medium and reduce the optical distortions and beam divergence. A pump chamber is a structure that includes; the pump source, the gain medium and transferring optical part between the pump source and the gain medium. In this study, the computational methods for the aforementioned parameters are introduced, followed by the analysis based on a computer aided pump chamber design. All computational methods were verified experimentally.
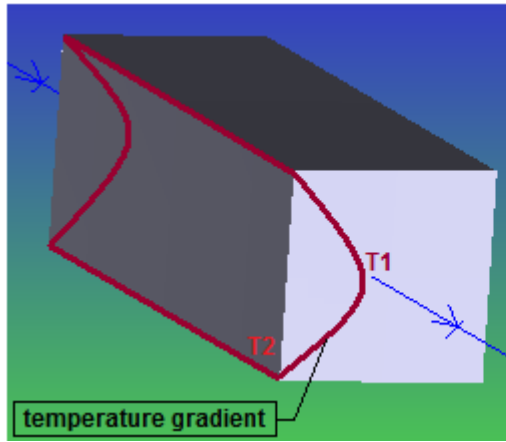
Figure 1.8: Y Axis Temperature Distribution along Z > 0 Inside the Crystal, T1 > T2   Figure 1.9: Y Axis Refractive Index Profile along Z > 0 Inside the Crystal, n1 > n2
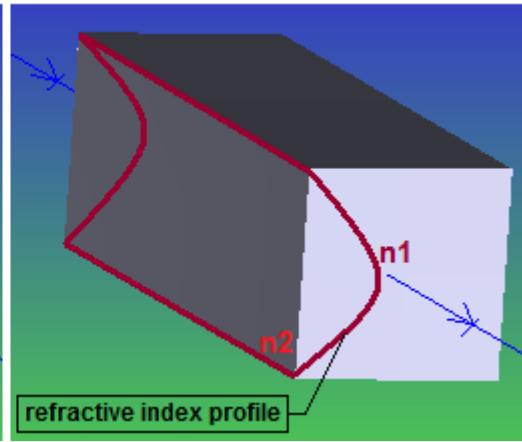
1.3. Literature Survey on the Present Study

There are various studies to obtain a uniform pump distribution by a special design of pump chamber leading to constant gain coefficient across the crystal and increased overall system efficiency. There are also other studies to investigate temperature distribution inside the gain medium and make the temperature distribution uniform to suppress thermo-optical effects and obtain maximum beam quality, as will be mentioned below.

In literature, thermo-optical distortions have been investigated usually in terms of thermal lensing, thermally induced birefringence and wavefront distortions. Some studies aimed to find the ways to get a uniform temperature distribution across the gain medium and get rid of thermo-optical effects. Rotating the gain medium in pulsed solid state lasers to pump different sides at each time was reported in a variety of studies that are summarized and specialized with a simple technique in [4]. The reason for rotating the crystal with respect to the laser formation axis is to increase pump volume and thermal fractional loading, spread out heat generation and obtain more uniform temperature profile inside the crystal. In another study, thermally-induced aberration of approximately two waves was measured and corrected by a diffractive optic element inside the cavity. As a result, single-mode slope efficiency increased by a factor of 4 [5].

The effort in some studies is to calculate and measure thermo optical effects inside the gain medium. For instance, in [6] thermo-optical distortions of a solid state crystal ($Nd:YVO_4$) of a side-diode-pumped solid-state laser was investigated. The mathematical model of thermal lensing was developed and experimentally tested with a wavefront analyzer. In another study, thermally induced

birefringence was measured with a highly sensitive polarimeter [7]. In another study, thermo-optical distortions in a slab geometry of Nd:YAG with a zigzag beam propagation was measured. Heat distribution along the active medium was obtained by an interferometric technique and the effect of homogenous heat distribution on the wavefront was observed [8]. In another study, thermal management in different kinds of solid-state crystals in diode-pumped models was studied and some measurement techniques, were investigated [9].

In order to calculate temperature distribution inside the gain medium analytically or numerically one should know a coefficient called "fractional thermal loading coefficient", η_H, that is the generated heat power out of absorbed pump power. In literature different approaches to calculate this parameter were reported. Laser calorimetry was used to extract η_H in [10] for Nd:YAG and Yb:YAG, where thermal load for 1.04% doped Nd:YAG was reported between 0.37-0.43. In another study, an interferometric measurement method was proposed and η_H was calculated as 0.53 for flashlamp pumping of Q-switched 1.1% doped Nd:YAG [11]. In another study, η_H was calculated for miniature solid state laser by stability quenching method [12]. In this thesis η_H was calculated in a practical way that has not been reported before. The parameter was adjusted so that measured transient temperature profiles by a thermal camera and numerically calculated transient temperature distributions were matched.

There are also various studies reported in literature for maximizing transfer efficiency between laser diodes and active medium, and also for developing pumping chambers as a result of which the gain medium is pumped uniformly. Different side-pumped configurations for diode-pumped solid-state lasers with 1% doped Nd:YAG rod were compared in [13] in terms of uniformity and absorption efficiency. In another study, a side-pumping design to maximize system efficiency using a micro-lens-free laser diode stacks has been shown [14]. In another study, modeling of both end-pumped and side diode-pumped configurations was studied. Both analytical and ray tracing methods in Non-Sequential Part of ZEMAX, which is an optical design and analysis software, were used to analyze the absorbed pump distributions to maximize the transfer efficiency [15]. ZEMAX software was used also in our study to get the desired pump profiles across the gain medium. In another study, a model was developed for optimizing the pumping geometry in a side-diode-pumped laser. A ray tracing algorithm was used to obtain absorbed pump distribution in the gain medium. Analytical and numerical results were given for a single mode laser output resulting from a few examples of Gaussian pumping [16].

As a result, besides the given studies in which the transfer efficiency was increased or thermal lens effect was reduced, this study will be a reference for optimizing both temperature and pump distributions together across the gain medium in order to design a pump chamber for maximizing both the transfer efficiency and beam quality.

1.4. The Outline of the Present Study

In this study, various criteria that should be considered in the diode-pumped solid-state laser design will be examined with numerical and analytical computations and empirical measurements. And then by using these findings, a computer-aided pump chamber design for this kind of lasers will be studied. Throughout the study, 1.1% doped Nd:YAG crystal in slab geometry will be used as the gain medium and will be longitudinally pumped with 5 serially connected laser diode-stacks of the same model as given in Figure 1.10.
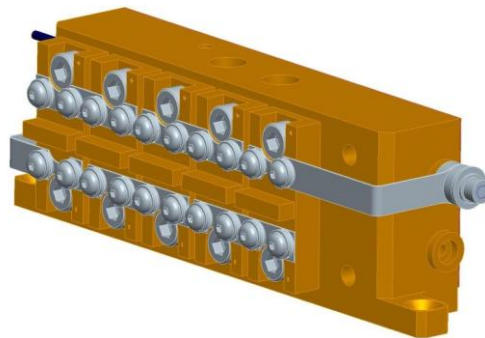
Figure 1.10: Five Serially Connected Laser-Diode Stacks

5

The outline for this study is as follows:

1. An experimental method was developed to characterize the laser diode stacks in terms of the beam profile and beam divergence in fast and slow axes. Then, by using this method, laser diode-stacks were characterized in terms of beam profile at different positions. The dependency of the beam profiles with respect to repetition rate and the applied current value to the laser diode-stack were also investigated. Finally the absorption of the laser crystal was investigated as a function of the laser diode-stack temperature and the optimum working temperature of the diode-stack was obtained.

2. The amount of generated heat power out of the absorbed pump power inside the gain medium was calculated. Towards this end, the crystal was side pumped with a laser diode-stack of which beam profile at any distance in the air or in the gain medium was known from the previous step. Then the thermal images with thermographic data of the crystal cross section were recorded by means of a thermal camera as a function of time. Later on, the absorbed pump power in the gain medium was calculated and the temperature profile simulations by CFD (Computational Fluid Dynamics) method were carried out in FLUENT software by using the obtained beam divergence and pump profiles from the previous step. The results of the simulations were compared to the thermographic data to find the percentage of generated heat power out of the absorbed pump power by the gain medium. This coefficient enabled us to calculate the temperature distribution inside the crystal for any given pump beam profile. From this temperature distribution, the refractive index variation inside the crystal and the wavefront aberrations on the laser beam was calculated.

   In optically pumped laser, the wavelength of an emitted laser photon is longer than the wavelength of an absorbed pump photon. Therefore, the energy of a pump photon is greater than the energy of a laser photon. This difference in photon energies is called "quantum defect" and formulated by;

   $$q = h\nu_{pump} - h\nu_{laser} = h\nu_{pump}. \ \left(1 - \frac{h\nu_{laser}}{h\nu_{pump}}\right)$$

   $$= h\nu_{pump}. \ \left(1 - \frac{\lambda_{pump}}{\lambda_{laser}}\right) \tag{1.1}$$

   For Nd:YAG crystal that is pumped at 808nm and operating at 1064nm, the equation 1.1 becomes;

   $$q = h\nu_{pump} \ \left(1 - \frac{\lambda_{pump}}{\lambda_{laser}}\right) \ = \ \left(1 - \frac{808nm}{1064nm}\right) \ \cong 0.24 \times h\nu_{pump} \tag{1.2}$$

   That means at least 24% of the absorbed pump energy will be lost as heat energy in any case because of the quantum defect. Since there will be heat generation in also non-radiative transitions, we expect that the generated heat energy out of absorbed pump energy, namely thermal loading coefficient will be greater than 24%.

3. In this step, a pump chamber design will be investigated in an optical design software, ZEMAX. There is a quadratic relationship between the pump profile and the temperature distribution formed inside the crystal as a result of that pump profile. And in a laser source the crystal should be cooled down by means of a heat sink. Designed heat sink structure also introduces thermal variation inside the crystal. Therefore obtaining a uniform temperature profile across the crystal is not a simple task. Pumping the gain medium with a top hat pump profile is one of the best choices for this study in order to show the improvement in thermal lens and beam divergence. Therefore, a pump chamber that results in a top hat pump profile across the gain medium on the pump axis was designed. The design was implemented by using a laser diode-stack whose near-field emission profile was found in step 1. In this design, the generated heat energy inside the crystal was removed from top and bottom planes symmetrically.

After manufacturing the laser source together with the designed pump chamber, the resulting design was analyzed computationally and empirically. The temperature distribution across the crystal for this kind of pump profile was computed numerically in chapter 2.2.1 by means of the verified thermal loading coefficient. Temperature distribution was also obtained by means of a thermal camera. The calculated results were then fitted to the experimental data in order to observe the agreement.

Thermal lens radius and the resulting laser beam divergence were also calculated for this pump profile as described in 2.2.1. A reference top hat laser beam in 633nm was passed through the gain medium while pumping continues without the resonator. The beam radius on the reference beam was observed by means of a wavefront analyzer as shown in Figure 1.11. Then the resonator of the design was formed to get 1064nm laser beam emission and the emitted laser beam divergence was measured by using a CCD camera at the far-field. Finally, both the measured thermal lens radius and the laser beam divergence values were compared to the computed ones in order to see the improvement.
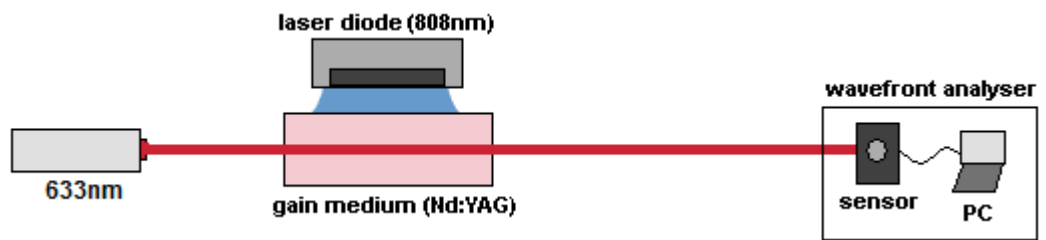
Figure 1.11: The Setup for Observing Wavefront Distortion Experimentally

THEORETICAL DEFINITON OF THE PROBLEM

2.1. Components and Operating Principles of a Solid-State Laser

A typical diode-pumped solid-state laser system consists of three major components as shown in Figure 2.1. These are namely:

- A pumping (stimulating) mechanism which is the laser diode
- An active medium (gain medium) which is a solid-state crystal doped with an active ion that exhibits a suitable laser transition
- And a feedback mechanism consisting of two mirrors; one is high reflector and the other one is partial reflector or sometimes called output coupler.
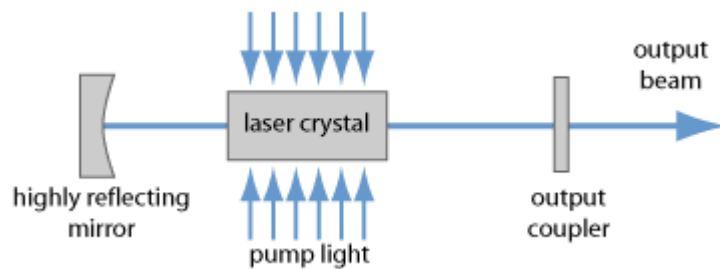
Figure 2.1: Elements of a Diode-Pumped Solid-State Laser [17]

The function of these elements is based on three fundamental processes; stimulated absorption or simply "absorption", spontenous emission and stimulated emission that take place within light-matter interaction. In absorption process, there is an upward transition between energy states E1 and E2 of the active medium as given in Figure 2.2. An atom or a molecule at the energy state E1 absorbs the incoming wave of which energy is E2-E1 and then jumps to the upper energy state E2.

Figure 2.2: The Illustration of Absorption Process

In the spontaneous emission process, an excited atom at an upper energy state E2 spontaneously relaxes down to a lower energy state E1 and emits a photon of which energy is again the energy difference between the levels as given in Figure 2.3.

In the stimulated emission process, emission of a photon is induced externally. An atom at an upper energy level E2 is excited by the incoming wave with the energy equal to E2-E1 spacing in Figure 2.4 and then relaxes down to a lower energy state E1 by emitting a photon of which phase, frequency and direction are exactly the same as the incoming wave.

Figure 2.3: The Illustration of Spontaneous Emission Process
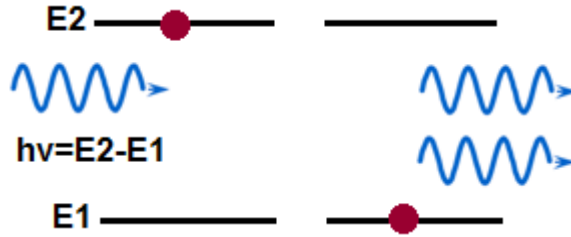
Figure 2.4: The Illustration of Stimulated Emission Process

The word "LASER" stems from the first letters of the sentence "Light Amplification by Stimulated Emission of Radiation". The sentence describes an amplification process of electromagnetic radiation by stimulated emission which provides coherent and directional emission that are the most important properties of a laser source. Operating principle of a laser source is based on the given three processes and their probabilities to occur. These processes were first derived by Albert Einstein with the related constants B_{12}, A_{21}, B_{21} in the light matter interaction. Among these processes, stimulated emission is the only one that provides equivalent energy, direction, phase and polarization of amplified photons. The active medium is pumped to get a population difference between an energetically higher excited state and a lower excited state among which lasing occurs. This phenomenon is called population inversion and increase the probability of stimulated emission. The gain medium is placed in a resonator, namely an optical oscillator that is composed of two reflective mirrors one of which is utilized as an output coupler. By means of the resonator, radiation field is redirected into the gain medium. Thus the probability of stimulated emission is increased as compared to the probability of spontaneous emission over the geometrical orientation that is defined by the resonator axis, and the emitted photons by stimulated emission are amplified in the resonator to exceed laser threshold.

In this study, Nd:YAG (Neodymium Yttrium Aluminum Garnet) will be used as the active medium. YAG is the host material which is doped with Nd^{3+} ions. Nd^{3+} ions have four energy levels shown in Figure 2.5. Ground level of the energy states, $I_{9/2}$ consists of five sublevels whereas pump band, $F_{5/2}$ consists of seven sublevels. The lasing process is depicted in Figure 2.6. Nd^{3+} atoms at ground level E0 ($I_{9/2}$) absorb the incoming pump energy around 808nm and jump to the upper energy state E3 ($F_{5/2}$). And then by radiating heat energy via electron-phonon scattering, the atoms quickly relax down to the metastable state E2 ($F_{3/2}$) which forms the upper state of the laser transition. Emission processes occur between the energy states E2 and E1 ($I_{11/2}$). The most common lasing transition for Nd:YAG is between $F_{3/2}$ and $I_{11/2}$ energy states by stimulated emission that results an emitted wave around 1064nm. Then the atoms at E1 relax down to the ground level E0 by again radiating heat energy. And the emitted photons between the energy states E2 and E1 are amplified in the resonator.

2.2. The Problem in Depth

The optical distortions on a laser beam stem from the thermal nonuniformity and stress inside the crystal. In the following example, a uniform top hat, and a nonuniform pump distributions will be compared in terms of their effect on the thermal lens and beam divergence. First, the analytical

calculation of the temperature distribution inside the crystal due to the absorbed pump power will be given for both pump profiles. Then, the optical path difference (OPD) will be calculated as a result of temperature distribution on the fast-axis. After OPD calculation, the radius of thermal lens will be calculated. And finally the effect of the thermal lens radius on the beam divergence at far-field will be investigated.
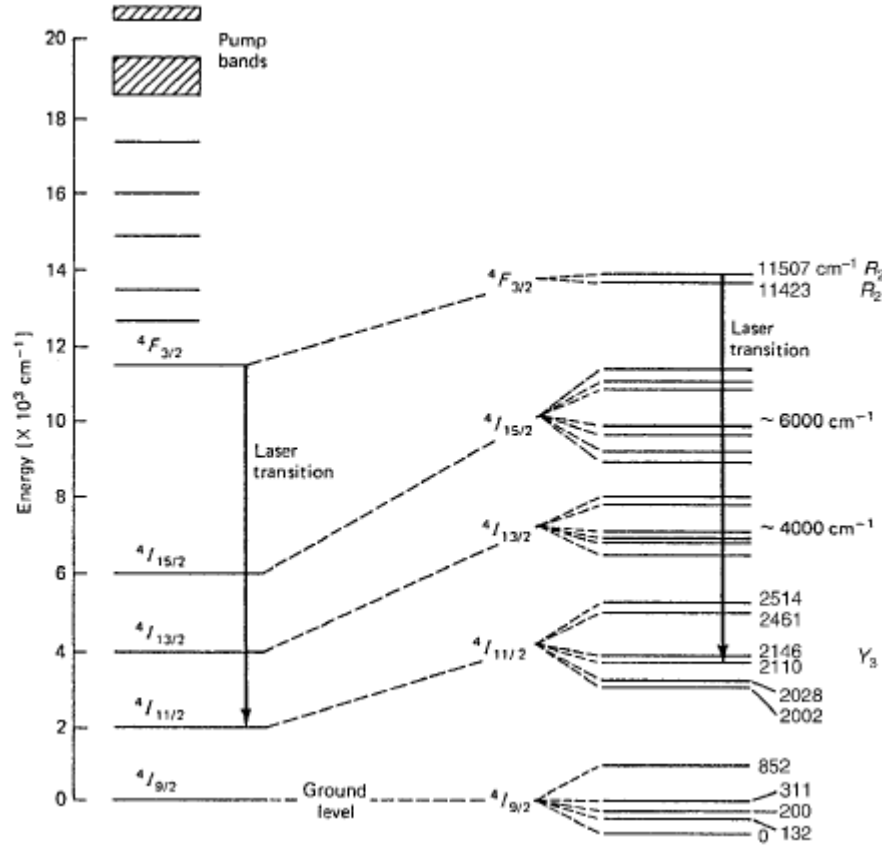
Figure 2.5: Energy Levels of Nd^{3+} ion in a YAG Crystal [18]
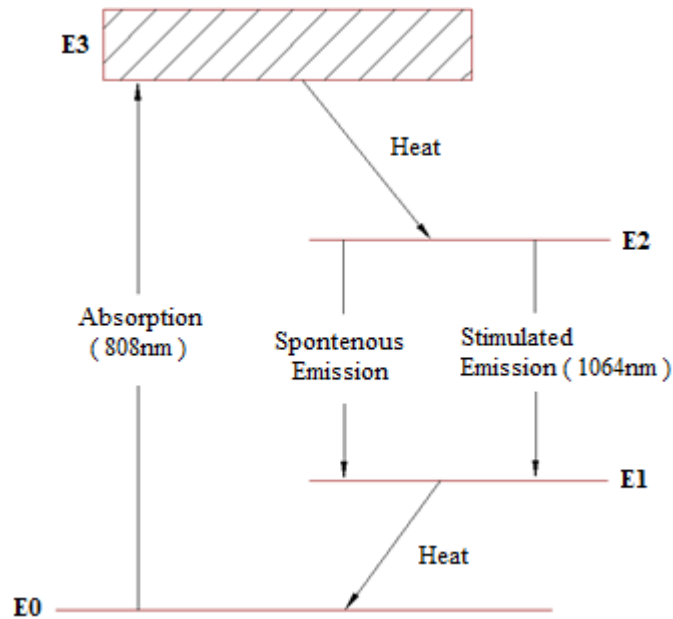
Figure 2.6: The Four Level Energy Scheme

2.2.1. Analytical Calculation of Temperature Distribution inside the Crystal as a result of Absorbed Pump Power

Temperature profile inside the gain medium as a result of the absorbed pump power can be calculated by means of heat conduction equation. For simplicity and solving the equation analytically, one dimensional problem will be studied using one dimensional heat conduction equation which has the well known form [19] ;

$$\frac{\partial^2 T(y)}{\partial y^2} + \frac{g(y)}{k} = 0 \qquad (2.1)$$

where $g(y)$ is heat generation distribution which is related to the absorbed pump power. And k is the thermal conductivity of Nd:YAG crystal, i.e. $k = 0.13 \, W/°C \times cm$.

Temperature differences inside the crystal will be derived for the fast-axis, shown with a red line in Figure 2.7, at a fixed position on the x and z axes. The computation will be studied at the proximity of the entrance surface, as given with the red line in the figure, since the heat load is maximum at the entrance of the crystal because of high absorbed power (See Figure 4.17).
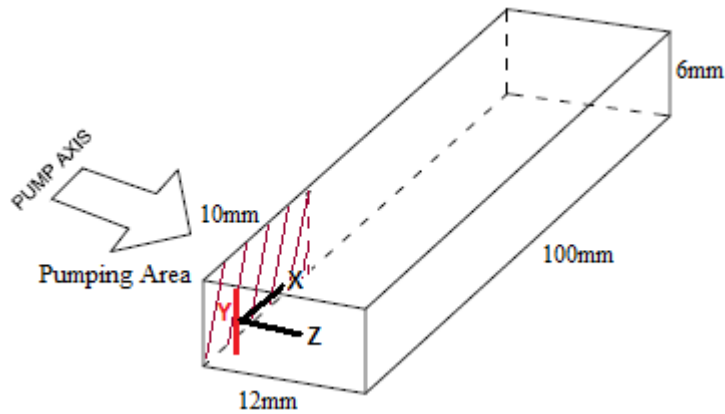
Figure 2.7: Representation of Position on which Temperature Distribution was Derived

First, $g(y)$ will be calculated for the uniform and the nonuniform pumping cases and then the generated thermal profiles on the fast-axis will be derived. Using realistic values; consider the gain medium in the dimensions 100mm x 6mm x 12mm, on the x, y and z axes, is pumped with a single laser diode-stack of which output power is 560W at 20Hz repetition rate in 230μs pulse width. Thus the average output power becomes:

$$P_{out,avg} = 560W \times 20Hz \times 230.10^{-6}s \cong 2.58W \qquad (2.2)$$

<u>Uniform Pump Profile:</u>

The emission area of a single diode-stack on the x-axis is approximately 10mm. Thus the average absorbed power density, $P_{abs. \, density}$, at $z = 0$ becomes:

$$P_{abs. \, density} = \frac{P_{out,avg}}{Absorption \, Volume} = \frac{2.58}{1 \times 0.6 \times 1.2 cm^3} \cong 3.6 \, \frac{W}{cm^3} \qquad (2.3)$$

It is reported in the literature that 30-43% of the absorbed pump power contributes to the heat generation inside the crystal [10], [11], [20]. For now, this value was accepted as 35% and thus the absorbed power density that contributes to the heat generation, $P^h_{abs. \, density}$, is given in equation 2.4. As a result, the uniform top hat $P^h_{abs. \, density}$ distribution becomes as plotted with the blue line in Figure 2.8.

$$P^h_{abs. \, density} = 3.6 \times 0.35 \cong 1.26 \, \frac{W}{cm^3} \qquad (2.4)$$

The heat load with such an absorbance profile is the integral of the curve, i.e.;

$$Heat\ Load = \int_{-0.3}^{0.3} 1.26 dy = 0.76 \frac{W}{cm^2} \tag{2.5}$$

Nonuniform Pump Profile:

For the case of pumping the gain medium with a nonuniform beam profile, it will be considered that the pump source is very close to the gain medium. For this reason, the beam width of the pump source will be smaller than the one of the top hat distribution at the proximity of the entrance surface (See Figure 4.13). The same heat load of the gain medium with uniform absorbance case will be used to compare both cases precisely. Assume the absorbed pump power density, that contributes to the heat generation inside the crystal, as a result of nonuniform pumping to be given by the profile with the red line in Figure 2.8. This analytical expression is easy to integrate and resembles a typical realistic beam profile of the laser diode-stack (See Figure 6.3).

$$g(y) = \frac{8.1}{1 + (30y)^2} \ [W/cm^3] \tag{2.6}$$
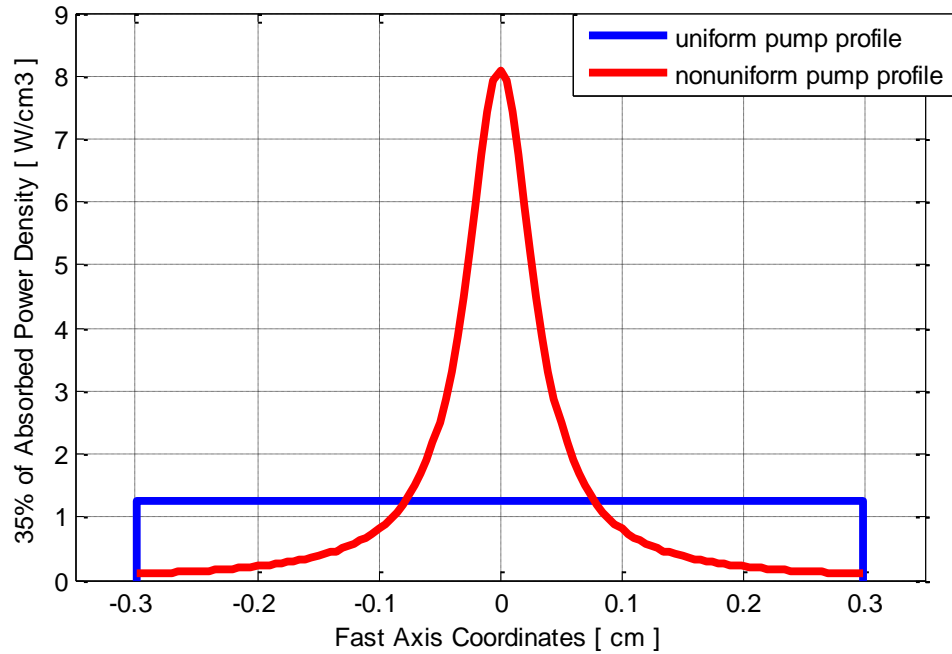
Figure 2.8: Uniform and Nonuniform Absorbance Profiles (at z = 0) that Contribute to the Heat Generation inside the Crystal

Analytical calculations of temperature distributions that come along with such power densities will be obtained by solving the differential equation in 2.1 for temperature, T. There are two boundary conditions for solving the equation: one is $\partial T / \partial y = 0$ since the change of the functions at $y = 0$ is zero as observed in Figure 2.8, and let's say the crystal is held at room temperature to write the second boundary condition, i.e. $T(0.3) = 25\ °C$.

First, the temperature profile for the uniform pumping will be derived. By integrating the equation 2.1 once yields:

$$\frac{\partial^2 T(y)}{\partial y^2} + \frac{1.26}{k} = 0 \tag{2.7}$$

$$\frac{\partial T(y)}{\partial y} + \int \frac{1.26}{k} dy = \frac{\partial T(y)}{\partial y} + \frac{1.26y}{k} + C1 = 0 \tag{2.8}$$

13

By using the first boundary condition, $\partial T / \partial Y = 0$ at $y = 0$, $C1$ is found to be zero. Then integrating equation 2.8 yields:

$$T \; y \; + \; \frac{1.26}{k} \; y \; dy = T \; y \; + (\frac{1.26}{2k} \; y^2 \; + C2 \;) = 0 \tag{2.9}$$

The constant $C2$ can be found by using the second boundary condition, $T \; 0.3 \; = 25$. Substituting $y = 0.3$ and $k = 0.13$ into equation 2.9 yields equation 2.10. The resulting analytical solution of one dimensional heat equation for $T(y)$ by given uniform absorbance profile is given with equation 2.11.

$$C2 = -25 - \frac{1.26}{2(0.13)} \; (0.3)^2 \cong -25.44 \tag{2.10}$$

$$T \; y \; + (\frac{1.26}{2k} \; y^2 \; - 25.44 \;) = 0 \tag{2.11}$$

The resulting temperature distribution as a result of the given uniform pump and absorbance density distributions is plotted with the blue line in Figure 2.9. There is approximately 0.44 °C temperature difference between central point and side surfaces of the crystal.

Now the temperature distribution for the nonuniform pumping case will be derived. Integrating the differential equation, given in equation 2.1, once yields:

$$\frac{\partial T(y)}{\partial y} + \; \frac{g \; y}{k} dy \; = \frac{\partial T(y)}{\partial y} + \; \frac{1}{k} \frac{8.1}{1 + (30y)^2} \; dy \; =$$

$$= \frac{\partial T(y)}{\partial y} + \; \frac{8.1}{30k} tan^{-1}(30y) + C1 \; = 0 \tag{2.12}$$

By using the first boundary condition, $\partial T / \partial Y = 0$ at $y = 0$, $C1$ can be found, i.e.:

$$\frac{\partial T(y)}{\partial y} + \; \frac{8.1}{30k} tan^{-1}(30y) + C1 \; = 0 + (0 + C1) \; = \; 0 \tag{2.13}$$

Thus $C1$ is found to be zero. Then integrating equation 2.13 yields:

$$T \; y \; + \; \frac{8.1}{30k} tan^{-1}(30y) \; dy =$$

$$= T \; y \; + \; \frac{8.1}{30k} \; y \times tan^{-1} \; 30y \; - \frac{\log(30^2 y^2 + 1)}{30 \times 2} \; + C2 \; = 0 \tag{2.14}$$

The constant $C2$ can be found by using the second boundary condition that is $T \; 0.3 \; = 25$. Substituting $y = 0.3$ and $k = 0.13$ into equation 2.14 yields:

$$C2 = -25 - \frac{8.1}{30 \times 0.13} \; 0.3 tan^{-1} \; 0.16 \; - \frac{\log(30^2 \times 0.3^2 + 1)}{30 \times 2} \; \cong -25.76 \tag{2.15}$$

Thus the analytical solution of one dimensional heat equation for $T(y)$ resulting from the nonuniform pumping becomes:

$$T \; y \; + \; \frac{8.1}{30k} \; y \times tan^{-1} \; 30y \; - \frac{\log(30^2 y^2 + 1)}{30 \times 2} \; - 25.76 \; = 0 \tag{2.16}$$

The resulting temperature distribution as a result of the given nonuniform pump and absorbance distributions is given with the red line in Figure 2.9. There is approximately 0.76 °C temperature difference between central point and the side surfaces of the crystal.

14
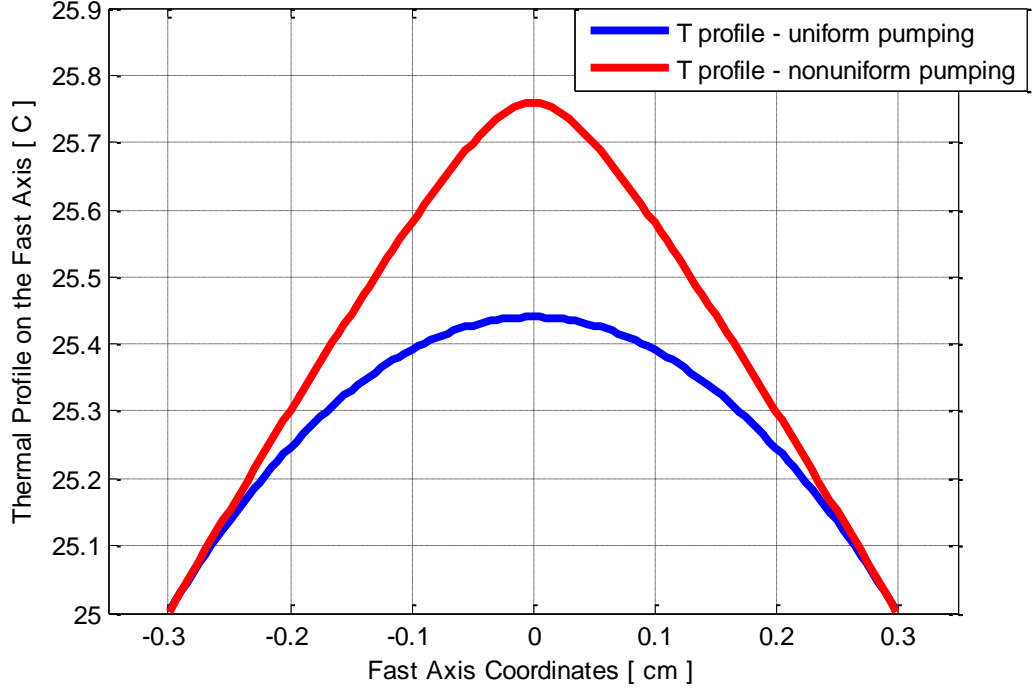
Figure 2.9: Temperature Distributions (at z = 0) Formed as a result of the Uniform and the Nonuniform Pumping Cases

2.2.2. Temperature Dependent Optical Path Difference (OPD) and Calculation of Thermal Lens Beam Radius

The aberrated laser wavefront is discussed in terms wavefront distortion or OPD. Nonuniform temperature distributions of the previous section cause a gradient in refractive index, Δn, and nonuniform expansion along the gain medium. The change in refractive index and expansion of the gain medium cause OPD on the laser beam passing through the crystal. OPD calculation by using thermally induced refractive index change and expansion along the gain medium is given in equation 2.17 [21].

$$OPD = \ \Delta T.\frac{dn}{dT}.L \ + (\Delta T.\alpha(T).L)$$

$$= \ \Delta T.L \ \times \ \frac{dn}{dT} + \alpha(T) \tag{2.17}$$

where dn/dT is the temperature coefficient of refractive index, $\alpha(T)$ is the temperature dependent linear expansion coefficient, ΔT is temperature difference between two points and L is the length of gain medium.

The radius of curvature of the thermal lens will be calculated by means of OPD on the laser beam. This calculation will be carried out in the same way as the wavefront analyzer does, so that the calculated beam radius values can be compatible with the measurements. A slowly varying function in 2 dimensions can be approximated by a paraboloid. A wavefront analyzer relies on this principle to deduce beam parameters and aberrations by means of fitted coefficients [22]. OPD therefore can be written as;

$$OPD \ x,y \ = \frac{2\pi}{\lambda} \ P + T_x x + T_y y + \alpha x^2 + \beta y^2 + \gamma xy \tag{2.18}$$

where P is the "piston" term and this constant value does not give an aberration. T_x and T_y are related to tilts and do not contribute to the divergence. The lens effect is governed by the second order terms;

$$OPD(x,y) = \frac{2\pi}{\lambda}\left(\frac{x^2}{2R_x} + \frac{y^2}{2R_y}\right) \tag{2.19}$$

$$R_x = \frac{1}{2\alpha} \quad and \quad R_y = \frac{1}{2\beta} \tag{2.20}$$

In equations 2.18 and 2.19, $2\pi/\lambda$ is the propagation constant of the medium that appears in the phase term, whereas the rest describes the fitted surface on which phase is constant. Since the temperature difference is mainly on the fast axis, only R_y will be investigated.

Assuming the entire length of the crystal in Figure 2.7 is side-pumped, OPD curve out of temperature distribution formed by uniform pumping was plotted by using equation 2.17. The length of gain medium was taken to be $L = 10cm$, dn/dT is given to be $8.9 \times 10^{-6} \, °C^{-1}$ and $\alpha(T)$ is given to be $7.7 \times 10^{-6} \, °C^{-1}$ [23]. The resulting curve is given in Figure 2.10. A paraboloid was fitted to OPD curve as shown in the figure in order to calculate the fast-axis beam radius, R_y. By using the second order term of the fitted curve, the beam radius on the fast-axis was calculated through equation 2.21 and found to be -625 cm. The radius curvature of the surface is also called "thermal lens radius".
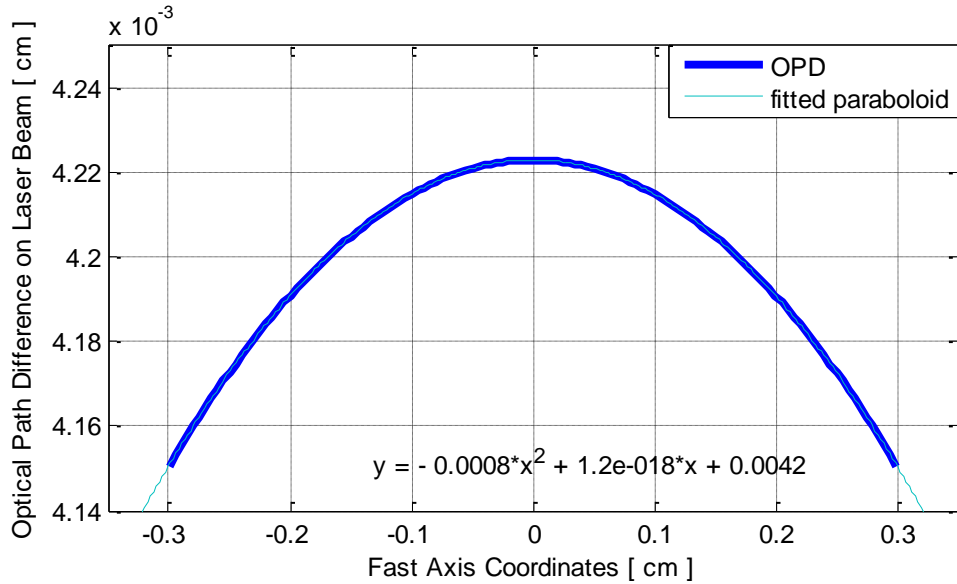
Figure 2.10: OPD Profile on Laser Beam and Fitted Paraboloid on the Curve – Uniform Pumping Case

$$R_y = \frac{1}{2 \times -0.0008} \cong -625 \, cm \tag{2.21}$$

In the same manner, OPD curve out of thermal distribution formed by nonuniform pumping, given in Figure 2.9, was plotted. The resulting curve and the fitted paraboloid on it are given in Figure 2.11.

Again by using the second order term of fitted curve, the fast-axis beam radius, namely thermal lens radius was found to be -357 cm, i.e.;

$$R_y = \frac{1}{2 \times 0.0014} \cong -357 \, cm \tag{2.22}$$

There is a significant difference between two radius values. Using realistic values, nonuniform pumping causes nearly a 2 times stronger thermal lens.

16
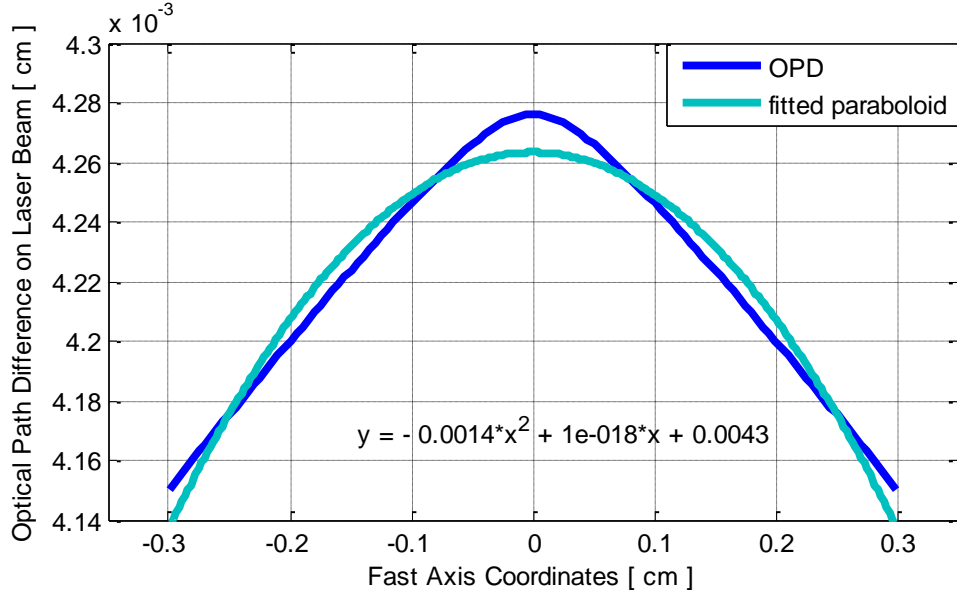
Figure 2.11: OPD Profile on the Laser Beam and Fitted Paraboloid on the Curve – Nonuniform Pumping Case

2.2.3. The Effect of Thermal Lens on the Far-Field Beam Divergence

When focused, a diffraction limited beam can be obtained by means of a collimated laser beam. For this reason, divergence is one of the most important beam quality parameters of a laser source. The calculation of beam divergence proceeded by means of an optical analysis software called "GLAD".

Let's consider the length of the laser resonator to be approximately 65cm and the pulse duration of the laser to be 10ns. Thus the laser beam passes 4 times, in 2 round-trip, along the gain medium in a pulse duration as given in equation 2.23. Since the length of the gain medium is 10cm out of 65cm resonator length, the average speed of light was calculated.

$$N_{pass} = \frac{v_{light} \times T_{pulse}}{L_{res}} = \frac{\frac{L_{cr}/L_{res}}{n} + (1 - L_{cr}/L_{res}) \times c \times T_{pulse}}{L_{res}} \tag{2.23}$$

$$N_{pass} = \frac{[(\frac{0.15}{1.82} + 0.85) \times 3.10^{10} cm/sn] \times (10.10^{-9} sn)}{65 cm} \tag{2.24}$$

$$\cong 4 \; times$$

where c is the speed of light, n is the refractive index of Nd:YAG crystal, T_{pulse} is the pulse duration, L_{cr} is the length of the crystal and L_{res} is the length of the resonator. That means the wavefront passes 4 times through the thermal lens in a pulse duration.

In order to show the effect of thermal lens on the beam divergence, first, the focal lengths of the found thermal lens radius values for the uniform and the nonuniform cases were calculated. Then the laser beam in 1064nm was passed 4 times in a lens having that focal length in the software, as given in Figure 2.12, in order to derive the output beam divergence because of the thermal lens. Beam divergence is calculated at the far-field, that's why, an ideal converging lens with a focal length 100cm was used to focus the laser beam in the software.

Consider a plano-convex lens with $R1 = \infty$ and $R2 = R_{thermal\ lens}$, where $R_{thermal\ lens}$ is the found thermal lens radius values. The focal length of a lens is calculated through equation 2.25, i.e.:

$$\frac{1}{f} = \; n - 1 \; \; \frac{1}{R1} - \frac{1}{R2} + \frac{(n-1)d}{n.R1.R2} \tag{2.25}$$

17

where f is the focal length, n is the refractive index of Nd:YAG crystal, d is the thickness of thermal lens.
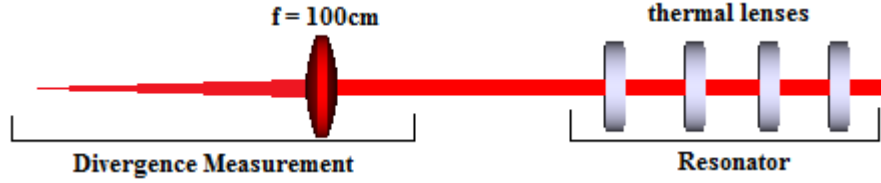
Figure 2.12: Far-Field Beam Divergence Setup for Numerical Calculation

The focal length of the thermal lens generated by uniform pumping becomes:

$$\frac{1}{f} = \begin{bmatrix} 1.82 - 1 \end{bmatrix} \begin{bmatrix} \frac{1}{\infty} - \frac{1}{-625cm} \end{bmatrix} + \frac{(1.82 - 1)d}{\infty} \qquad (2.26)$$

$$f \cong 762cm$$

Importing the found focal length into the software, the far-field divergence value was calculated to be approximately $2.7 mrad$ by means of the GLAD source code given in Appendix B.

The same procedure was repeated for the nonuniform pumping case. The focal length becomes:

$$\frac{1}{f} = \begin{bmatrix} 1.82 - 1 \end{bmatrix} \begin{bmatrix} \frac{1}{\infty} - \frac{1}{-357cm} \end{bmatrix} + \frac{(1.82 - 1)d}{\infty} \qquad (2.27)$$

$$f \cong 435cm$$

The far-field beam divergence was calculated to be approximately $3.9 mrad$ by means of the GLAD source code given in Appendix C. These calculated divergence values were calculated with ideal Gaussian modes for the laser beam. However, actual laser modes can be different from Gaussian modes.

It is observed from Figure 2.11 that the fitted paraboloid does not exactly match with the resulting optical path difference plot as a result of nonuniform pumping. It means that the obtained thermal lens radius value and thus the generated thermal lens focal length changes across the crystal cross section. The thermal lens focal length changes with the laser beam diameter or the position on x and y axes from where the beam passes along the z-axis. Let's consider the beam passes along the center of the crystal at $z = 0$, the thermal lens focal length changes with laser beam diameter as shown in Figure 2.13. As a result, the far-field laser beam divergence changes with the thermal lens focal length as given in Figure 2.14. The given $3.9 mrad$ was calculated for 6mm laser beam diameter.

The far-field laser beam divergence that was found as a result of nonuniform pumping is more than 1.5 times greater than the one found as a result of uniform pumping. Such a difference in beam divergence is very crucial in laser applications. Higher values in beam divergence should be reduced by using a beam expander which expands and collimates the laser beam at the output of a laser source. However, using a beam expander brings extra volume, weight and cost. The higher the amount of thermal lens is, the bigger magnification with beam expander is required. That' why, designer will not gain only from the system efficiency and beam quality but also from the volume, weight and the cost by reducing the amount of thermal lens.

18
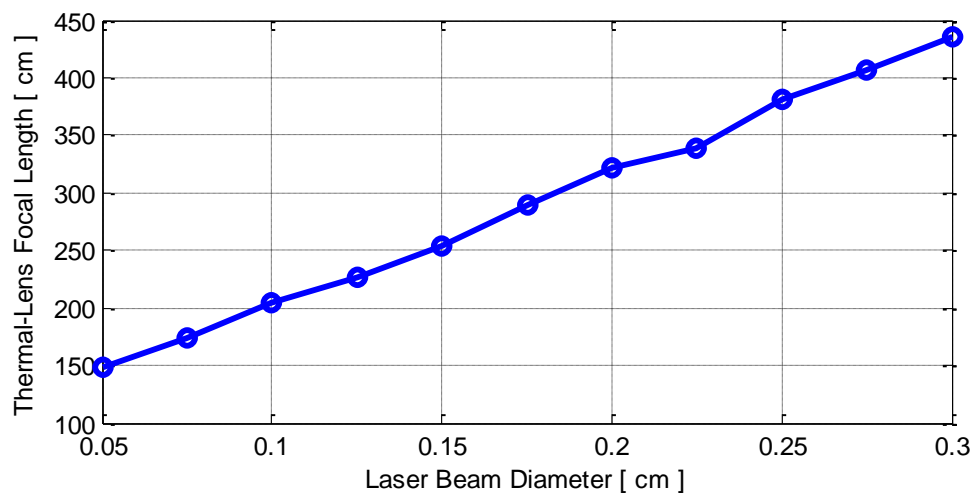
Figure 2.13: Thermal Lens Focal Length versus Laser Beam Diameter
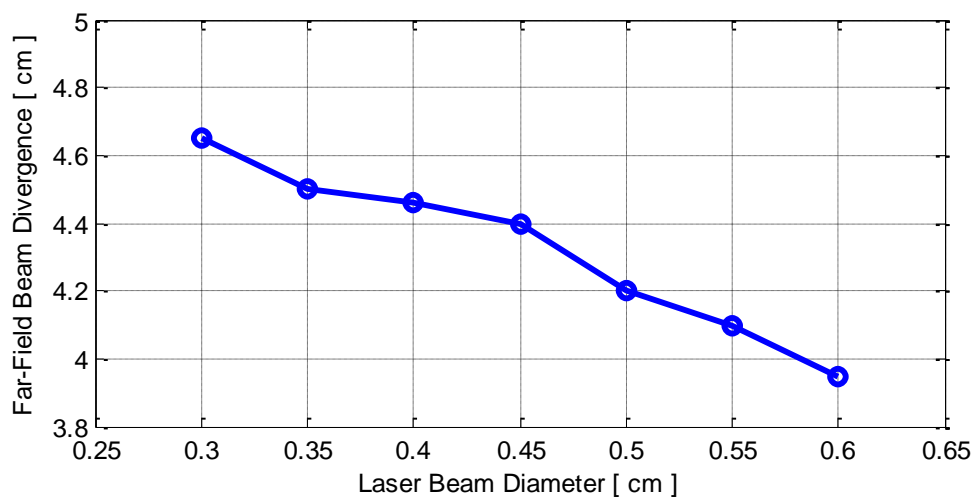
Figure 2.14: Laser Beam Divergence versus Laser Beam Diameter

LASER DIODE CHARACTERIZATION WITH OPTICAL FIBER

In order to design a pump chamber for a diode-pumped solid-state laser, the designer should know the divergence and beam profile of emitted beam from the laser diode(s). The change over beam profile as a function of the repetition rate, the temperature of laser diode etc. should be also known. Therefore, before starting a pump chamber and resonator design for a diode-pumped solid-state laser source we need to characterize laser diodes that will be used as pump source. There are methods in the literature to characterize the divergence profile and some other features of the laser diodes by using an optical fiber. In this work, a modified version of such a method was developed and verified. The beam profile is simply obtained by scanning the space by an optical fiber.

The method was first tested and verified by using a single laser diode emitter. Then laser diode-stacks to be used as pump source in this study were characterized for obtaining the beam profiles with respect to the position on the z-axis, the applied current value to the stack, the TEC (stack) temperature value and the repetition rate.

3.1. The Development Stage of the Method and Its Verification

3.1.1. The Setup and Method

A single emitter laser diode of "Coherent Inc." as shown in Figure 3.1 was used. The laser diode emits at 808nm. The measurements were taken with a controllable power source at the voltage and current values of 2V and 0.6-0.7A, respectively.
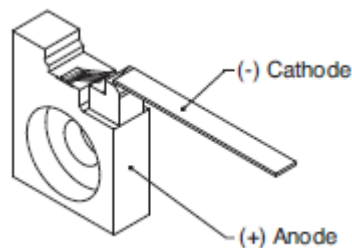
Figure 3.1: The Single Emitter [24]

The emitted beam was expanded and nearly collimated by a beam expander. A CCD camera was used to observe and save the beam profile that was used later to verify the method. Since the sensor size of CCD camera is very small compared to the beam size. The beam passed through an iris as shown in Figure 3.2.

An optical density (ODE) filter that attenuates the laser beam, was used to protect the sensor of CCD camera. The CCD camera was a USB-capable model of "Spiricon - LW230". The beam was observed on the monitor and saved on the PC. An example of the observed beam on the monitor is shown in Figure 3.3.

After saving the observed beam on the computer, the CCD camera was removed and a fiber optical cable was placed at the same position with the CCD sensor as shown in Figure 3.4. A multi-mode optical fiber with 50μm core radius was used. The fiber is mounted on a x-y-z stage to give freedom in 3D. The stage takes 88.75 tours in one axis which yields a total distance of 28mm.
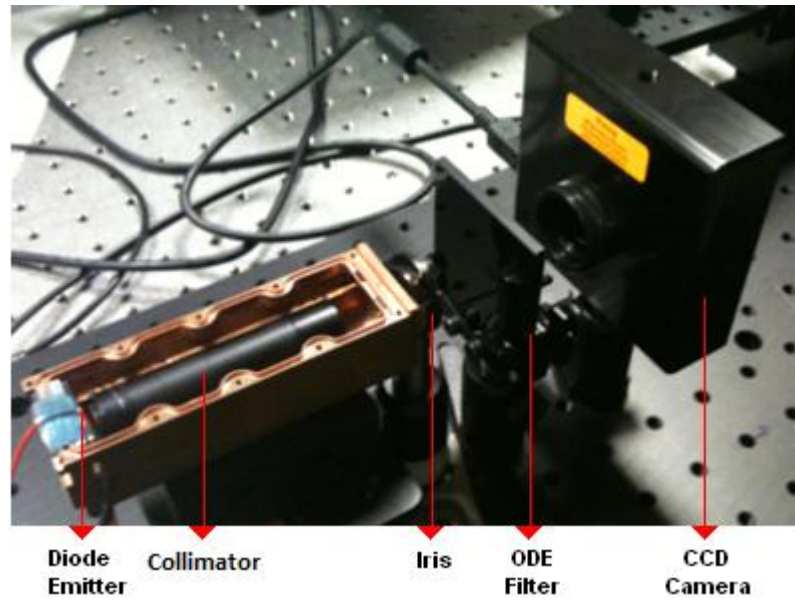
Figure 3.2: Observation of Emitted Beam by a CCD Camera
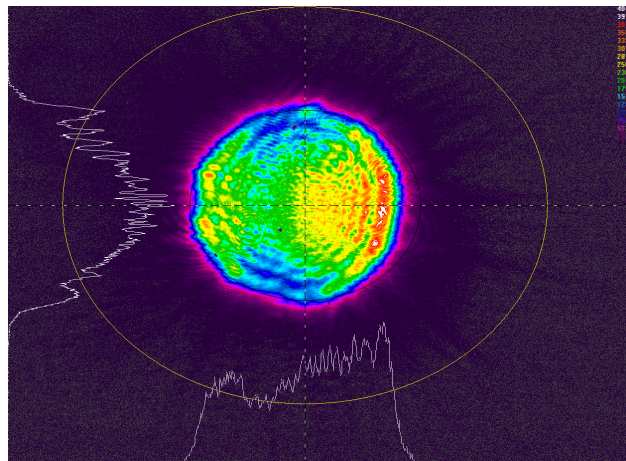
Figure 3.3: The Beam Observed on the PC by means of CCD Camera
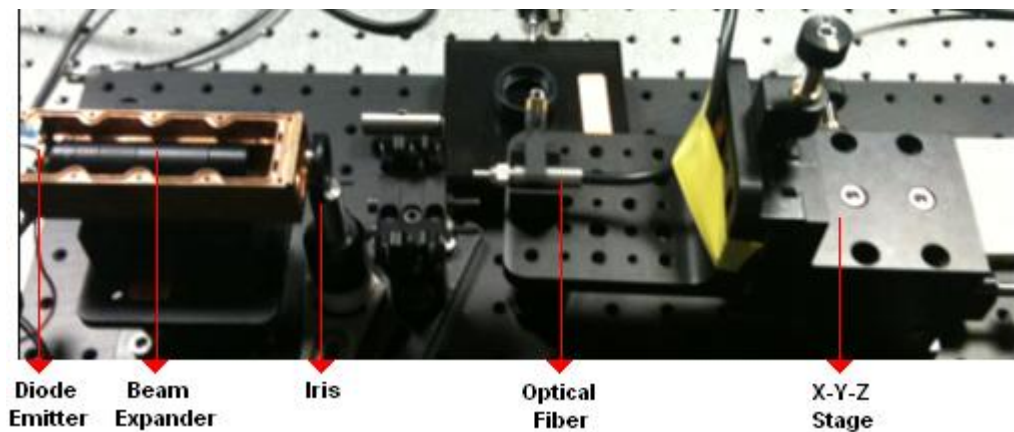
Figure 3.4: Detection of Emitted Beam by Using an Optical Fiber

A PIN photodiode of Thorlabs (S1223) was used to detect the signal at the other end of the fiber as shown in Figure 3.5. The voltage value of detected signal was observed by means of a scope.
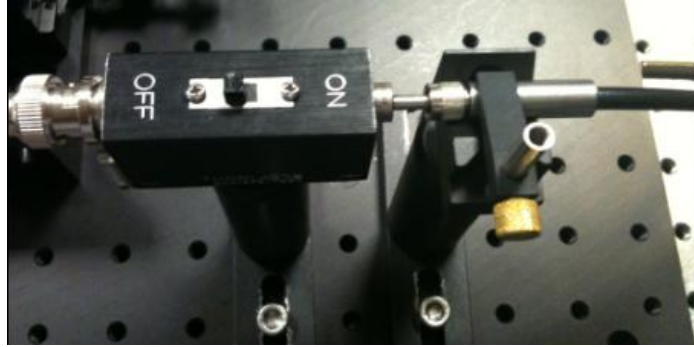
Figure 3.5: PIN Detector and the Other Side of Optical Fiber

The PIN detector was switched on and the beam was aligned on the optical fiber shown in Figure 3.4 by means of an IR viewer card. Then the voltage values were recorded along a line on desired axis (vertical or horizontal) of the beam by turning the screw heads half a tour which yields 158µm resolution on the chosen axis. In order to confirm this empirical data taken on one a single line and verify the scanning method, the measured data were compared to the data previously saved on the PC by means of CCD camera. The comparison was carried out by plotting both measured and saved data on the same figure. The measured data were taken on the central axes for the simplicity.

The recorded beam profile in .cma format on the PC was converted to matrix form by using "ORIGIN" program. The central axes were approximately found from the matrix in ORIGIN and the data from these two axes were transferred to MATLAB. The measured data were also imported to MATLAB and each data plotted on the same figure for comparison. The recorded beam profiles is given in Figure 3.6 while the plots that compare measured and recorded data on the central axes are given in Figure 3.7 and Figure 3.8. Red lines are the data recorded on the PC by means of the CCD camera, while blue lines are the measured data on the same lines on the central axes.

As shown from the figures, the measured and original data saved on the PC are approximately the same, which means that the method can be reliably used to extract beam profile along a line on a desired beam at any position.
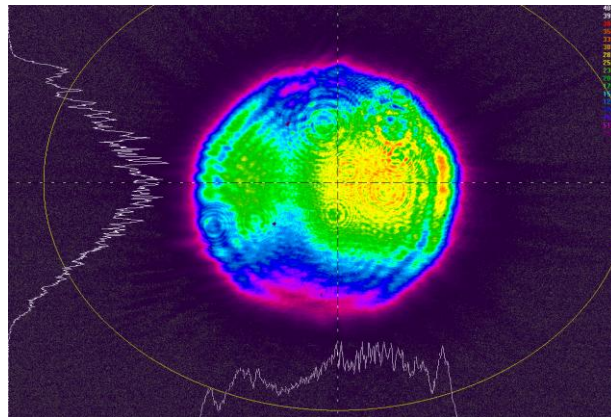
Figure 3.6: One of the Investigated Beam Profiles on the PC
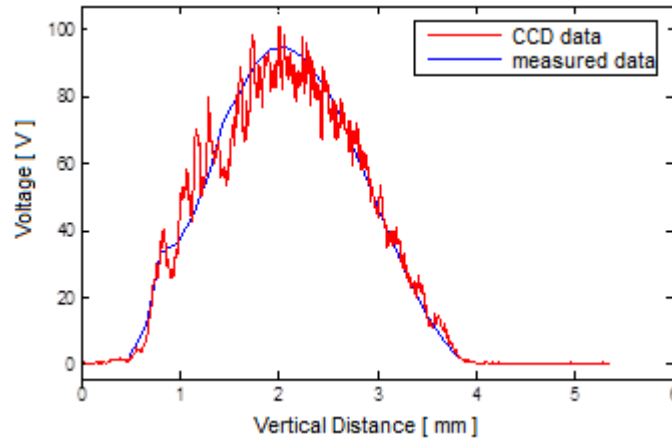
Figure 3.7: The Vertical Line Measurements
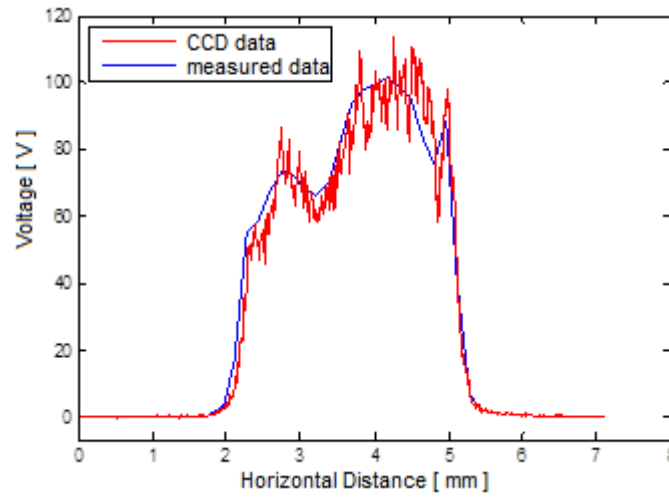
Figure 3.8: The Horizontal Line Measurements

3.2. Application of the Method to the Laser Diode-Stacks

Here the scanning procedure by an optical fiber as outlined in chapter 3.1 was used to characterize the laser diode-stacks. The characterization of the stacks includes the change at beam profile with respect to position, repetition rate and temperature of the stacks. The procedure was also repeated for different laser diode-stacks of the same model to confirm that they are all consistent profiles. In the reported stack, the emitting aperture of x-width is 0.102mm and y-width is $5x10^{-4}$mm. The row spacing between the emitters is 0.148mm. The total emitting area is 10mm x 2.4mm. This dimensional information was used in pump chamber design that was explained in chapter 5.

3.2.1. The Setup and Measurements Taken with Laser Diode-Stacks

The optical fiber was mounted on a x-y-z stage that has 25mm moving distance with micrometer positioning sensitivity as shown in Figure 3.9. The laser diode-stack was mounted on a metal plate as shown in Figure 3.10 to cool the stack down. The metal plate was kept at desired temperature by means of a TEC (Thermo-Electric Cooler) and a TEC controller. Temperature information was returned by a thermistor to the TEC controller. The voltage information was read again by means of the same PIN detector looking to the other end of optical fiber as shown in Figure 3.5 and observed by an oscilloscope which is connected to the PIN detector by a BNC cable. An OD-0.7 filter was placed between fiber optical cable and the detector to preserve PIN detector from saturation.

24
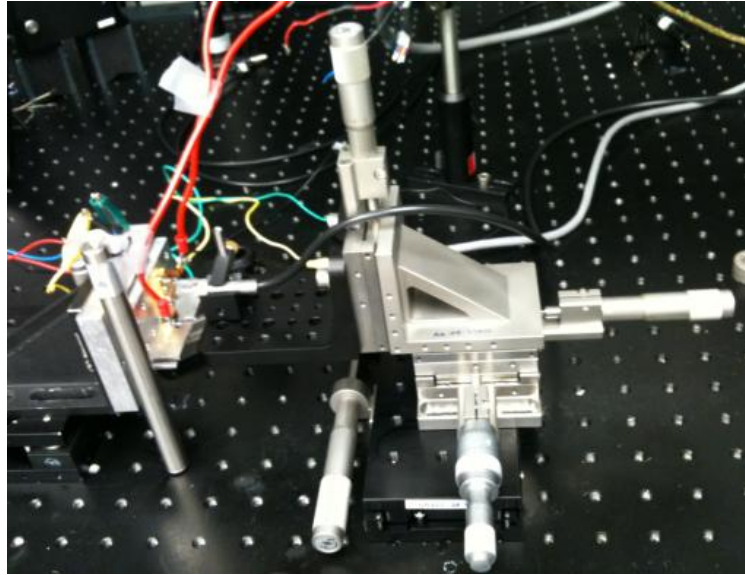
Figure 3.9: Optical Fiber that was Mounted on the X-Y-Z Stage
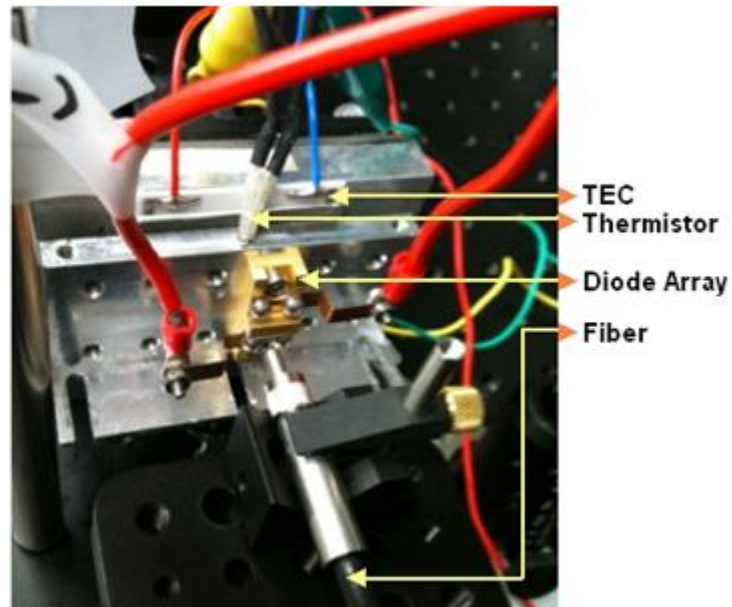
Figure 3.10: The Laser Diode Assembly with Its Heat Sink

3.2.1.1. Measurements Regarding Slow and Fast Axes Beam Profiles

The beam profiles on the fast and the slow axes versus optical fiber position were obtained. The laser diode-stack was driven with 2Hz repetition rate, 230μs pulse duration and at different current values by using the laser diode controller. The temperature of TEC plate was kept constant at 45°C by means of TEC controller. The first measurement was taken for the slow-axis at a position where the fiber optical cable was directed towards the laser diode-stack as much as possible on the pump axis. This position of the optical fiber was accepted as z = 0mm. Measurement was repeated at three different current values, 80A, 100A and 120 A as shown in Figure 3.11.

The voltage values were normalized to see the dependence of beam profile to the current as shown in Figure 3.12. As seen from the normalized plot, although the output power of the laser diode-stack changes, the beam profile is independent of the current value that the stack is driven with.

The slow-axis beam profiles versus the optical fiber position on the pump axis were obtained at a constant current value, 80A, to extract the divergence information as shown in Figure 3.13.
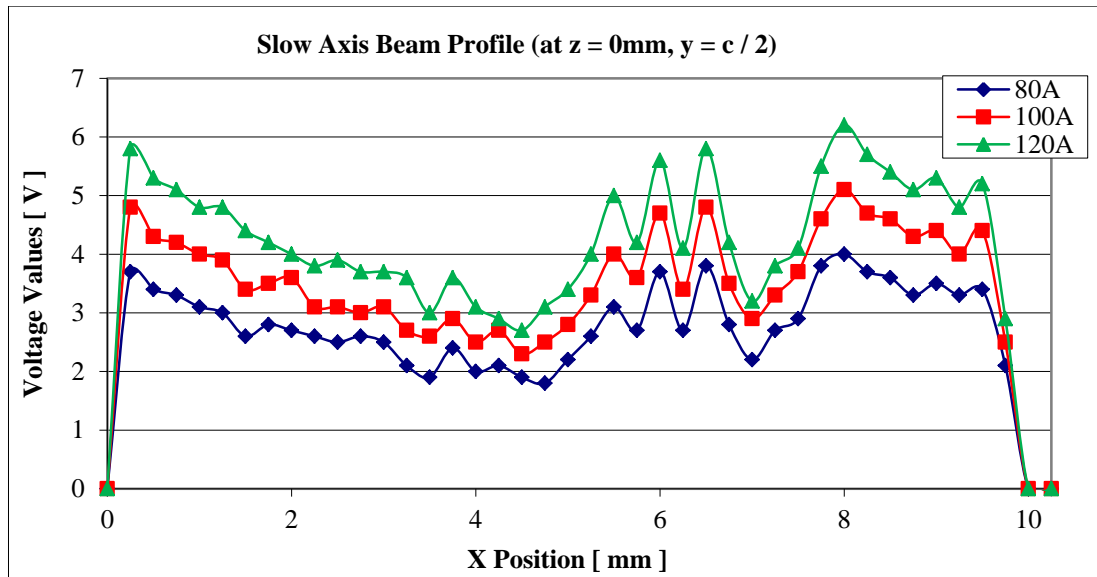
Figure 3.11: Slow-Axis Beam Profiles at z = 0mm at Different Current Values
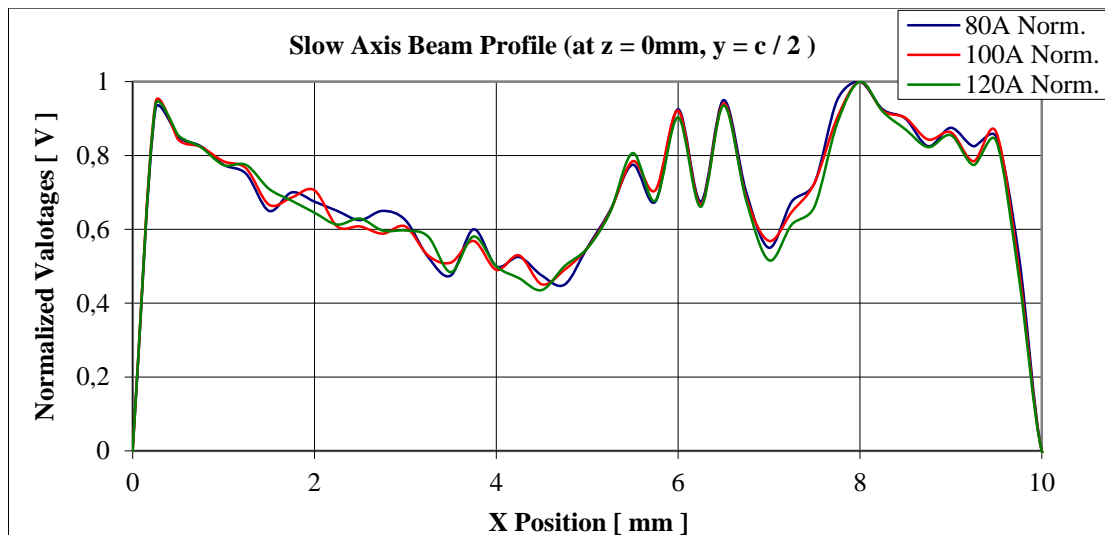
Figure 3.12: Normalized Slow-Axis Beam Profiles at z = 0mm
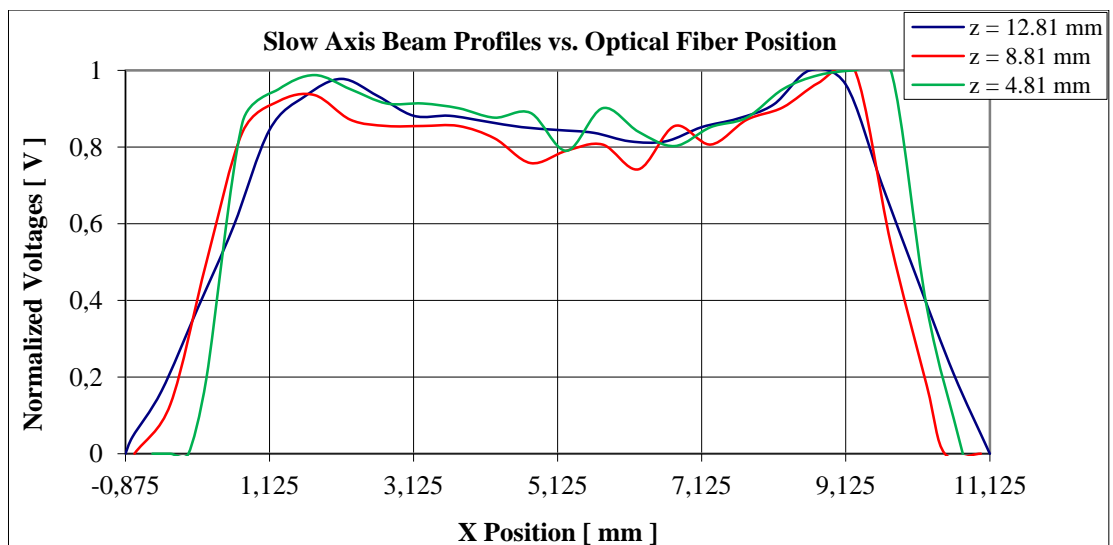
Figure 3.13: Normalized Slow-Axis Beam Profiles vs. Optical Fiber Position

The lower voltage values of the pump beam was not accurately measured, therefore divergence angle was calculated by using the beam widths at 10% of maximum values. A representation of divergence angle calculation between two measurements or namely two positions is given in Figure 3.14. W1 is the beam width at 10% of the maximum value at distance Z1 from laser diode-stack, and W2 is the beam width at 10% of the maximum value at distance Z2 from laser diode-stack. The distance between Z2 and Z1 is Z, namely $Z2 - Z1 = Z$. Then the half angle divergence angle becomes:

$$D = \arctan \frac{(W2 - W1)/2}{Z} \tag{3.1}$$
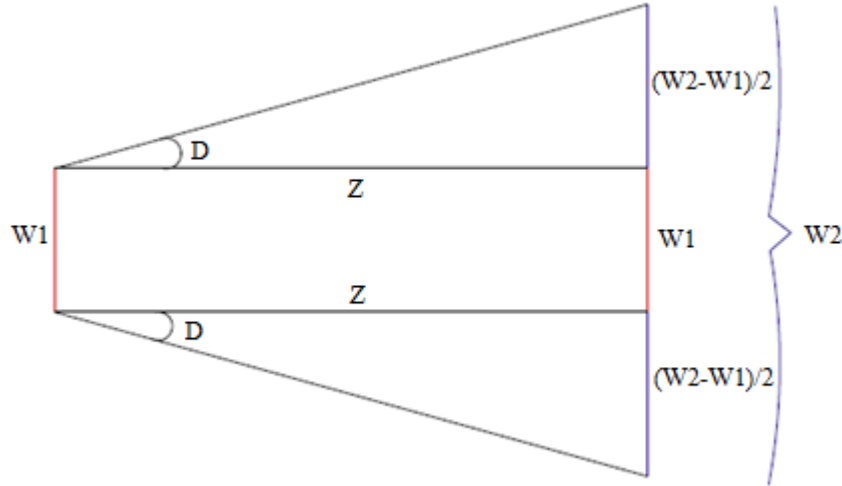
Figure 3.14: Divergence Angle Calculation between Two Distances

By using the beam width at 10% of max value as reference to Figure 3.13;

Beam width at z = 4.81mm becomes $5.43 - -4.87 = 10.3mm$
at z = 8.81mm becomes $5.32 - -5.53 = 10.85mm$
at z = 12.81mm becomes $5.75 - -5.7 = 11.45mm$

Half-angle divergence angle between $Z1 = 4.81mm$ and $Z2 = 8.81mm$ by using beam widths becomes:

$$D = \arctan \frac{(W2 - W1)/2}{Z}$$
$$= \arctan \frac{(10.85mm - 10.3mm)/2}{8.81mm - 4.81mm} = 3.93° \tag{3.2}$$

And the full angle divergence angle becomes: $2D = 7.86°$

The same divergence angle between any two z-positions was expected, but there were measurement inaccuracies. Therefore, the average divergence angle was calculated in this study. Half angle divergence angle between $Z1 = 8.81mm$ and $Z2 = 12.81mm$ becomes:

$$D = \arctan \frac{(11.45mm - 10.85mm)/2}{12.81mm - 8.81mm} = 4.3° \tag{3.3}$$

And the full angle divergence angle becomes: $2D = 8.6°$

Then the average slow-axis divergence angle becomes: $(7.86° + 8.6°)/2 = 8.23°$

The same routine was repeated for the fast-axis divergence. Firstly the beam profiles at $z = 0mm$ obtained at again three different current values as given in the normalized graphs in Figure 3.15.
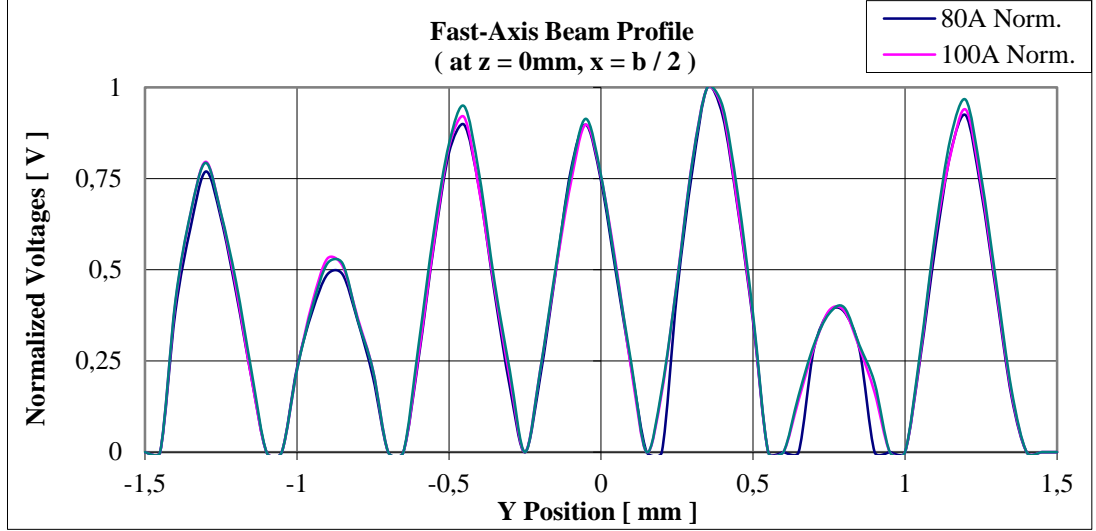
Figure 3.15: Normalized Fast-Axis Beam Profiles at z = 0mm

Seven peaks in the given figure are observed because of the seven diode arrays in the stack. One can notice from the figure that the total power emitted by each diode array is different. Total normalized power of each diode array will be useful in pump chamber design later on. One can again see from the normalized graphs that the beam profile is independent from the current value and that means the following measurements can be taken at any current value.

The beam profiles along the pump axis is more crucial for the fast-axis since the divergence angle for the fast-axis is higher than for the slow-axis and it is the main reason for the generated thermal lens due to the nonuniform pumping of the gain medium in a pump chamber free design. Therefore more measurements are taken to observe the change in beam profiles and calculate the divergence angle precisely. Some of the obtained fast-axis beam profiles taken at different positions on the pump axis with constant current value are shown in Figure 3.16.
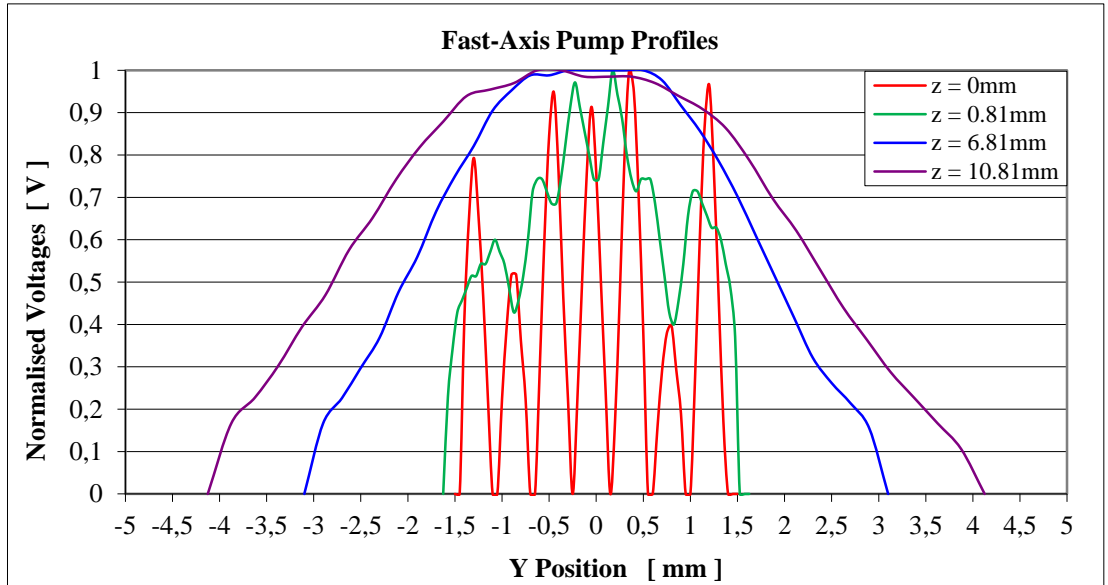
Figure 3.16: Normalized Fast-Axis Beam Profiles vs. Optical Fiber Positions

Pump profile variation as the beam propagates is clear from the figure. The same divergence angle calculation procedure was repeated for the fast-axis divergence angle. For instance, the half angle divergence angle between $Z1 = 0mm$ and $Z2 = 6.81mm$ becomes:

$$D = \arctan \frac{(5.8mm - 2.65mm)/2}{6.81mm - 0} = 13.02° \qquad (3.4)$$

And the full angle divergence angle becomes: $2D = 26.04°$

Half angle divergence angle between $Z1 = 10.81mm$ and $Z2 = 6.81mm$ becomes:

$$D = \arctan \frac{(7.7mm - 5.8mm)/2}{10.81mm - 6.81mm} = 13.4° \tag{3.5}$$

And the full angle divergence angle becomes: $2D = 26.8°$. After doing the same calculation for 10 measurements at different positions, the overall average of fast-axis divergence angle becomes 27.23°. All the fast-axis beam profile measurements are given in Appendix A.

The effects of repetition rate and temperature value of TEC plate on the beam profile were also observed. The effect of repetition rate on the fast-axis beam profile was observed at a fixed position on pump axis with three different repetition rates as plotted in Figure 3.17. The profile remained constant with varying repetition rate.
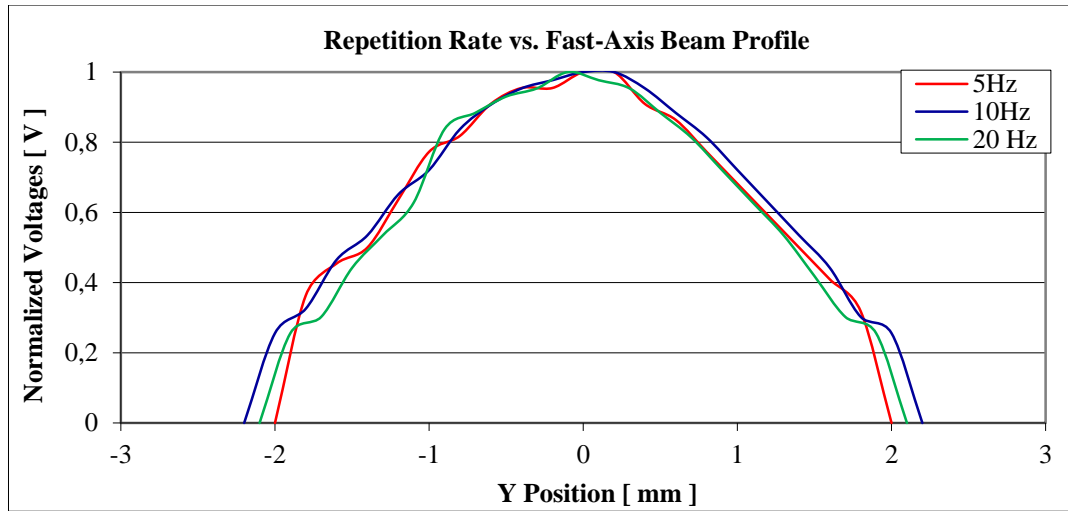
Figure 3.17: Normalized Fast-Axis Beam Profiles at Different Rep Rates at z = 2.81mm

The relationship between the fast-axis beam profile and the temperature value of TEC plate was also observed as shown in Figure 3.18 with three temperature values of TEC plate. As seen from both figures the shape of the fast-axis beam profile does not change with both repetition rate and temperature values, although top intensities differ. After observing the invariant beam profile versus repetition rate, 20Hz was used as a constant repetition rate for the following measurements since the heat load of the crystal is maximum at 20Hz repetition rate.
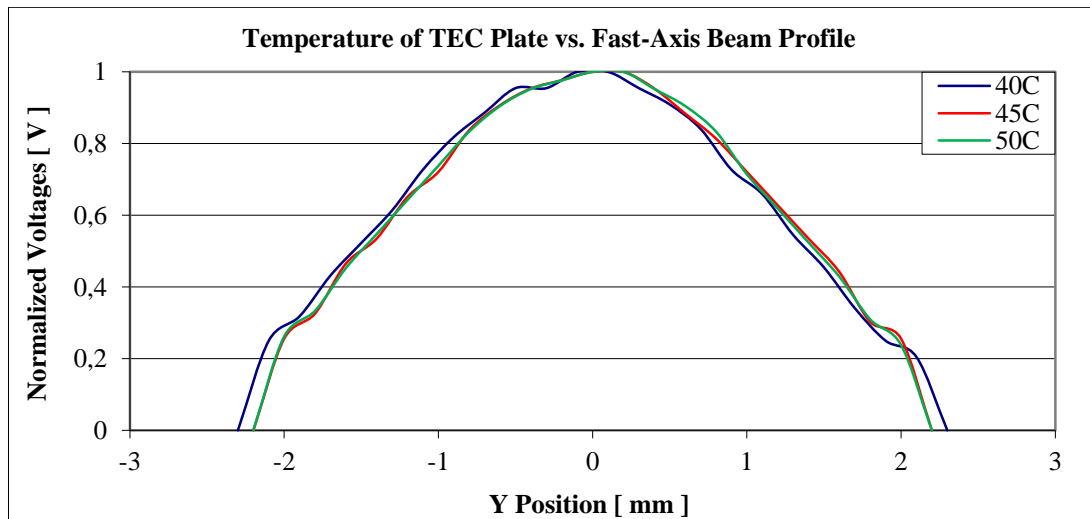
Figure 3.18: Normalized Fast-Axis Beam Profiles at Different Temperatures of TEC

3.2.1.2. Characterization of Pump Absorption by Active Medium

Pump wavelength varies with the temperature. Therefore, absorption characteristics of 1.1% doped Nd:YAG crystal was studied as a function of laser diode-stack temperature. A typical peak absorption wavelength of Nd:YAG crystal is 808nm as given in Figure 3.19. But the actual absorption spectrum may vary from vendor to vendor. Therefore, we studied the absorption of the crystals made from the same batch with respect to diode temperature. If the temperature of a diode-stack deviates from its design temperature, the peak emission wavelength also deviates from 808nm and as a result the amount of absorbed power by the crystal decreases.
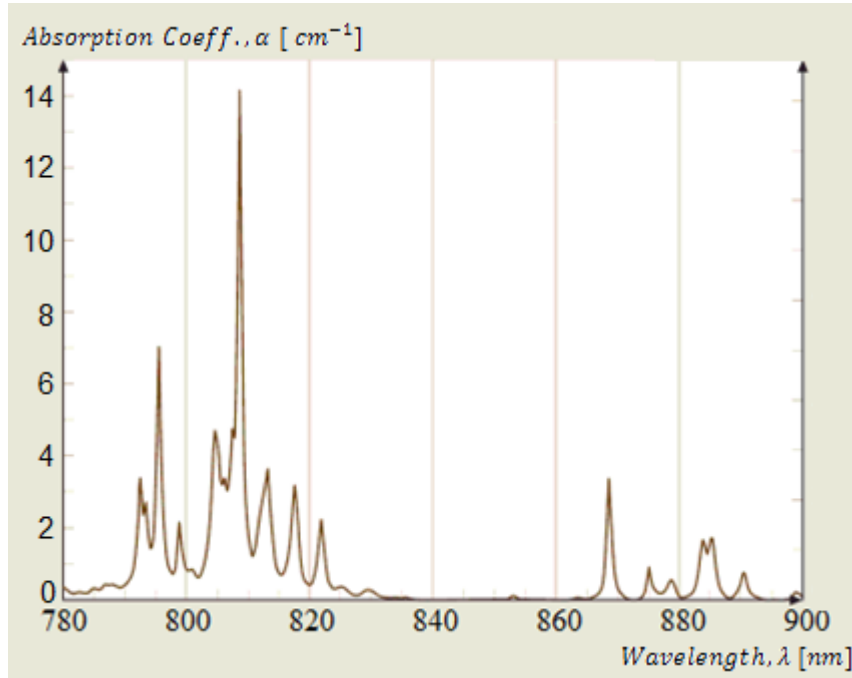
Figure 3.19: Absorption Spectrum of 1.1% Doped Nd:YAG Crystal [25]

The setup of the measurement is shown in Figure 3.20. Optical fiber was positioned at the end of Nd:YAG crystal that has a cross section 5mm x 5mm. The laser diode-stack was driven with 20Hz repetition rate and 230μs pulse rate.
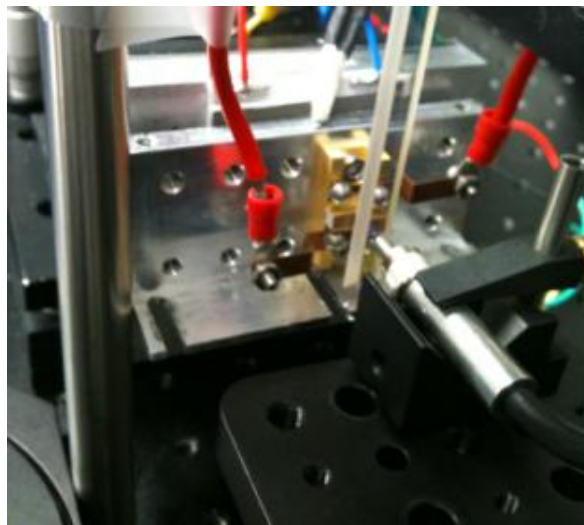
Figure 3.20: Measurement Setup of Absorption versus TEC Temperature

The crystal was then removed and the percentage absorption was calculated from the difference in power that was read with and without the crystal. The measurement was repeated with varied temperature values of TEC plate. Laser diode stack was manufactured to emit at 808nm around 50 °C. Therefore, the measurements were taken at between 44-62 °C. The result is given in Figure 3.21. Comparing the plotted percentage absorption profile with the absorption spectrum given in Figure 3.19 one can say that the maximum absorption of the crystal occurs when the diode temperature is at 52 °C.
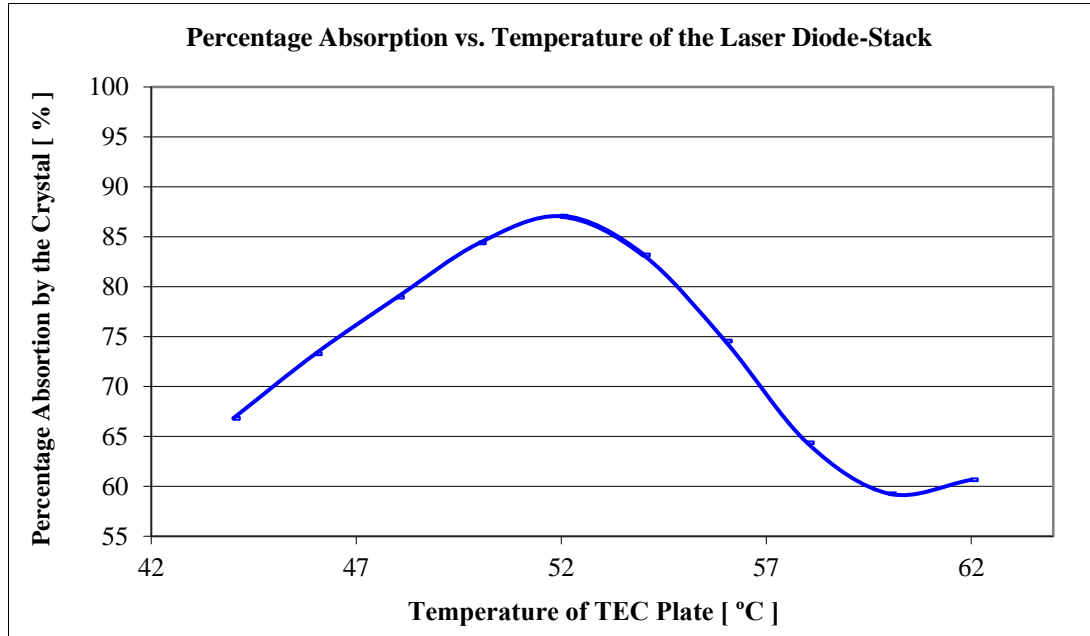
Figure 3.21: Change in the Percentage Absorption of Nd:YAG Crystal by the Temperature of Diode-Stack

CHAPTER 4

CALCULATION OF THERMAL LOADING COEFFICIENT

Thermal loading coefficient is the ratio of heat generated in the gain medium to the absorbed pump power. This coefficient enables us to calculate temperature distribution inside the crystal for any pump distribution. Refractive index profile across the crystal, thermal lens beam radius, wavefront aberrations and laser beam divergence can be calculated by using this temperature distribution. The coefficient is calculated for 1.1% doped Nd:YAG crystal in two steps: firstly thermal measurements were obtained by taking thermographic photos of the crystal cross section and then numerical simulations of crystal cross section temperature plots were carried each with different thermal loading coefficient until obtaining the same results with the empirical measurements.

In the empirical step, a slab crystal with the dimensions 70mm x 5mm x 12mm was pumped longitudinally by a laser diode-stack of which beam profile at any distance was known from chapter 3. The sides of the crystal was anti-reflection (AR) coated at around 808nm. Thermal images of the slab cross section were taken per minute while pumping the gain medium. Thermographic data were obtained from the captured thermal images. In the numerical step, our objective was to fit the thermal loading coefficient of the crystal that yields the same heat load per unit time as obtained from the experimental measurements. Absorbed fast-axis pump profiles across the gain medium were calculated by means of the beam profiles of the laser diode-stack measured in the previous section. Then the simulations that yield the heat load inside the crystal were carried out by means of CFD (Computed Fluid Dynamics) analysis in FLUENT 6.3 software. Each simulation was carried out with a different thermal loading coefficient and after each simulation the results were compared to the empirical ones. The simulations were continued until obtaining the same results with the empirical measurements.

4.1. Thermal Measurements of Diode Pumped Slab Crystal

First the thermal images of the diode-pumped slab crystal cross section were taken over uniform time intervals, with a setup as shown in Figure 4.1, in order to set base line for the numerical simulations. Later on, each numerical simulation was carried out with the same thermal load formed inside the crystal in this measurement and each with a different thermal loading coefficient. The procedure was iteratively performed until obtaining the same thermographic data with the one found as a result of the measurement.

The measurement was performed without heat sink on slab crystal for the sake of simplicity in numerical simulations. For this reason the slab crystal was hold with a small holder from the farthermost end of the crystal as shown in Figure 4.1. The slab crystal was longitudinally pumped along 10mm on the x-axis with a single laser diode-stack that was almost co-planar with the slab surface. The measurements for the beam profiles of laser diode-stack were given in chapter 3. The temperature of laser diode-stack was controlled with a TEC which was kept at 45 °C by means of a TEC controller. The ambient temperature was 25 °C that was read on the thermal camera.

Thermal images were recorded per minute by a thermal camera that is T335 model of FLIR Company. An example of the recorded images by thermal camera is shown in Figure 4.2. Images were analyzed as thermographic data by means of the software, "ThermaCAM Researcher". The temperature value

of any point or temperature profile of a line on an image can be extracted by the software. For instance, as shown in Figure 4.3, the temperature profile of the given cross section line of the slab along the middle part can be extracted in the software interface. The thermographic data can be also saved as m-file and can be analyzed in MATLAB by using the relevant pixels. Later on, these features were used to compare the numerical simulations with the thermal measurements.
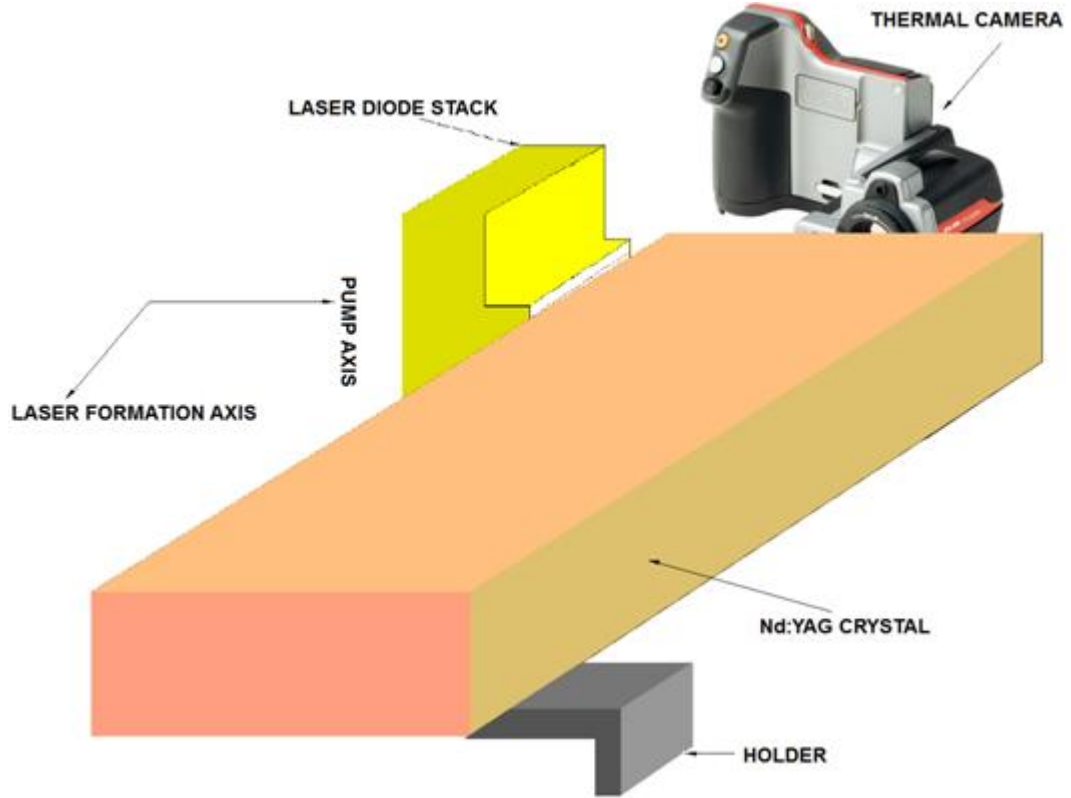
Figure 4.1: The Un-Cooled Crystal Setup for Obtaining Thermographic Data per Time
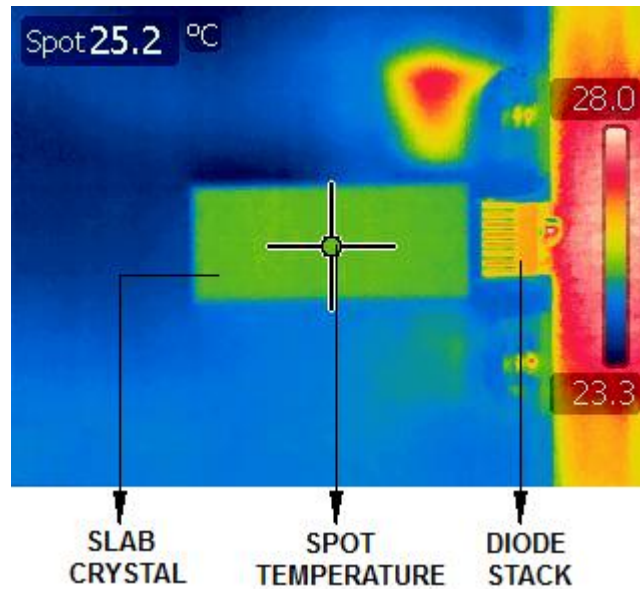
Figure 4.2: Thermal Image of Slab Cross Section at t=0 (Prior to Pumping)

Firstly, the diode-stack was driven with 100A current, 20Hz repetition rate and 230μs pulse width. Thermal images were recorded for 10 minutes while the slab crystal heated up. The temperature profiles of the crystal center cross section are given in Figure 4.4. Then the laser diode driver was

turned off and thermal images of the slab cross section while cooling it down were recorded for five minutes. Related thermal profiles for cooling down after pumping with 20Hz repetition rate are given in Figure 4.5. When the crystal reached to room temperature, the procedure was repeated for 10Hz repetition rate of which thermal profiles are given in Figure 4.6 and Figure 4.7. The crystal slab reaches a steady-state after pumping for five minutes for both 10Hz and 20Hz repetition rates.
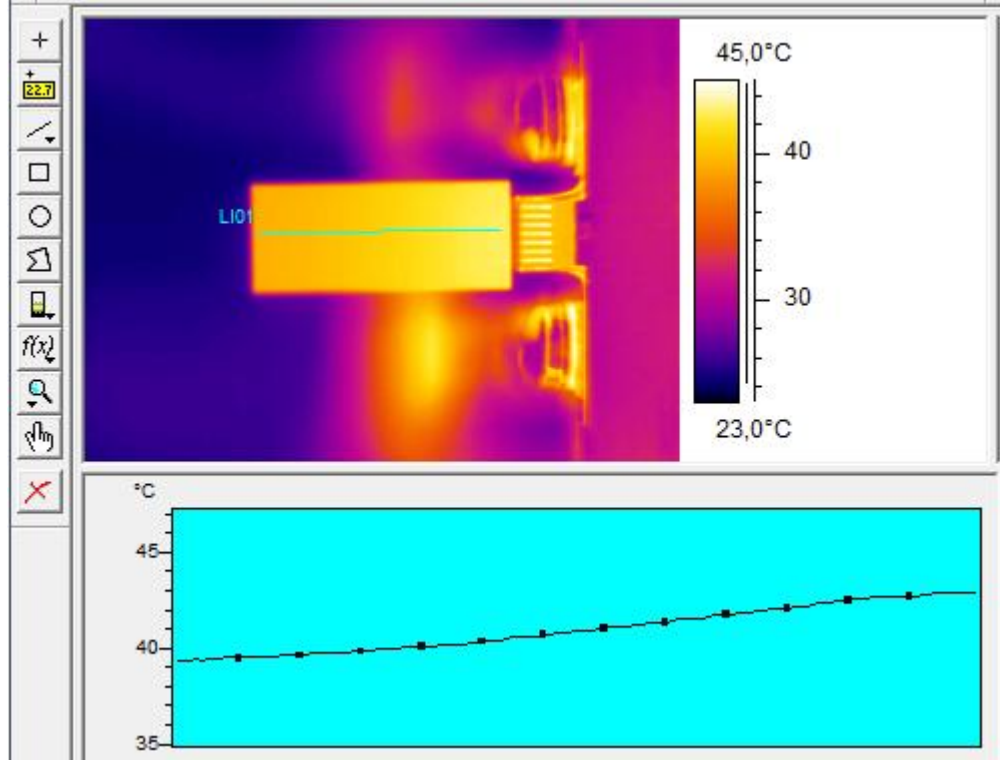
Figure 4.3: Thermographic Analysis in ThermaCAM Software, Crystal under Pumping
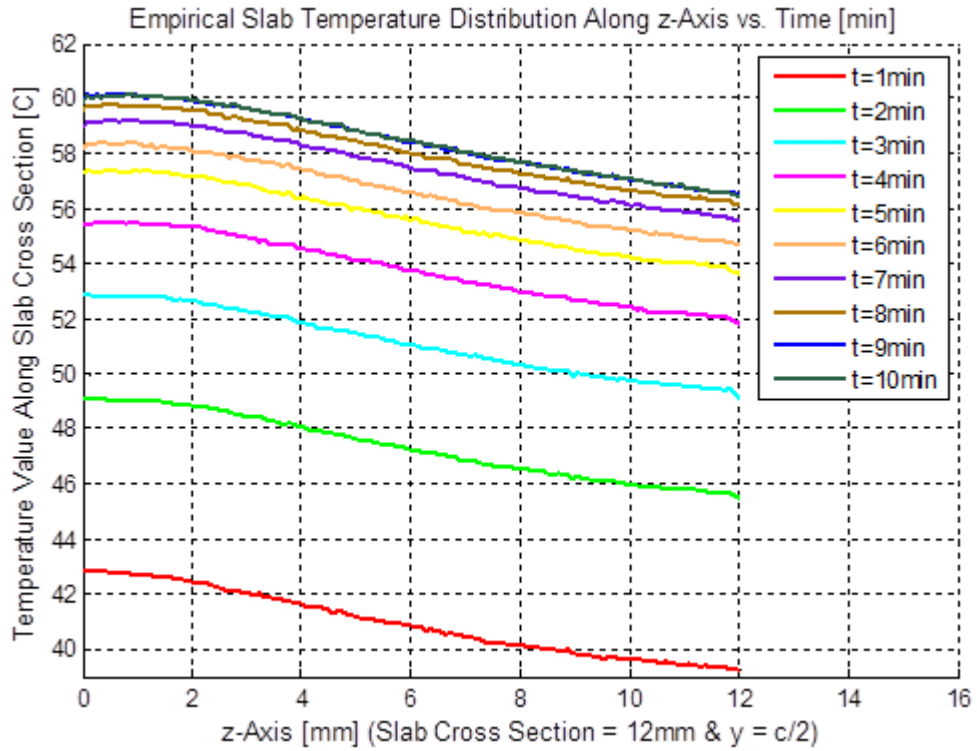
Figure 4.4: Heating Phase - Temperature Values Measured within the Crystal along z-axis at y = 0 Recorded for 20Hz Repetition Rate in 1min. intervals
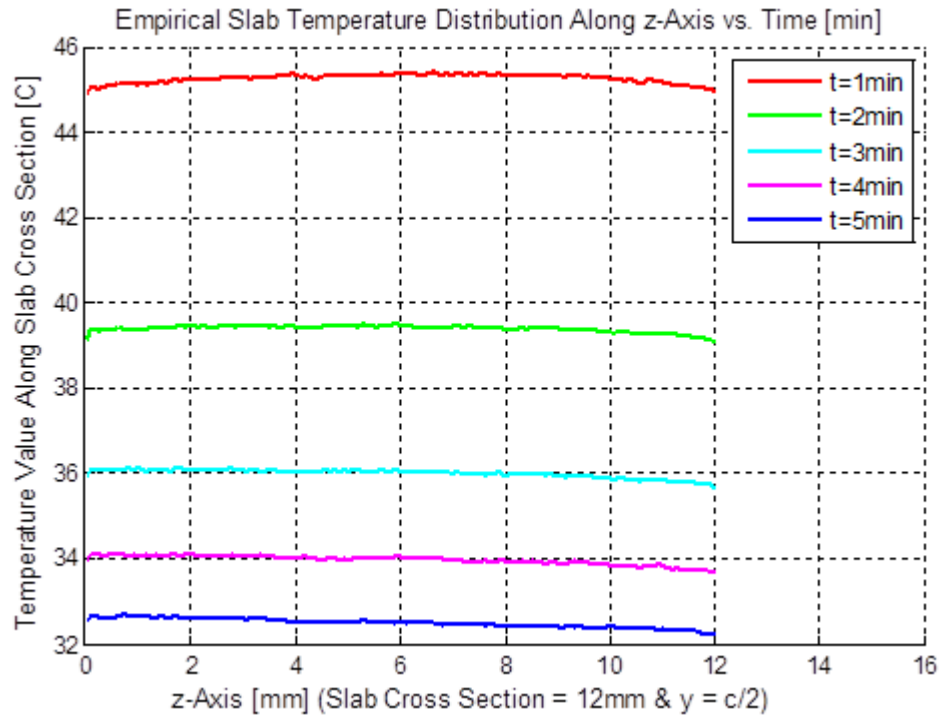
Figure 4.5: Cooling Phase - Temperature Values Measured within the Crystal along z-axis at y = 0 Recorded after Pumping with 20Hz Repetition Rate in 1min. intervals
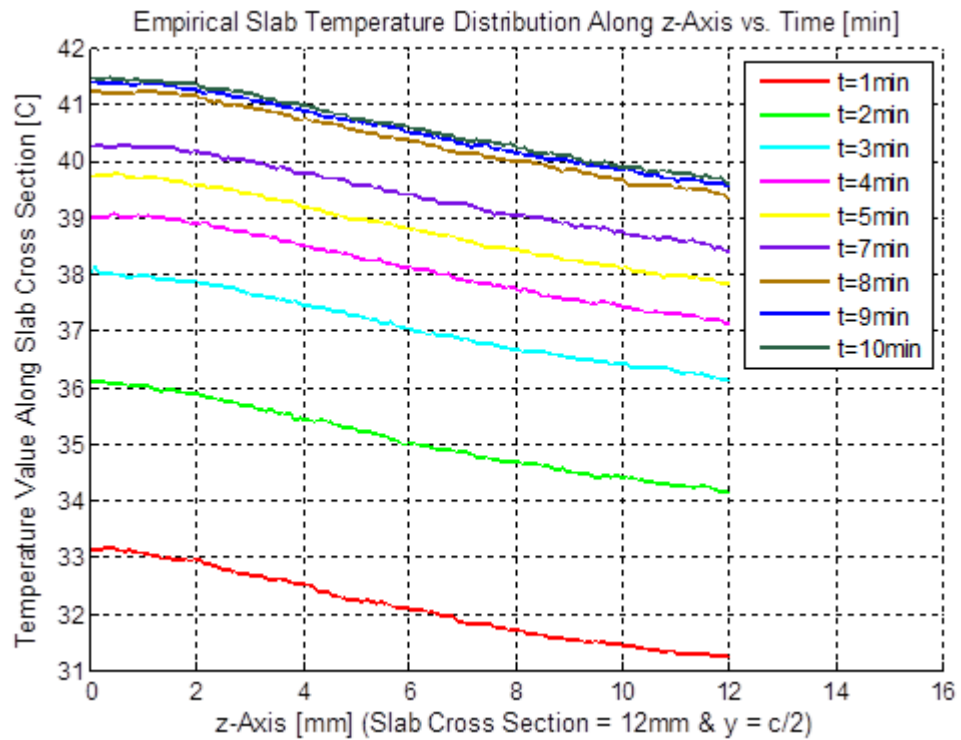
Figure 4.6: Heating Phase - Temperature Values Measured within the Crystal along z-axis at y = 0 Recorded for 10Hz Repetition Rate in 1min. intervals
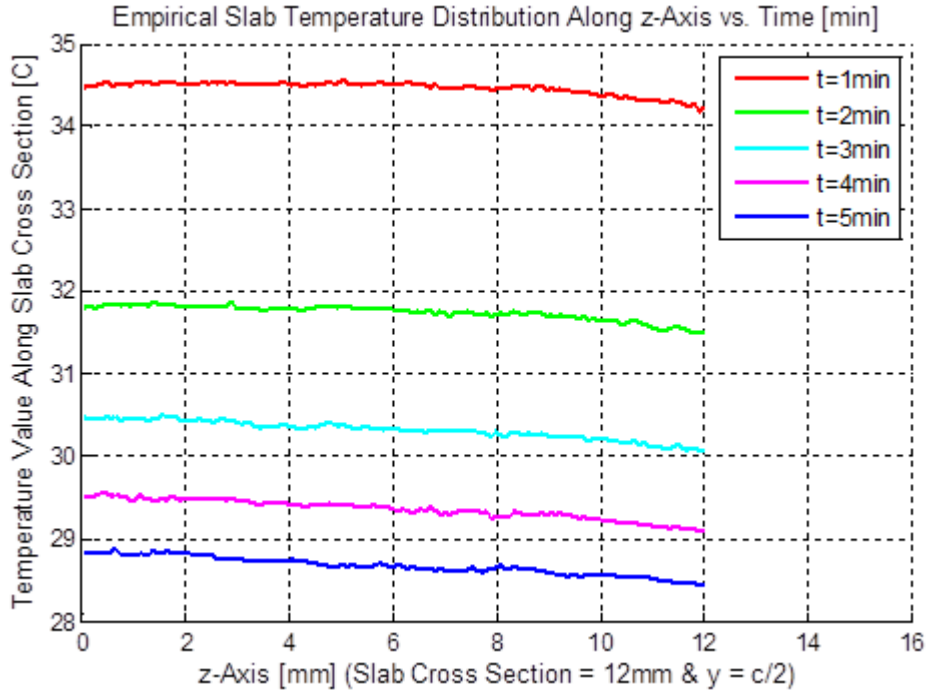
Figure 4.7: Cooling Phase - Temperature Values Measured within the Crystal along z-axis at y = 0
Recorded after Pumping with 10Hz Repetition Rate in 1min. intervals

4.2. Numerical Calculations and Simulations

In this part, firstly the absorbed pump power profiles along the crystal cross section were derived for 20Hz repetition rate. Then using these absorbed power distributions, generated temperature distributions were simulated with varying thermal loading coefficient until obtaining the same results with the empirical measurements.

4.2.1. Calculation of Absorbed Pump Power Profiles on the Fast-Axis across the Crystal

The calculation was carried out for the given setup in Figure 4.1. Numerical computations were implemented in MATLAB by using fundamental rate equations of a 4 level system and the fast-axis pump divergence obtained in chapter 3.

For a monochromatic beam with wavelength of λ, the fraction of the absorbed pump power inside the crystal, A, depends on the density of ground level ions, N_0, absorption cross section, $\sigma_a(\lambda)$, and the length inside the gain medium, L, i.e.:

$$A = \frac{P_{abs}}{P_{in}} = 1 - \exp\left(N_0.\sigma_a\left(\lambda\right).L\right) \tag{4.1}$$

Absorption cross section is the degree of absorption probability in light and matter interaction and is wavelength dependent. The multiplication of ground level ion density with the absorption cross section is called absorption coefficient, $\alpha(\lambda)$, i.e.:

$$\alpha\left(\lambda\right) = N_0.\sigma_a\left(\lambda\right) \tag{4.2}$$

Thus the equation 4.1 can be written in the form:

$$P_{abs}\left(\lambda\right) = Pin\left(1 - e^{-\alpha\left(\lambda\right)L}\right) \tag{4.3}$$

First, the absorption cross section and the ground level ion density at steady state should be calculated in order to obtain absorption coefficient. Wavelength dependent absorption cross section values for

37

Nd:YAG crystal is given in Figure 4.8. Main absorption band of Nd:YAG crystal is in the vicinity of 808nm as seen from this figure.
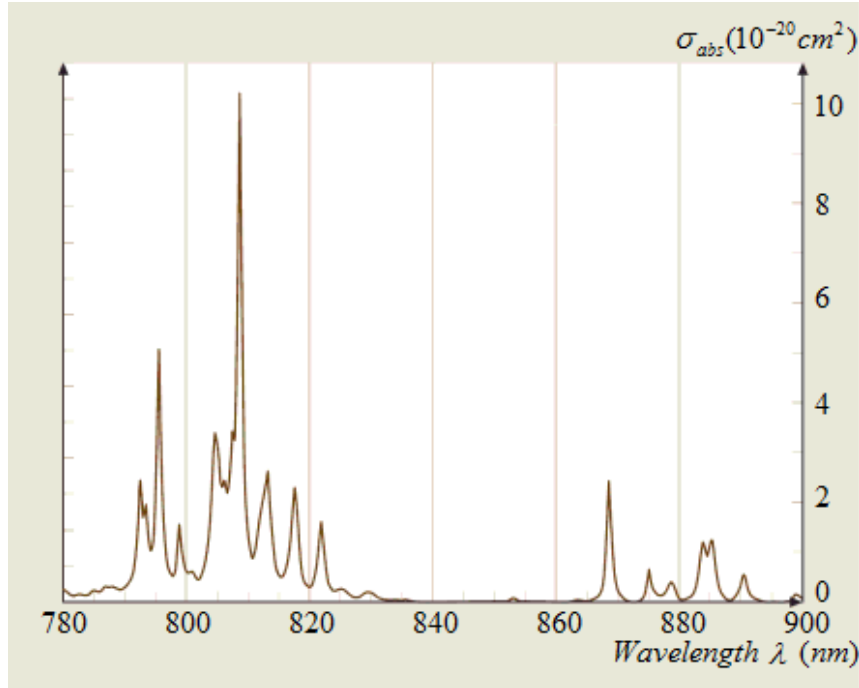
Figure 4.8: Absorption Cross Section Spectrum for 1.1% Doped Nd:YAG [25]

Since laser diode-stacks emits a radiation in a spectral band, instead of using a single value of absorption cross section, the effective absorption cross section $\sigma_{a,eff}$ λ should be computed by using the spectrum in Figure 4.8 and the emission spectrum of laser diode-stack. The emission spectrum, given in Figure 4.9, was measured at 20Hz repetition rate and at 43 ºC. Effective absorption cross section can be calculated through:

$$\sigma_{a,eff}\ \lambda\ \ = \frac{I\ \lambda\ .\sigma_a\ \lambda}{I\ \lambda} \cong 1.85 \times 10^{-20}\ cm^2 \tag{4.4}$$

where, $I\ \lambda$ is wavelength dependent intensity value of laser diode-stack emission spectrum.

Ground level ion density, $N0$, at steady state should be also calculated. To this end, firstly total Nd ion density, N is calculated for 1.1% doped Nd:YAG [26], i.e.:

$$N =\ Nd\ doping\ conc.\ \times 3 \times\ \frac{\rho}{M.W.}\ \times N_A \tag{4.5}$$

where ρ is the density of YAG which is 4.56 g/cm^3, M.W. is the molecular weight of YAG which is $594g/mol$, and N_A is Avagadro's number, i.e. :

$$N = 1.1 \times 10^{-2} \times 3 \times\ \frac{4.56}{594}\ \times 6.022 \times 10^{23} \cong 1.53 \times 10^{20} ions/cm^3 \tag{4.6}$$

A four-level energy scheme is given in Figure 4.10. Before pumping the gain medium, all Nd^{3+} ions stay at ground level, E0. Ground level ion density at steady state will be calculated by using laser rate equations with the obtained values of $\sigma_{a,eff}$ λ and N. Since transitions between the levels E3-E2 and E1-E0 are much faster than the transition between the levels E2-E1, ion populations at E3 and E1 will not be accounted in the given rate equations.
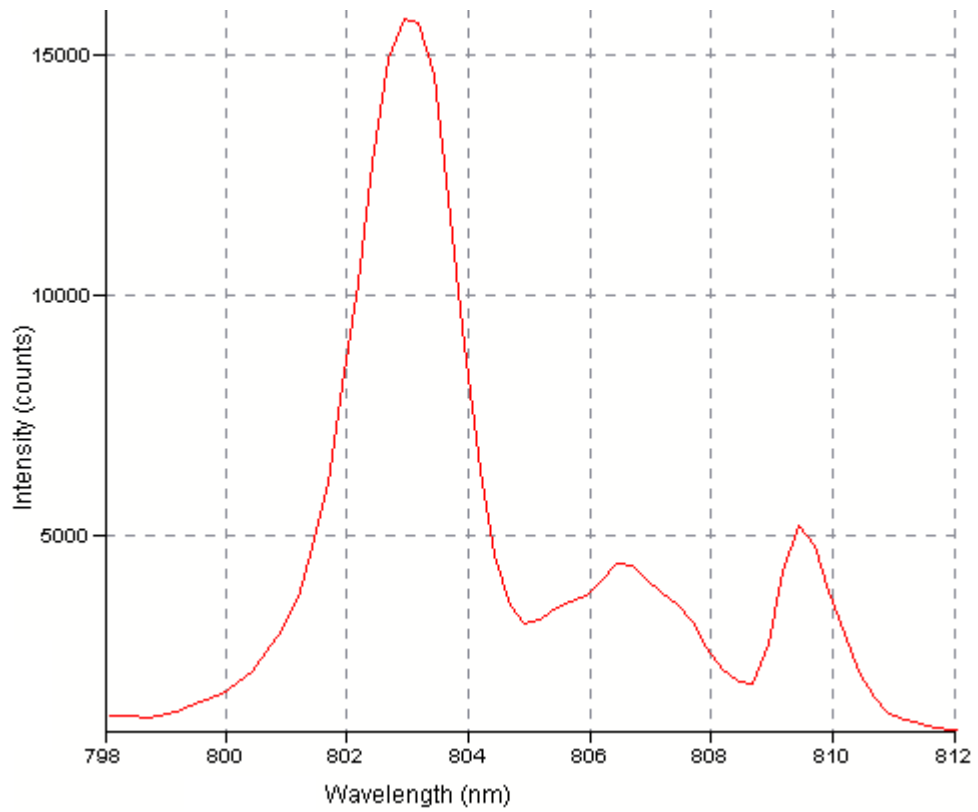
Figure 4.9: Laser Diode-Stack Emission Spectrum at 43 ºC
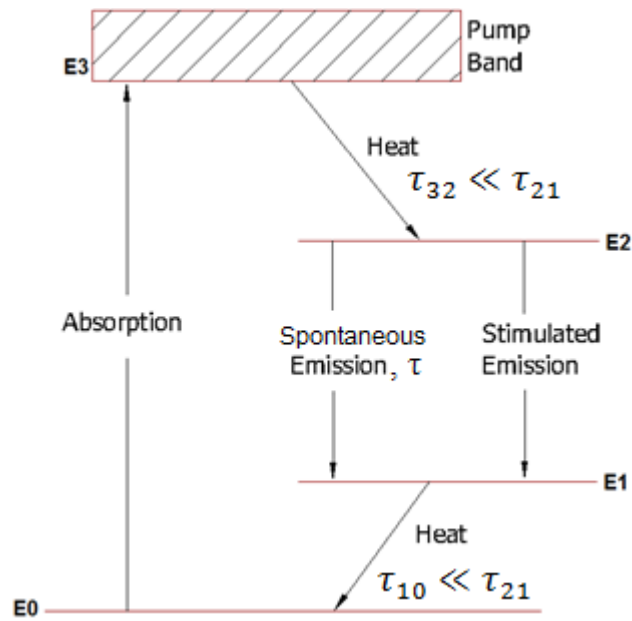
Figure 4.10: Four Level Energy Scheme

Under pumping and no-lasing conditions:

$$\frac{dN0}{dt} = -\sigma_{a,eff} \; \lambda \; . \frac{I_P}{h\nu} . N0 + \frac{N2}{\tau} \tag{4.7}$$

$$\frac{dN2}{dt} = \sigma_{a,eff} \; \lambda \; . \frac{I_P}{h\nu} . N0 - \frac{N2}{\tau} \tag{4.8}$$

$$N = N0 + N2 \tag{4.9}$$

where hv is the energy of a photon in 808nm wavelength, I_P is pump intensity, $N2$ is ion density at energy level E2 and τ is spontaneous emission lifetime which is 230μs for Nd:YAG crystal. In the equations "$(\sigma_{a,eff} \ \lambda \ .I_P)/hv$" is accounted for pumping rate and "$N2/\tau$" is accounted for spontaneous emission. Pumping rate term stands for a decrease in ion density at E0 and thus an increase in ion density at E2, whereas spontaneous emission term stands for a decrease in ion density at E2 and an increase in ion density at E1.

Pump intensity is the pump power divided by the total area. The pump intensity decreases because of absorption while the beam propagating through the crystal. For observing the change in the ground level ion density and the effective absorption coefficient, the pump intensity that is incident on the crystal can be used in the rate equations. The dimensions of the beam at the entrance surface of the crystal at the setup shown in Figure 4.1 is 10mm x 2.8mm on x and y axes, respectively. The measured output power of laser diode-stack with 100A current is 560W. Thus pump intensity becomes:

$$I_P = \frac{560W}{1cm \times 0.28cm} = 2000 \ \frac{W}{cm^2} \tag{4.10}$$

The energy of a photon at 808nm wavelength equals to $2.46 \times 10^{-19} J$. Now rate equations from equation 4.7 to 4.9 can be solved by using all the given values. The change of ground level ion density in 230μs during pumping the gain medium is given in Figure 4.11. There is not so much change in ground level ion density, $N0$, since the crystal is not in a resonator and thus there is not any stimulated emission.
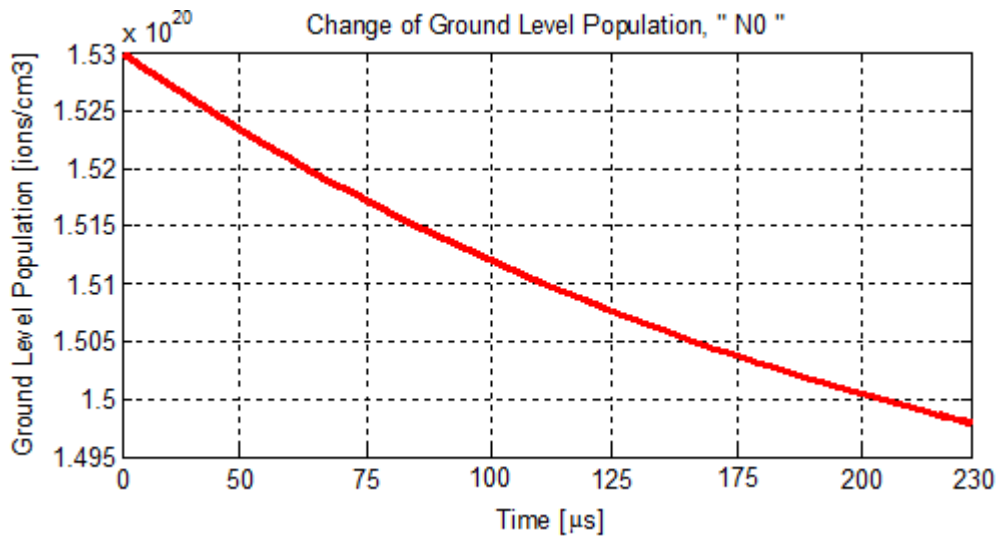
Figure 4.11: The Change of Ground Level Ion Density in a Pulse Duration

The change in effective absorption coefficient, $\alpha_{eff} \ \lambda$ that is calculated through equation 4.2 is given in Figure 4.12. Since the effective absorption coefficient does not change so much in a pulse duration, the average effective absorption coefficient, which is $\alpha_{eff,avg} \ \lambda$ = 2.725, can be used for the absorbed power computation, i.e.:

$$P_{abs} \ \lambda \ = Pin \ 1 - e^{-\alpha_{eff,avg} \ \lambda \ .L} \tag{4.11}$$

In calculation, the gain medium pumping was performed as given in Figure 4.1 in order to be consistent with the thermal measurements. The emission surface of the laser diode-stack was taken almost on the same plane with the entrance surface of slab crystal and only 10mm of slab crystal was pumped out of 70mm. In calculating the absorbed pump power profiles inside the gain medium, the fast-axis pump profiles obtained in chapter 3.2.1.1 were utilized. However, since the refractive index of Nd:YAG ($n_{YAG} = 1.81$) is greater than that of air, the divergence angle of fast-axis pump beam

will be reduced in the crystal as shown in Figure 4.13. Therefore for the calculation of absorbed pump profiles inside the crystal, this change at divergence angle should be taken into account.
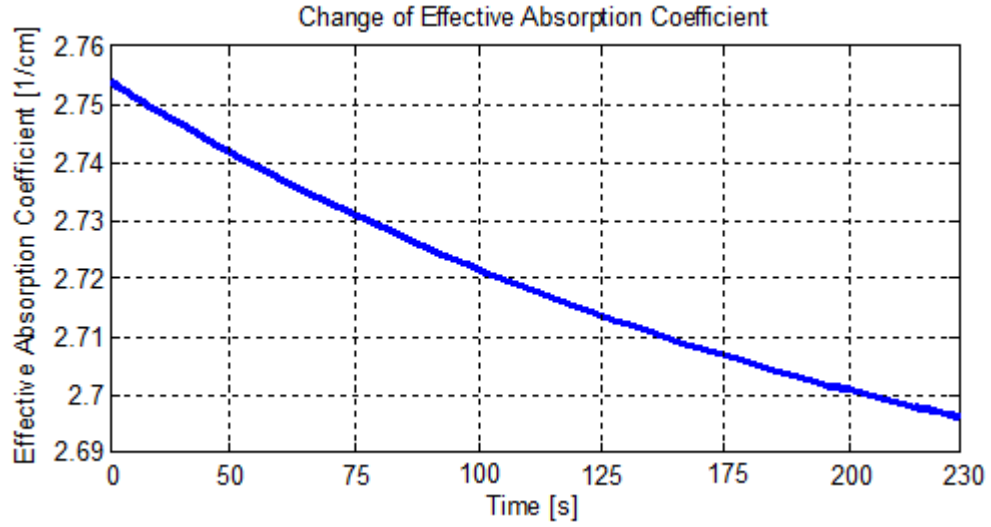
Figure 4.12: The Change of the Absorption Coefficient in a Pulse Duration
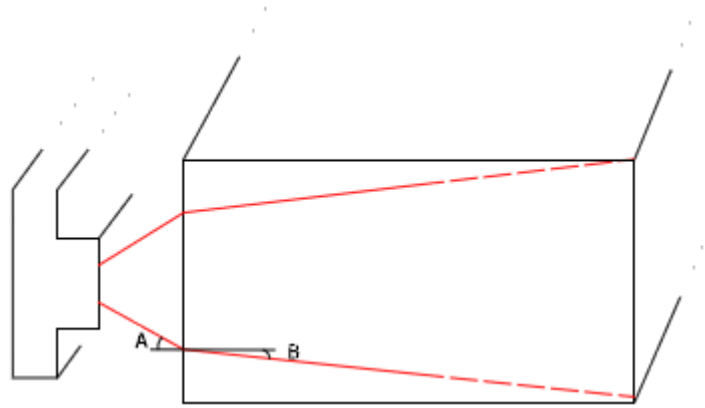
Figure 4.13: Decrease in Divergence Because of Refraction, A>B

where A was found to be 13.62° in chapter 3.2.1.1. The refractive index of Nd:YAG is $n_{Nd:YAG} = 1.81$ and the refractive index of air is $n_{air} = 1$. From Snell's law, divergence angle in the crystal, 2B becomes:

$$n_{air} \times \sin A = n_{Nd:YAG} \times \sin B \tag{4.12}$$

$$B = arc \sin \frac{\sin 13.62°}{1.81} \cong 7.4° \tag{4.13}$$

$$2B = 14.8° \tag{4.14}$$

The absorbed pump power profiles were calculated at 1mm intervals inside the crystal along 12mm as illustrated in Figure 4.14. To this end, measured fast-axis beam profiles in chapter 3.2.1.1 were derived numerically at 1mm intervals in MATLAB by using beam divergence value after refraction. Then absorbed pump power profiles on the fast-axis across the gain medium was computed numerically as given in Figure 4.15 and Figure 4.16.
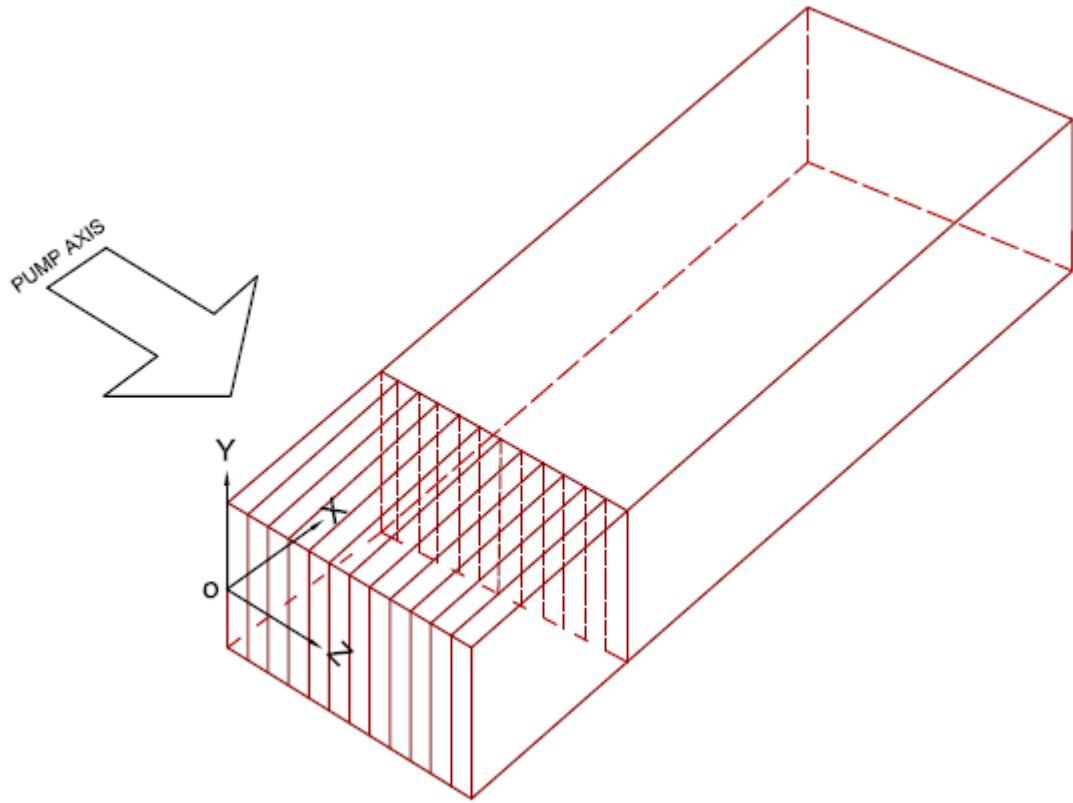
Figure 4.14: Schematic View of Slab Crystal for the Numerical Analysis

The change in absorbed pump power throughout the crystal cross section is given in Figure 4.17. The absorbed pump power is decreasing exponentially while propagating inside the crystal.
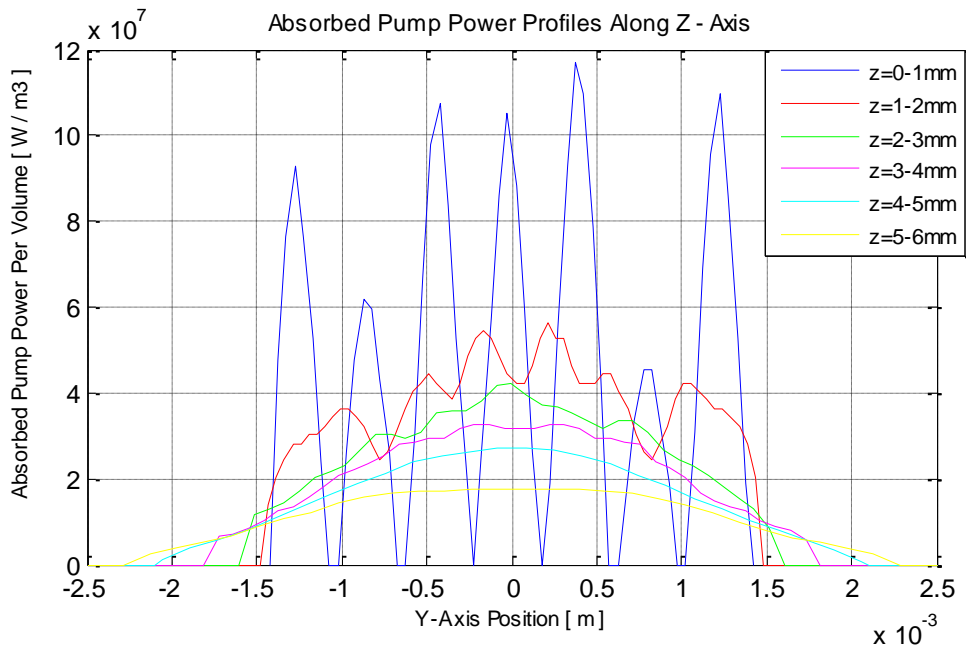
Figure 4.15: Absorbed Pump Profiles at Each Interval across the Crystal – z = 0-6mm
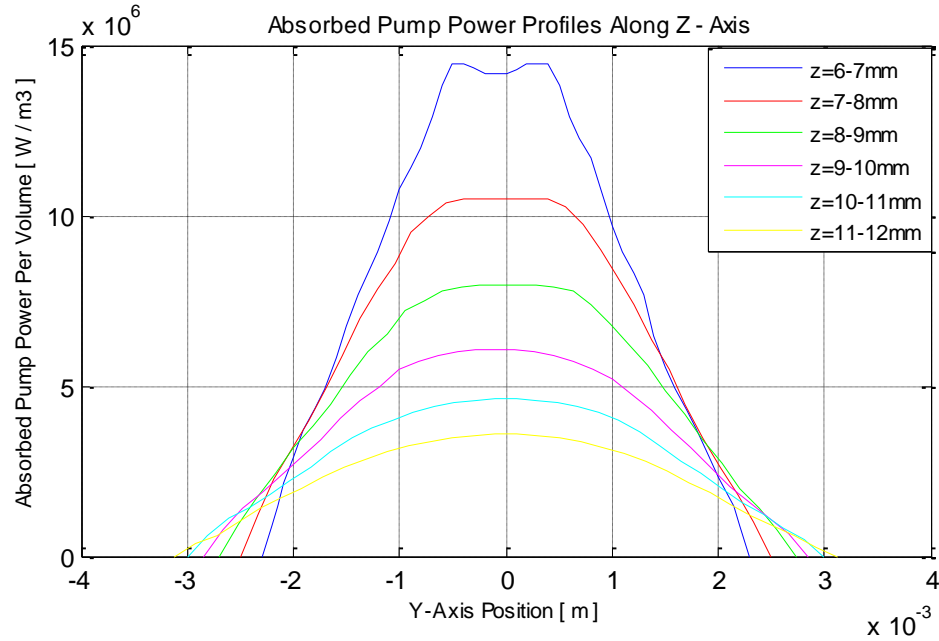
Figure 4.16: Absorbed Pump Profiles at Each Interval across the Crystal − z = 6-12mm
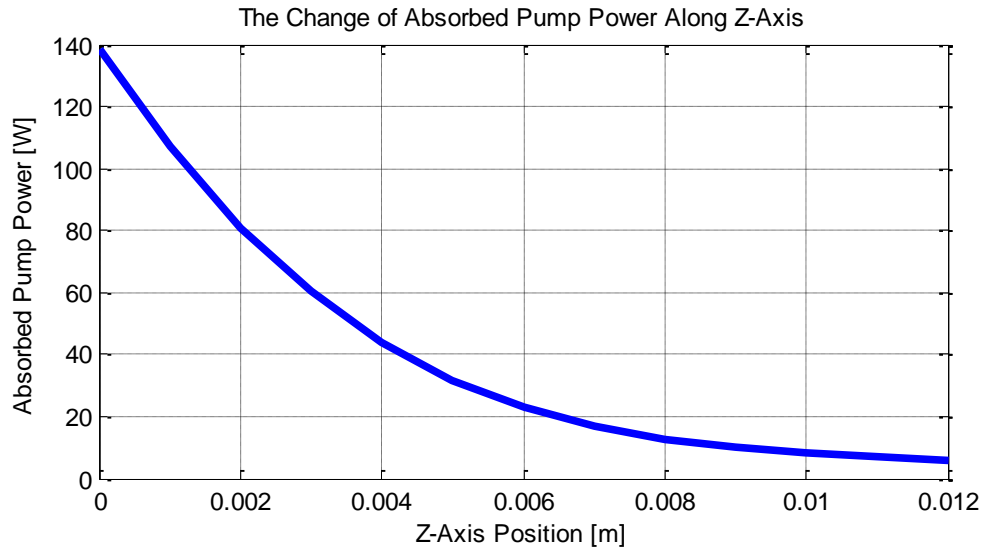
Figure 4.17: Absorbed Pump Power across the Gain Medium

4.2.2. Simulations by CFD Method for Fitting Thermal Loading Coefficient

By using the given absorbed pump power profiles across the slab, the related environmental conditions and Nd:YAG material properties that are given in Table 4.1, thermal loading coefficient was fitted for the same setup given in Figure 4.1. Computation was studied in the commercial CFD analysis software, "FLUENT" that uses finite volume method. Simulations were carried out for 2D line cross section along z-axis and along the middle part of the slab as shown in Figure 4.18. The temperature of any line on x-axis is almost the same since the divergence in slow-axis is low. But there are temperature differences on any line along y-axis because of high fast-axis divergence value, and along z-axis because of absorption.

Table 4.1: Nd:YAG Material Properties That were Used in the Analysis

Material	Density (kg/m³)	Specific Heat (J/kgK)	Thermal Conductivity (W/mK)
Nd:YAG	4550	590	12,90

43
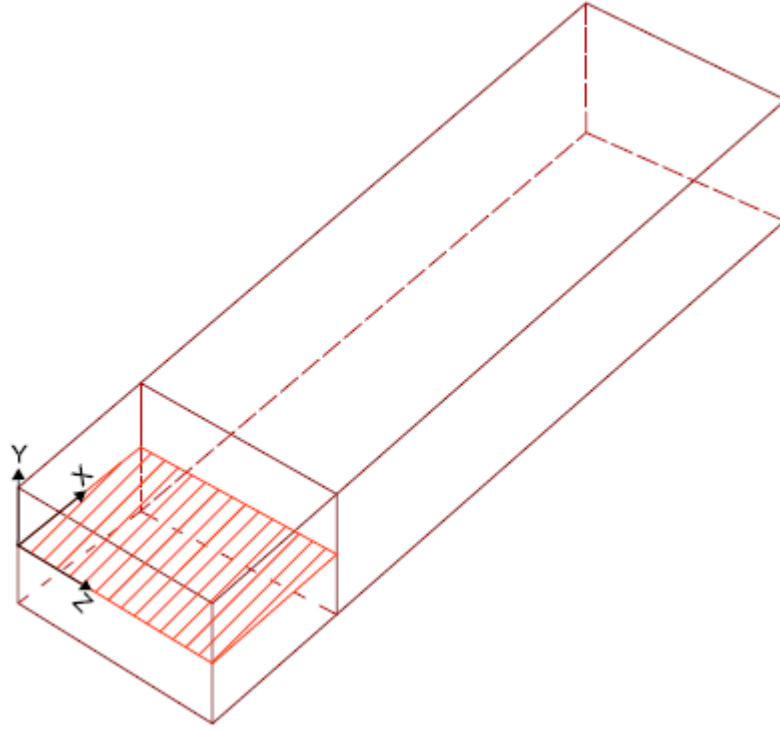
Figure 4.18: 2D Line Cross Section along the Middle Part of the Slab

In the simulations, the temperature distributions along propagation axis (z-axis) were calculated at one minute intervals. The heat convection coefficient was accepted to be constant along the cross section. After each simulation, the results were compared to the measured ones in chapter 4.1 for both 10Hz and 20Hz repetition rates. Best agreement between the simulation and the experimental data was obtained when $\eta_H = 0.39$.

The measurements in chapter 3.1 were taken in clean room where there was airflow which cannot be modeled in the simulations. And this airflow shows its effect especially at elevated temperatures that was reached after five minutes. Therefore comparing the first five minutes of measurements and simulations is more reliable. The comparison of the relevant temperature distributions between measurements and the best matched numerical simulations are shown from Figure 4.19 to Figure 4.22. Figure 4.19 and Figure 4.20 show the temperature distributions along the cross section of the slab while heating up with 10Hz repetition rate and cooling down after driver was turned off, respectively. Figure 4.21 and Figure 4.22 show the temperature distributions along the cross section of the slab while heating up with 20Hz repetition rate and colding down after driver was turned off, respectively.

The fit value of 0.39 is not far from our initial assumption of 0.35 in section 2.2.1 where we showed the effect of thermal lens on the laser beam divergence. Therefore it would be a benefit to improve the pump profile to reduce this effect.

Now by means of the derived thermal loading coefficient, η_H, temperature distribution on the fast-axis or the slow-axis inside the gain medium can be obtained. And by using this temperature distribution, optical distortion or aberration on the laser beam can be calculated.
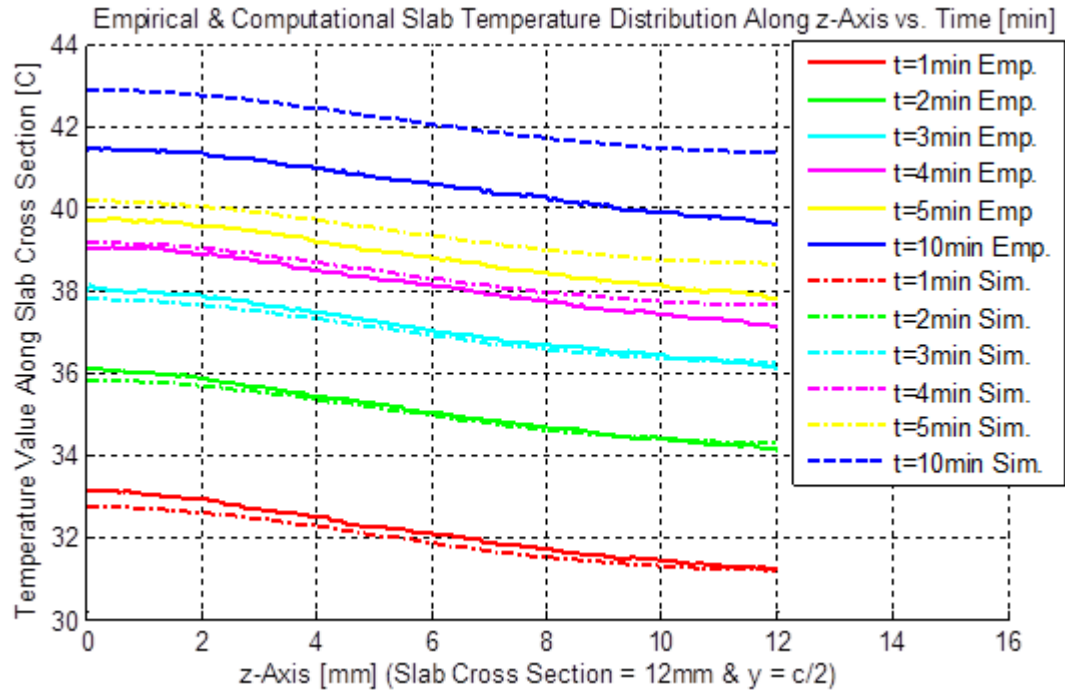
Figure 4.19: Heating Phase - Comparison of CFD Simulations and Thermal Measurements, Recorded for 10Hz Repetition Rate in 1min. Intervals
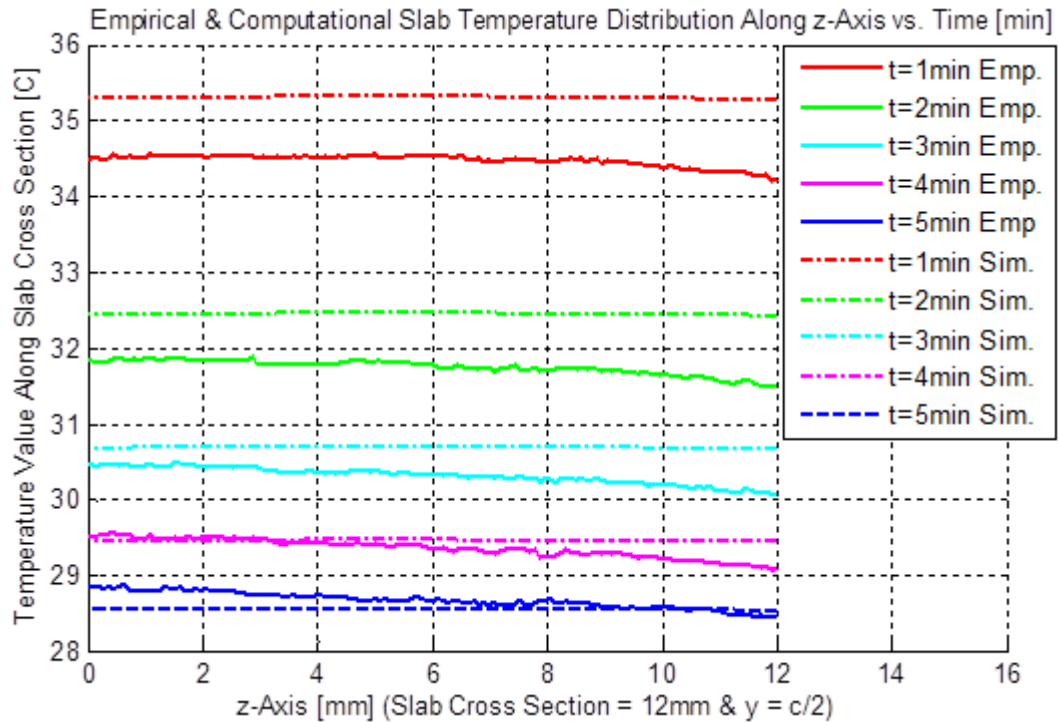
Figure 4.20: Cooling Phase - Comparison of CFD Simulations and Thermal Measurements, Recorded after Pumping with 10Hz Repetition Rate in 1min. Intervals
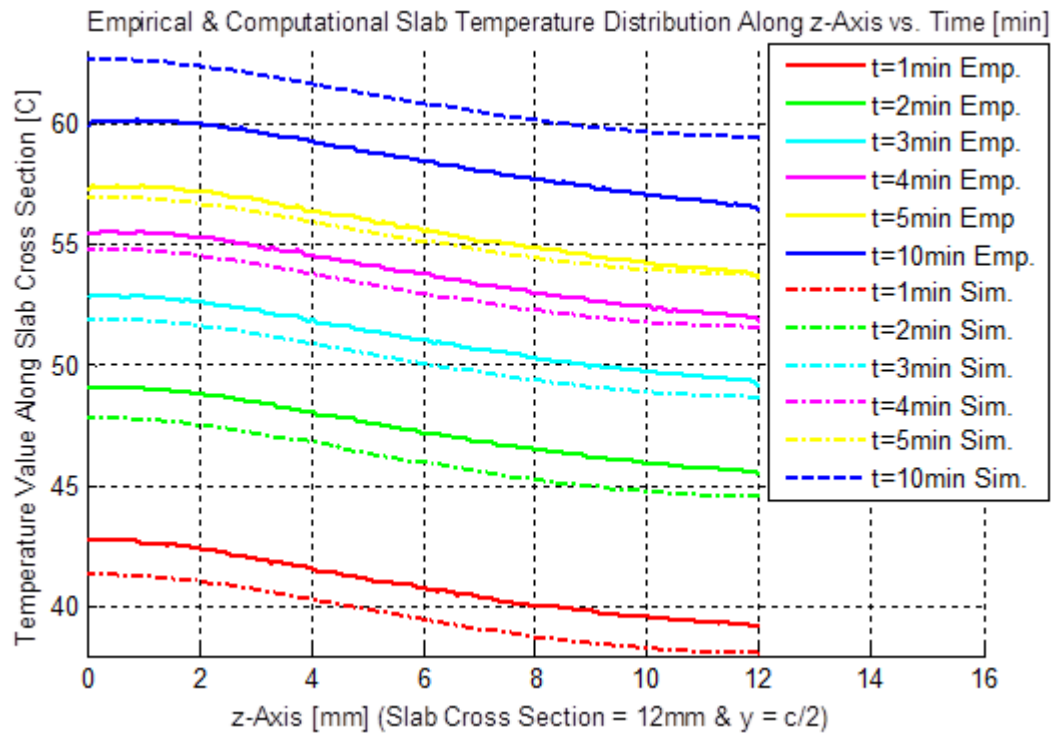
Figure 4.21: Heating Phase - Comparison of CFD Simulations and Thermal Measurements, Recorded for 20Hz Repetition Rate in 1min. Intervals
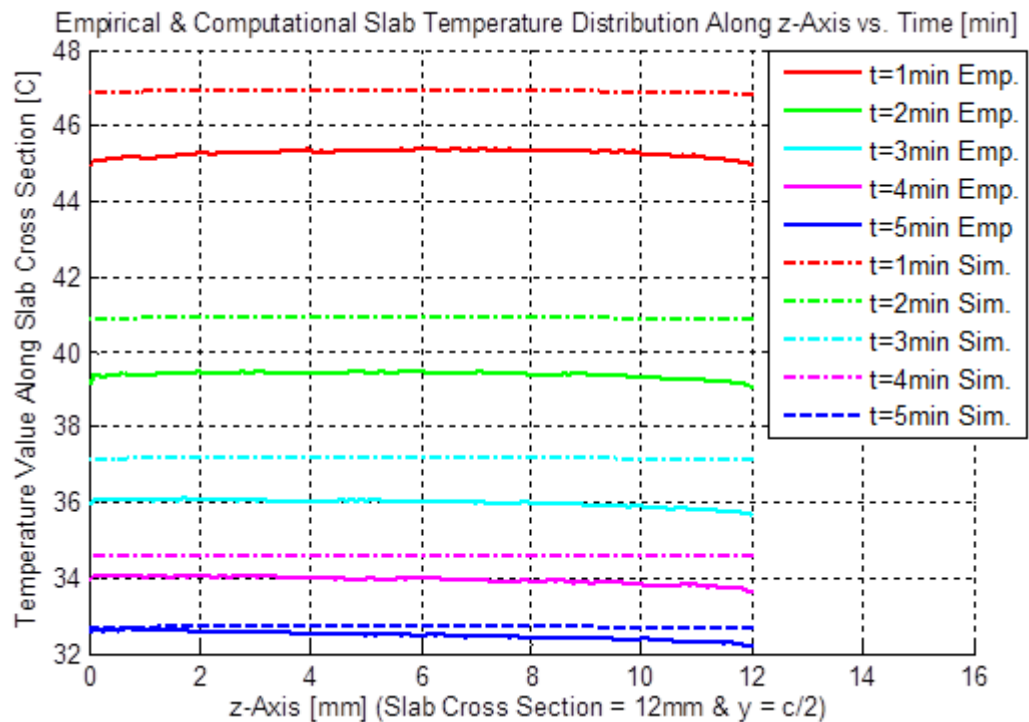
Figure 4.22: Cooling Phase - Comparison of CFD Simulations and Thermal Measurements, Recorded after Pumping with 20Hz Repetition Rate in 1min. Intervals

CHAPTER 5

COMPUTER AIDED PUMP CHAMBER DESIGN METHOD THROUGHOUT A SPECIFIC DESIGN

In this chapter, a pump chamber design was carried out in the optical design software, ZEMAX. In part 2.2.1 it is shown that there is a quadratic relationship between absorbed pump profile and temperature distribution inside the gain medium. Designing a pump chamber that results in a uniform temperature distribution inside the gain medium is the ideal case for eliminating thermal lens and optical distortions. However, the generated heat inside the crystal should be removed by means of a heat sink structure, and the heat sink also affects the formed temperature distribution inside the crystal. For this reason, obtaining a pump chamber structure that results in uniform temperature distribution inside the gain medium is not a simple task. Such a pump profile may not be the one that maximizes system efficiency. But it is a well known fact that pumping the gain medium by uniform pump profile is one of the best pumping distributions for system efficiency in side-pumped solid-state lasers and also it is shown in section 2.2.1 that pumping the gain medium with such a pump profile significantly reduces thermal lens and thus the laser beam divergence. As a result, by modeling the characterized diode-stacks as the pump source and using a crystal that has a $6 \times 6mm$ cross-section dimensions, a transferring optical structure that results in a uniform pump profile across the gain medium was designed in this chapter by means of near-field beam profiles and beam divergence found in chapter 2.

First of all, the beam uniformity merit should be defined for the pump chamber design. Uniformity can be defined as absolute change on beam profile. To this end, absolute of numerical derivatives on any normalized beam profile inside 90% of total energy was summed and averaged to the number of intervals on which derivatives were taken. The formulation is given in equation 5.1 and an illustration for uniformity calculation is given in Figure 5.1. Let's consider the blue line to be a beam profile and the red line to be the calculated derivatives at each interval as indicated in the figure. The less the value of uniformity value, ψ, given in equation 5.1 is, the more uniform beam distribution is obtained.
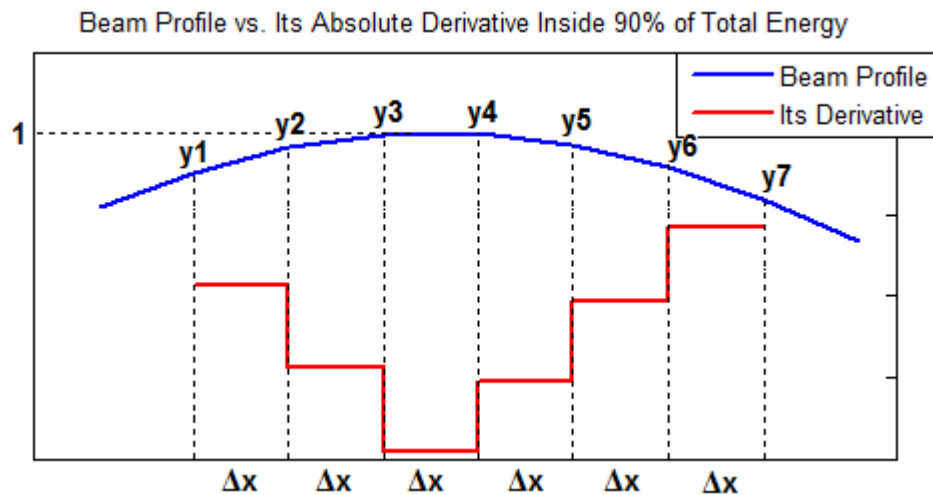
Figure 5.1: An Illustration for Uniformity Calculation
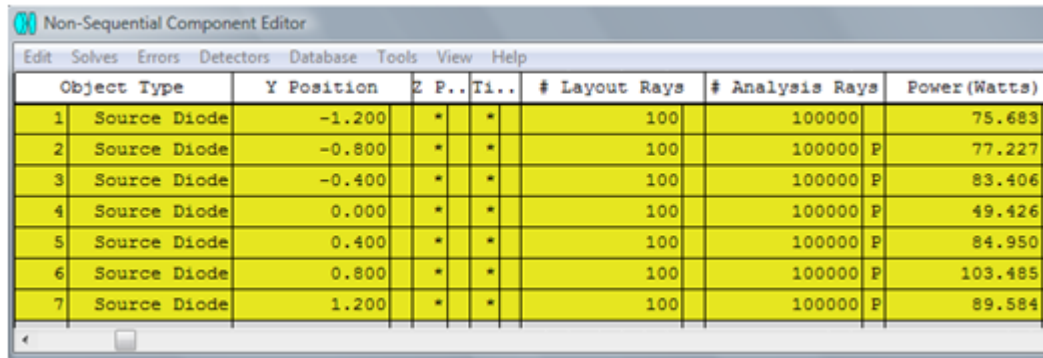
$$\Psi = \frac{_i\,abs\ \dfrac{dy}{dx}}{i} = \frac{_i\,abs\ \dfrac{y_{i+1}-y_i}{\Delta x}}{i} \tag{5.1}$$

The pump chamber design was studied in ZEMAX which is usually used in industry for combining sequential optical design, optimization, tolerancing, analysis of any optical system design, physical optics analysis and non-sequential optical system design. The software consists of three parts: sequential ray tracing, non-sequential ray tracing and mixed mode. Optimization is performed in sequential and mixed modes while analysis of an optical system is performed in non-sequential part.

The objective of the design was to obtain a uniform pump profile across the gain medium in a distance between the diode-stack and the gain medium as small as possible. In case there is no any transferring optical structure between the pump source and the gain medium, the uniformity was calculated to be 0.3068 as given in section 6.1.1. Various pump chamber configurations were investigated and realized in the software to decrease this value for increasing uniformity. The advantages and disadvantages of these configurations will be mentioned briefly in this chapter. Then the resulting configuration will be discussed in detail.
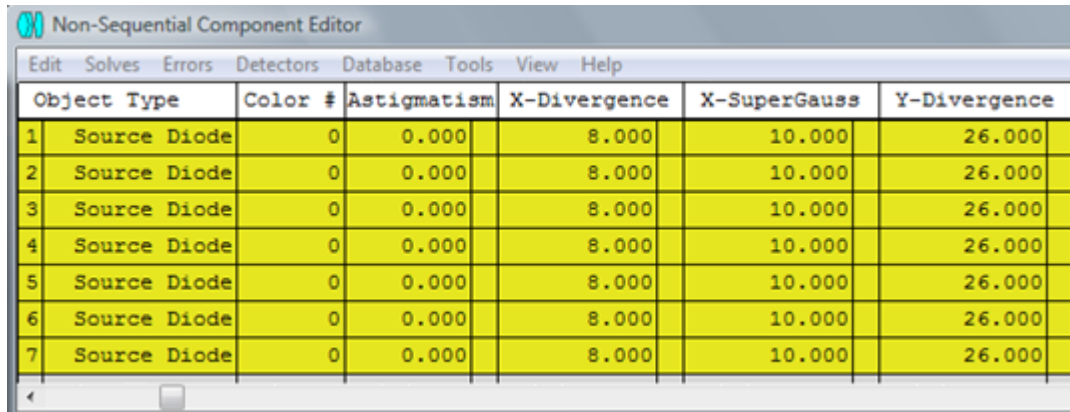
5.1. Laser Diode-Stack (Source) Modeling in ZEMAX

First of all, the specifications of laser diode-stack were imported in the software. Since there are seven arrays in a stack, seven "Source Diodes" were defined as shown in Figure 5.2 which shows non-sequential component data editor of ZEMAX. The vertical distance between arrays is 0.4mm as given in chapter 3. Thus, arrays positioned 0.4mm away from each other on y-axis. The diode characterization measurements were utilized in defining relative power of each array, x-divergence and y-divergence values of the pump source. The measured "X-Divergence" and "Y-Divergence" values were imported as shown in Figure 5.3.

	Object Type	Y Position	Z P..	Ti..	# Layout Rays	# Analysis Rays		Power (Watts)
1	Source Diode	-1.200	*	*	100	100000		75.683
2	Source Diode	-0.800	*	*	100	100000	P	77.227
3	Source Diode	-0.400	*	*	100	100000	P	83.406
4	Source Diode	0.000	*	*	100	100000	P	49.426
5	Source Diode	0.400	*	*	100	100000	P	84.950
6	Source Diode	0.800	*	*	100	100000	P	103.485
7	Source Diode	1.200	*	*	100	100000	P	89.584

Figure 5.2: Position and Relative Power Definitions of Source Diode in ZEMAX

	Object Type	Color #	Astigmatism	X-Divergence	X-SuperGauss	Y-Divergence
1	Source Diode	0	0.000	8.000	10.000	26.000
2	Source Diode	0	0.000	8.000	10.000	26.000
3	Source Diode	0	0.000	8.000	10.000	26.000
4	Source Diode	0	0.000	8.000	10.000	26.000
5	Source Diode	0	0.000	8.000	10.000	26.000
6	Source Diode	0	0.000	8.000	10.000	26.000
7	Source Diode	0	0.000	8.000	10.000	26.000

Figure 5.3: Source Diode - X and Y Divergence Values Definitions in ZEMAX

Super-Gaussian values and the emitter specifications were also imported as given in Figure 5.4. Super-Gaussian value is related to the shape of emitted Gaussian beam profile for each emitter on x

and y axes. There are 40 emitters along x-axis, and 1 emitter along y-axis for each array. The distance between two emitters is 250μm. The x-width of each emitter is 102μm while y-width is 0.5μm.

The imported seven diode arrays were simulated by tracing 100 million rays. And the resulting fast-axis beam profiles were observed at distinct distances on z-axis by placing the detector surfaces to see whether they overlap with the measurements that were given in chapter 3. Figure 5.5 and Figure 5.6 are the two results that compare the beam profiles obtained from simulations and measurements.

	Object Type	Y-SuperGauss	Number X	Number Y	Delta X	Delta Y	X-Width	X-Width Hx	Y-Width	Y-Width Hy
1	Source Diode	1.000	40	1	0.250	0.00	0.102	10.00	0.0005	1.000
2	Source Diode	1.000	40	1	0.250	0.00	0.102	10.00	0.0005	1.000
3	Source Diode	1.000	40	1	0.250	0.00	0.102	10.00	0.0005	1.000
4	Source Diode	1.000	40	1	0.250	0.00	0.102	10.00	0.0005	1.000
5	Source Diode	1.000	40	1	0.250	0.00	0.102	10.00	0.0005	1.000
6	Source Diode	1.000	40	1	0.250	0.00	0.102	10.00	0.0005	1.000
7	Source Diode	1.000	40	1	0.250	0.00	0.102	10.00	0.0005	1.000

Figure 5.4: Specifications for SuperGauss Values and Emitter Properties in ZEMAX

We see from the plots that simulated and measured beam profiles match well. Thus the imported seven diode arrays can be used in the simulations as the laser diode-stack while designing the pump chamber in ZEMAX.
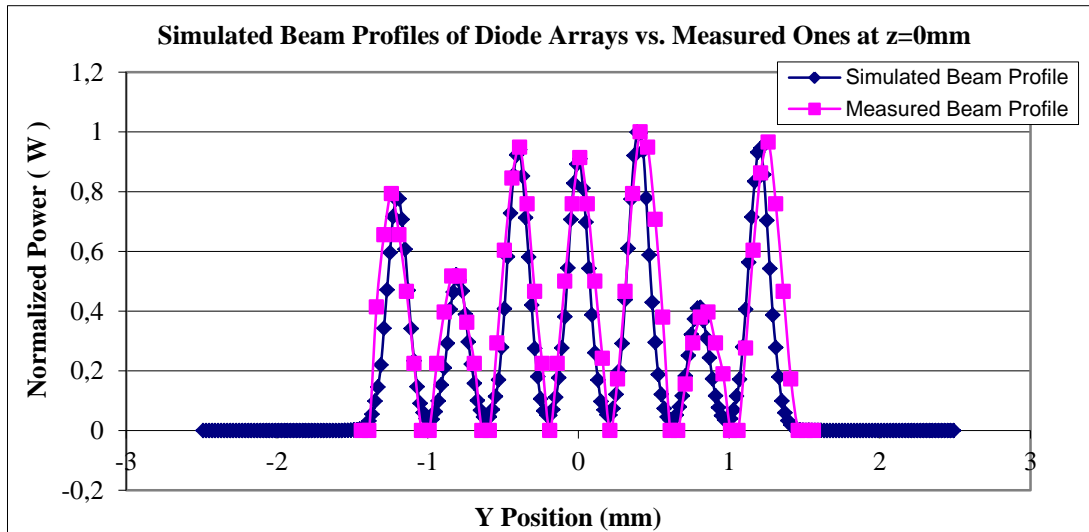
Figure 5.5: Fast-Axis Beam Profiles; Measurements vs. Simulations at z = 0mm
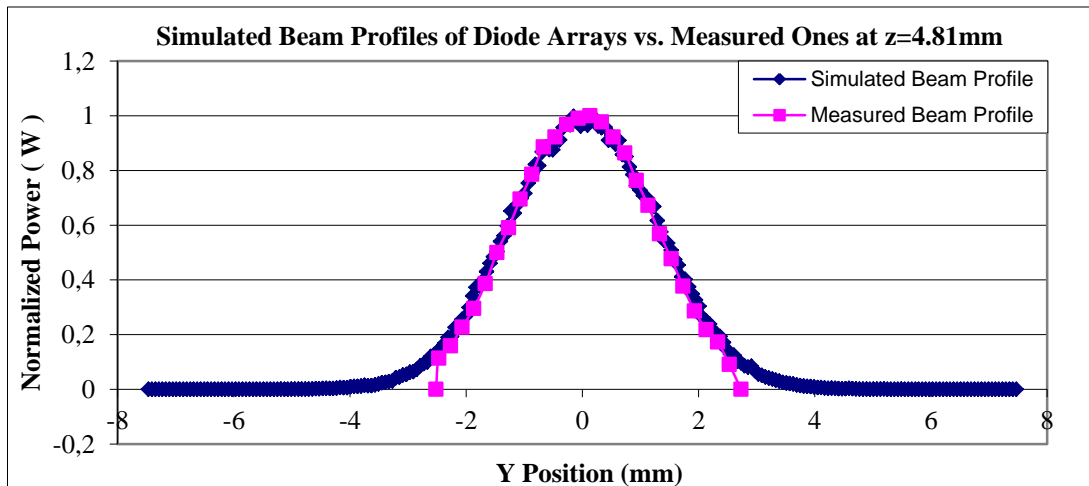
Figure 5.6: Fast-Axis Beam Profiles; Measurements vs. Simulations at z = 4.81mm

49

5.2. Studied Pump Chamber Configurations in ZEMAX

The first idea to get a uniform pump distribution across the crystal was collimation of emitted pump beam. Firstly, a single bi-convex cylindrical lens was optimized by the merit of yielding maximum uniformity across the crystal. The shaded model, 2D layout and the fast-axis beam profile at the entrance surface of the crystal in the resulting design are given in Figure 5.7, Figure 5.8 and Figure 5.9, respectively.
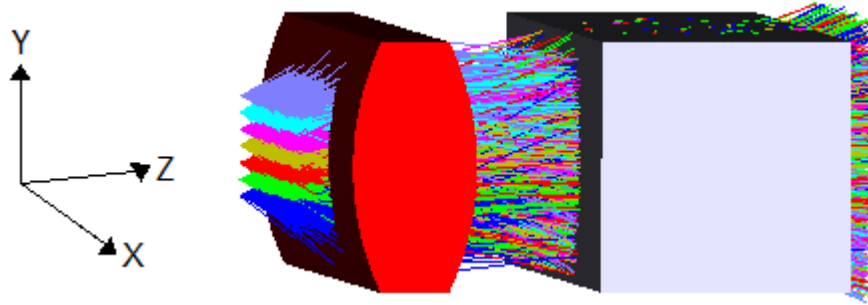
Figure 5.7: Shaded Model – Collimation with Cylindrical Bi-Convex Lens

The lower and upper surfaces of the laser crystal are ground surfaces which means they are diffuse reflectors. In all the simulations these surfaces were modeled as 0.05 Lambertian (ground) reflectors. Also in all the simulations, 99% AR coating at 808nm was applied to side surfaces of the laser crystal and 98% AR coating at 808nm was applied to clear apertures of all the lenses. The absorption coefficient found in chapter 3 was used for Nd:YAG.
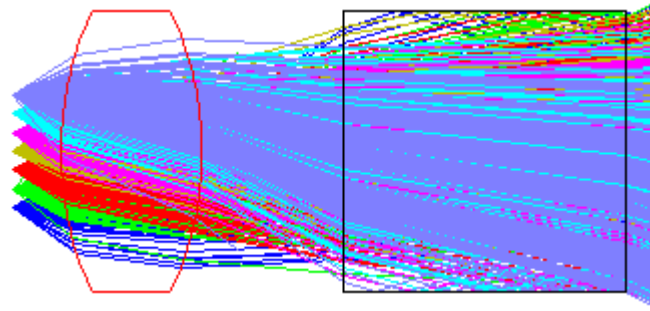
Figure 5.8: 2D Layout – Collimation with Cylindrical Bi-Convex Lens
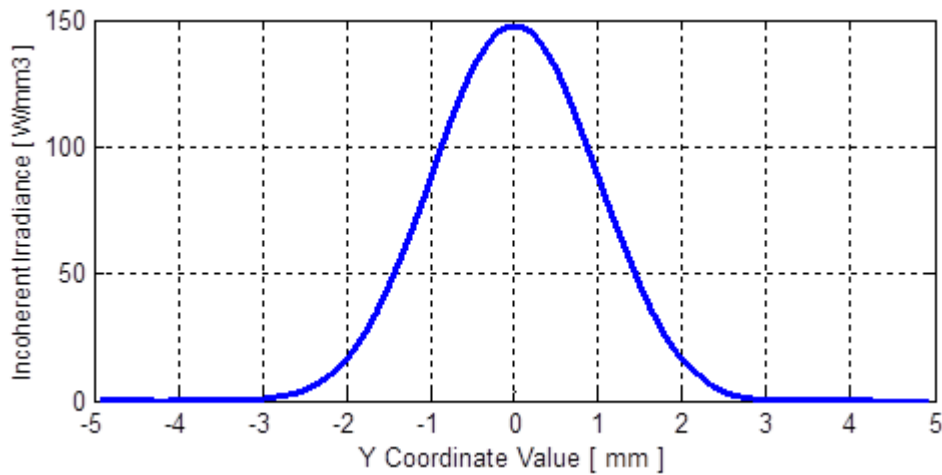
Figure 5.9: Fast-Axis Beam Profile - Collimation with Cylindrical Bi-Convex Lens

The uniformity of the bi-convex setup is calculated as $\Psi = 0.44$ by means of the equation 5.1. The calculated normalized absolute numerical derivative plot is given in Figure 5.10. The uniformity was

not improved because of spherical aberration that is observed when working with a single spherical lens. That means the focal length of the lens changes with its clear aperture, so the focal length of the lens differs for each diode array. Therefore obtaining a nearly top hat beam profile of emitted beam from diode-stacks with a single cylindrical bi-convex lens is not feasible. A top hat beam profile can be achieved by means of using more than one such cylindrical lenses, but this will reduce transmission value because of back reflections and absorption of the lenses.
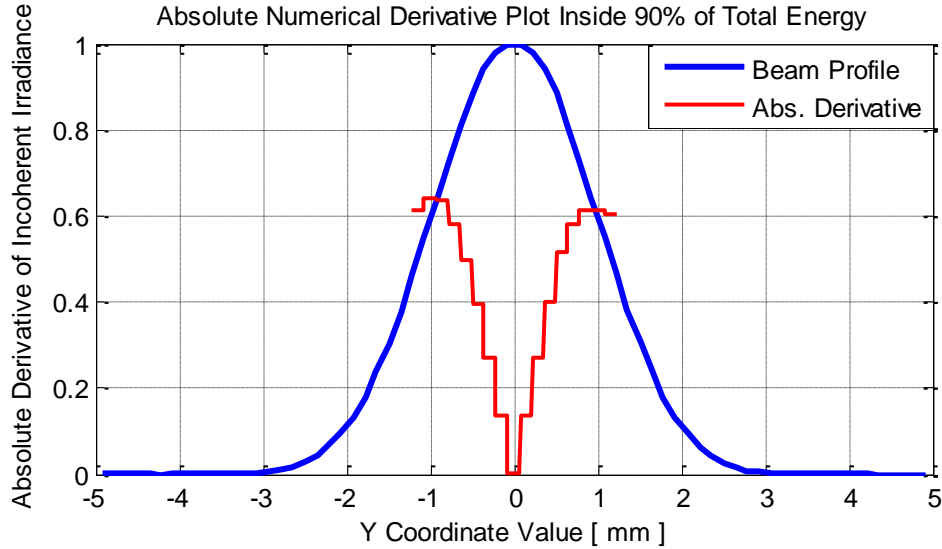
Figure 5.10: Normalized Absolute Numerical Derivative – Cylindrical Lens Design

A micro lens collimation structure was optimized in order to eliminate spherical aberration and keeping transmission value in a high level. Seven identical micro cylindrical lenses were placed in front of diode arrays as shown in shaded model in Figure 5.11 and in 2D layout in Figure 5.12. Thus the optical power of a single lens was distributed to seven lenses on which the emitted beam from each array hits the same clear aperture and as a result spherical aberration was decreased.
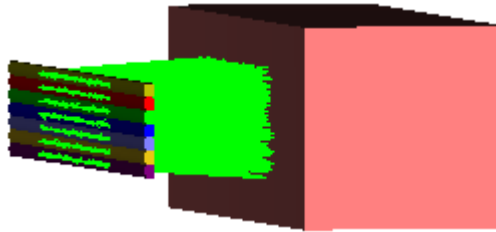
Figure 5.11: Shaded Model – Collimation with Micro Lenses
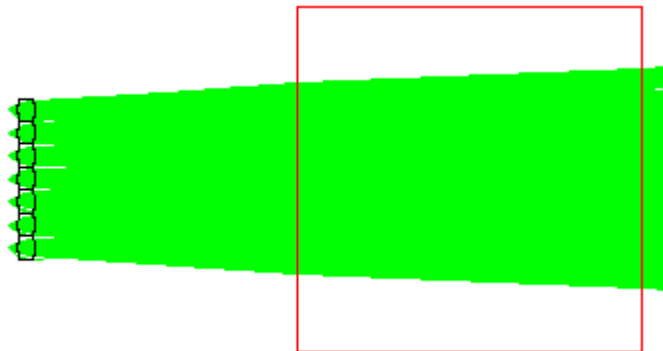
Figure 5.12: 2D Layout – Collimation with Micro Lenses

Figure 5.13 shows the beam profile at the entrance surface of the gain medium, whereas Figure 5.14 shows the normalized absolute derivative inside 90% of total energy with the beam profile itself. Uniformity was calculated to be $\Psi = 0.25$.

51
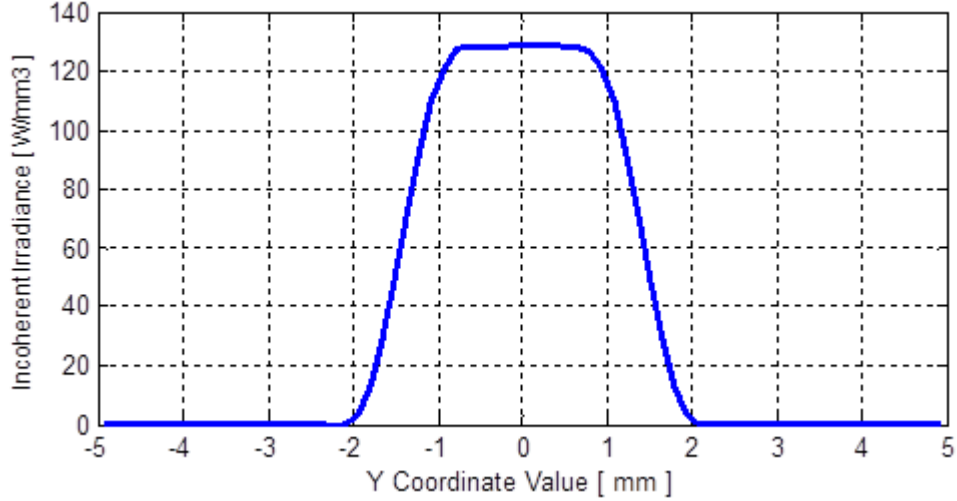
Figure 5.13: Fast-Axis Beam Profile - Collimation with Micro Lenses
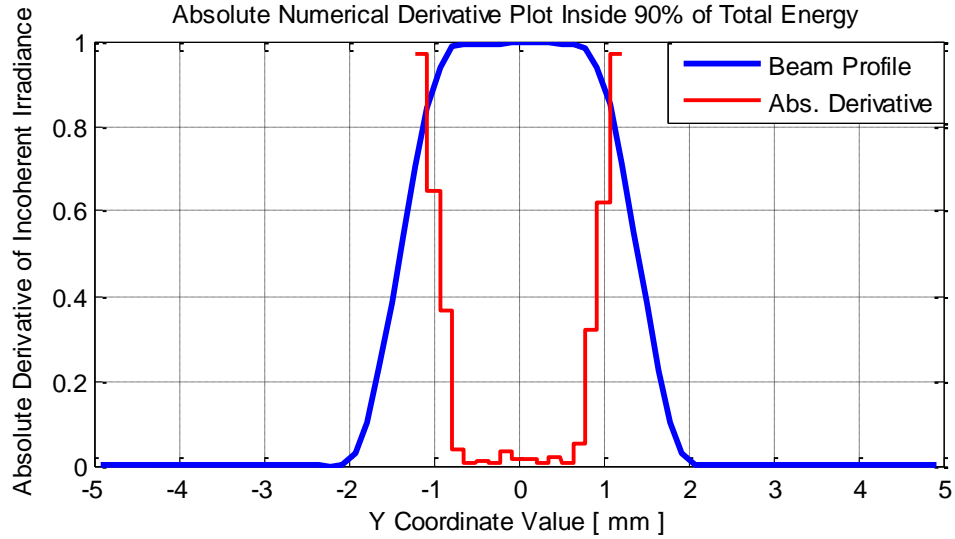
Figure 5.14: Normalized Absolute Numerical Derivative – Design with Micro Lenses

Although the uniformity of the design is improved, the manufacturability of such cylindrical micro lenses is very difficult and expensive. And also mechanical mounting tolerances for the lenses are very tight. Furthermore, only 4mm out of 6mm of the crystal cross section is pumped by this design and thus a significant number of ions doped to the crystal cannot be excited. This brings a reduction in the system efficiency. Therefore another configuration was needed.

5.3. Final Pump Chamber Design Configuration

Since the divergence angle on the fast-axis has a high value, the emitted beams from the diode-stack arrays merge into each other as propagating in the space. In order to transfer the diverged beam into the gain medium and let the beams merge into each other while propagating, two parallel mirrors which are polished and high reflection (HR) coated can be utilized as shown in Figure 5.15 and Figure 5.16. There is one degree of freedom in such a design: the distance, d, between the laser diode-stack and the crystal. This distance was optimized for the merit of obtaining acceptable uniformity (See Figure 5.25).

When $d \geq 16mm$, the uniformity value reaches a very low value and remains almost constant after that (See Figure 5.25). The resulting pump profiles at the entrance and exit surfaces of the crystal are given in Figure 5.17 and 5.18, respectively. The normalized absolute numerical derivative plot inside

52

90% of total energy of the pump distribution at the entrance surface of the crystal is given in Figure 5.19. The uniformity is found to be $\Psi = 0.0632$.
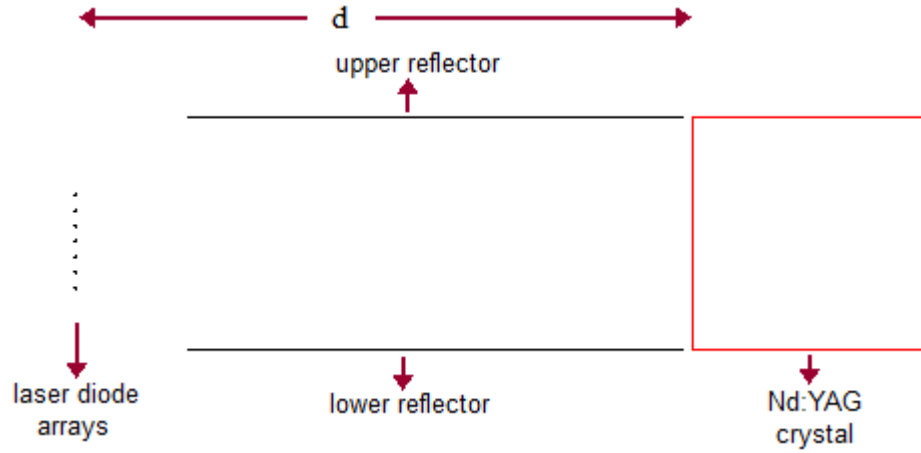
Figure 5.15: 2D Layout of the Design with the Reflectors
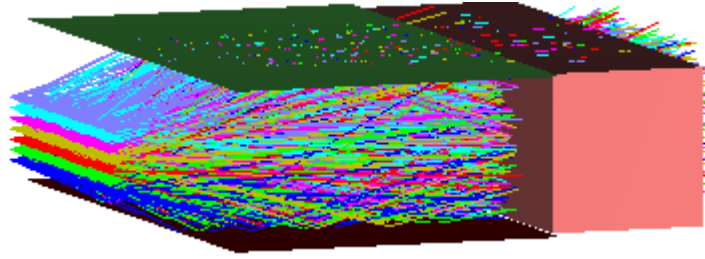
Figure 5.16: Shaded Model of the Design with the Reflectors

The volume of a laser source is very important engineering parameter and should be minimal. So the distance, d is very critical in such a pump chamber design and should be also minimal in most cases. A plano-concave cylindrical lens can be used in front of the diode-stack to reduce the distance, d. If emitted pump beams are diverged by means of a cylindrical plano-concave lens, the merge of beams occurs in a short distance as shown in Figure 5.20. Again two parallel mirrors can be used in order to transfer the diverged beam into the gain medium and let the beams merge into each other while propagating. The ZEMAX layout and shaded models of the design are given in Figure 5.21 and Figure 5.22, respectively.
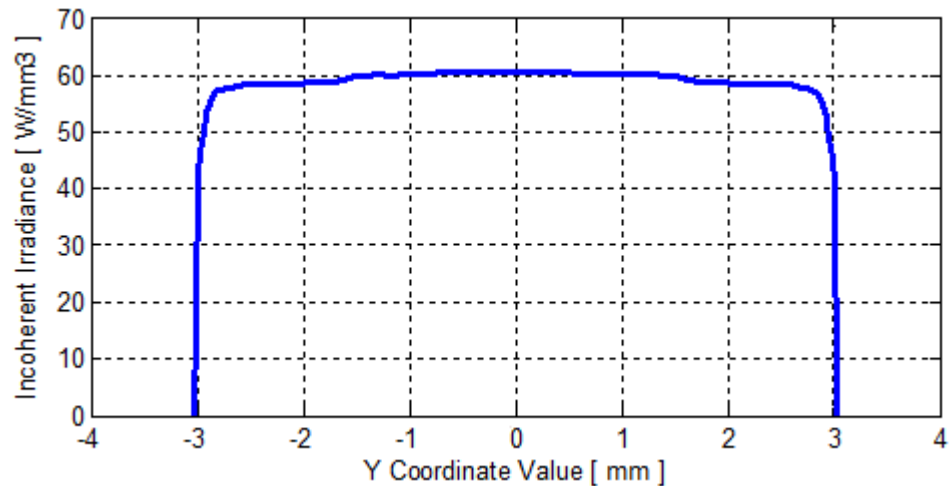
Figure 5.17: Fast-Axis Beam Profile at the Entrance Surface – The Design with the Reflectors

53
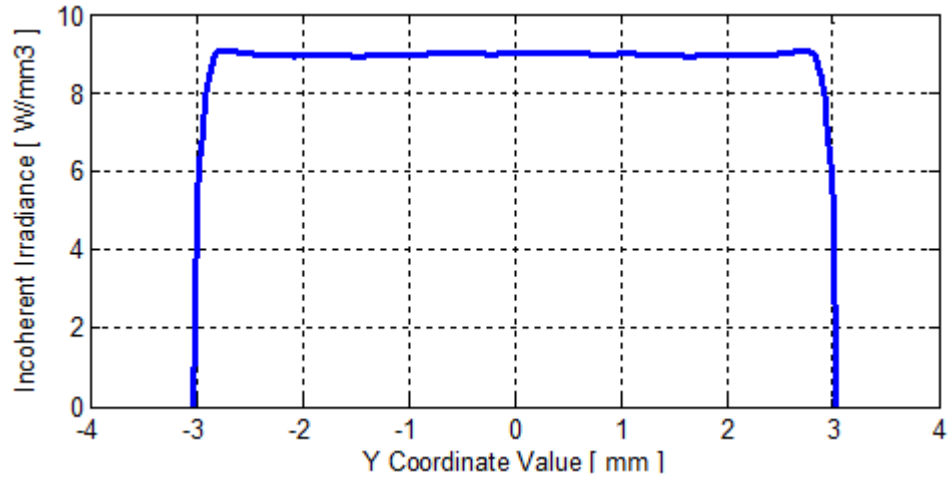
Figure 5.18: Fast-Axis Beam Profile at the Exit Surface – The Design with the Reflectors
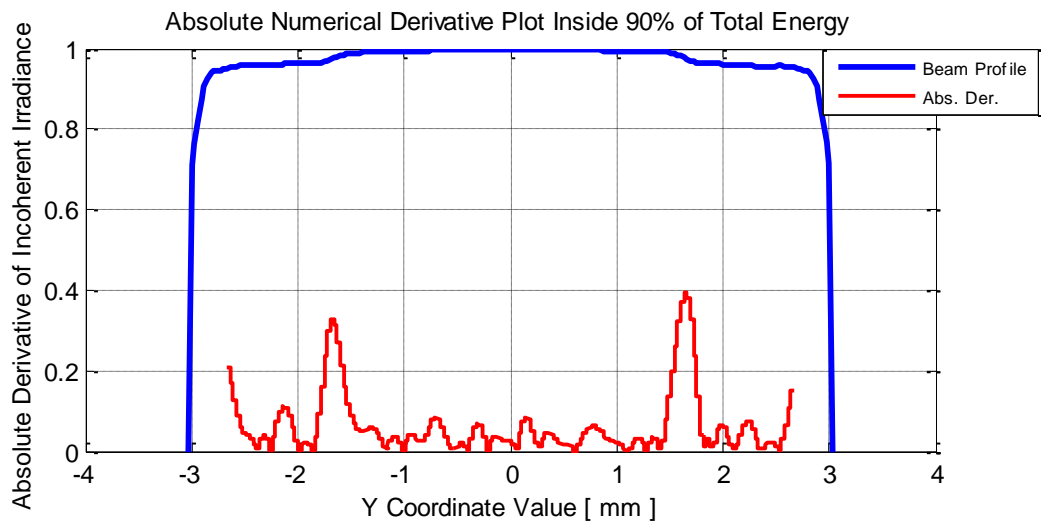
Figure 5.19: Normalized Absolute Numerical Derivative – The Design with the Reflectors
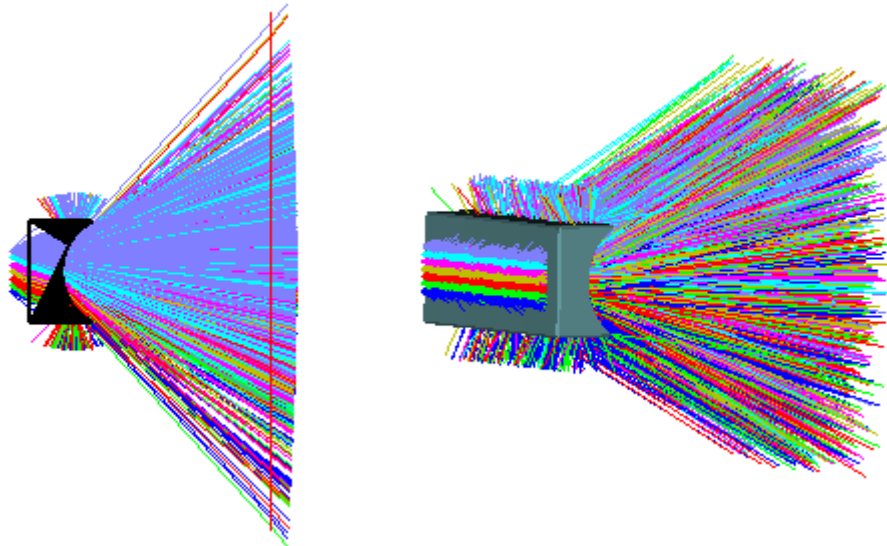
Figure 5.20: The Effect of Plano-Concave Cylindrical Lens

There were four degrees of freedom in such a design: the distance between the diode-stack and the plano-concave lens, the distance between the plano-concave lens and the gain medium, center thickness of the cylindrical lens, radius of curvature of the concave surface of the cylindrical lens. The

radius of curvature of the first surface of the lens was chosen to be planar in order to loosen mechanical tolerances of the lens. Then the system was optimized by varying these degrees of freedom with the merits of maximum transmission to the gain medium and maximum uniformity across the gain medium. After optimization and tolerance analysis of the system, the focal length of the lens was found to be -6.4mm, the center thickness of the lens was found to be 2mm, the distance between the diode-stack and cylindrical lens was found to be at least 1mm and the distance between the diode-stack and the gain medium was found to be at least 11mm (See Figure 5.25). The distance between the lens and the crystal was derived according to the decenter tolerance of the diode-stack. The decenter tolerance of the diode-stack was defined to be 200μm with which the uniform pump profile is conserved across the crystal.
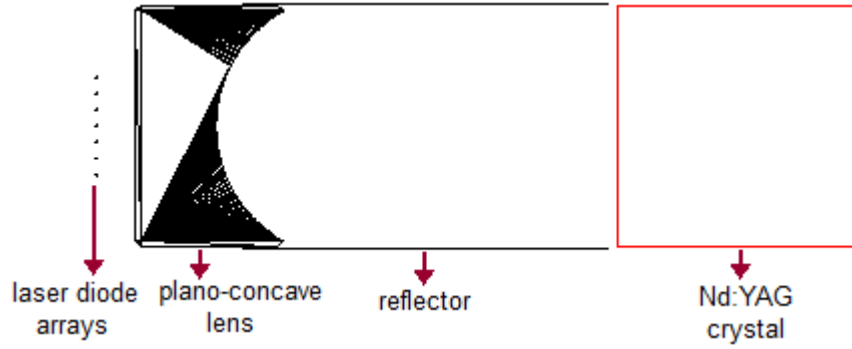
Figure 5.21: 2D Layout of the Design with the Reflectors and the Plano-Concave Lens
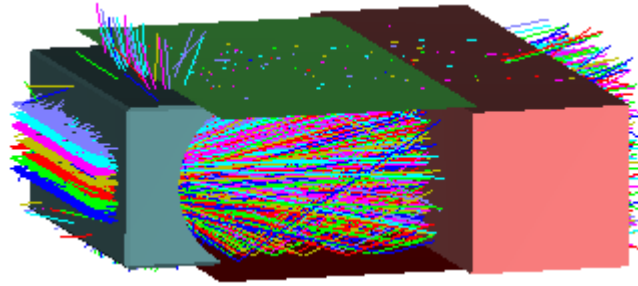
Figure 5.22: Shaded Model of the Design with the Reflectors and the Plano-Concave Lens

The resultant fast-axis beam profile at the entrance surface of the gain medium is given in Figure 5.23. It is observed that nearly top hat pump profile was obtained across the gain medium as a result of which all the dopant ions can be excited with the same pump intensity and thus the gain will be maximum. Normalized absolute numerical derivative plot inside 90% of total energy of the pump distribution at the entrance surface is given in Figure 5.24. The uniformity is found to be $\Psi = 0.061$.
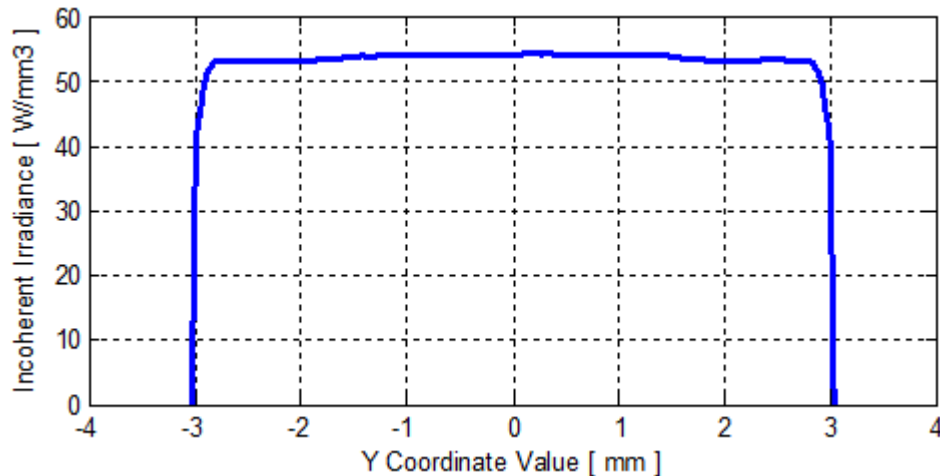
Figure 5.23: Fast-Axis Beam Profile – The Design with the Reflectors and the Plano-Concave Lens

55
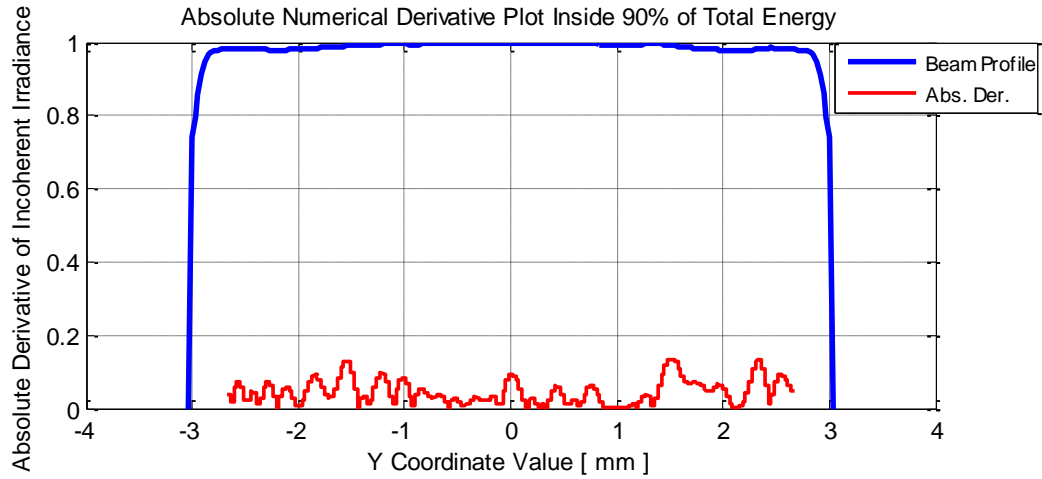
Figure 5.24: Normalized Absolute Numerical Derivative – The Design with the Reflectors and the Plano-Concave Lens

The calculated uniformity values versus the distance, d were plotted in Figure 5.25 for both configurations. The first observation is that the accepted uniformity value with d = 16mm in the design with only reflectors, given in Figure 5.20, is obtained with d = 11mm in the design with reflectors and the lens, given in Figure 5.21. There is almost 5mm gain from the distance, d with the reflectors and lens configuration. Such a distance can be very important in laser source designs, especially in military applications where available volume is very limited. The second observation is that the design with reflectors and the lens is always better in uniformity on any distance, d. However, there is a lost in pump energy because of the lens absorption and the surface reflections on the lens in spite of the anti-reflection coatings on the lens. Moreover, the lens increases the cost of the system. There is a trade-off between the gain in the volume, and the lost in energy and the cost. In this study, the pump chamber was manufactured with d = 16mm but the lens was also imported to the design in order to see its effect in uniformity and the energy lost.
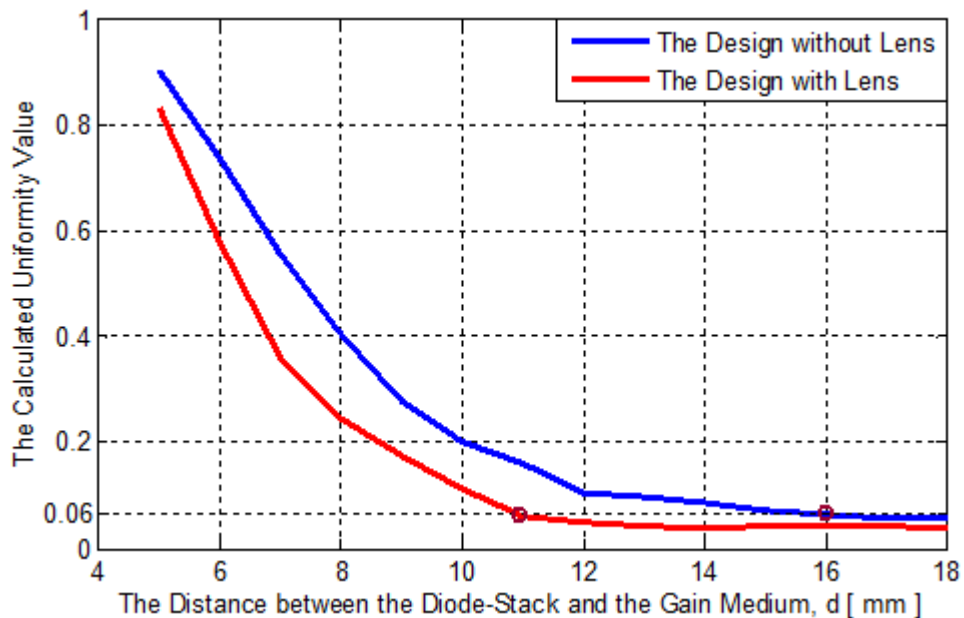
Figure 5.25: The Comparison of the Uniformity Values for the relevant two Pump Chamber Configurations – The Parallel Reflectors with and without Lens

In the designed laser source, the axial length of the pumped surface of the laser crystal is 60mm, and the crystal is pumped with 5 serially connected laser diode-stacks which have a total axial length of 50mm. The plano-concave cylindrical lens was designed with 64mm axial length. The clear aperture of the lens is 6mm, but the edge thickness of the lens increased such that the total height of the lens

has become 12mm in order to loosen mechanical mounting tolerances. Figure 5.26 shows the CAD drawings of the designed pumping chamber.

CYLINDRICAL   HR COATED   Nd:YAG
LENS   REFLECTORS   CRYSTAL
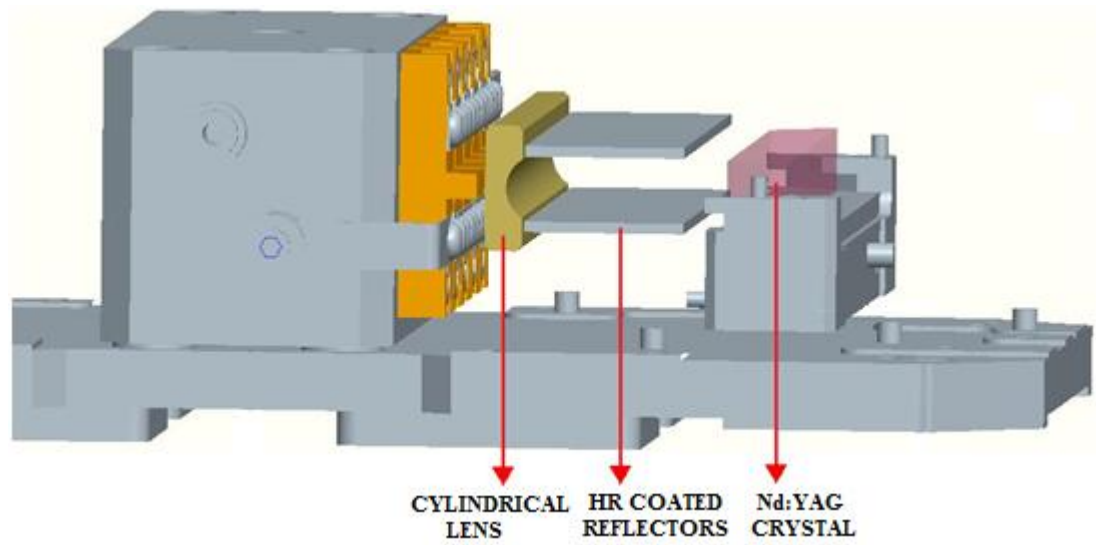
Figure 5.26: CAD Drawing of the Designed Pumping Chamber

EXPERIMENTAL EVALUATION OF THE DESIGNED PUMP CHAMBER

There should be a comparison mechanism for the designed pump chamber in order to see the improvement in thermal lens and beam divergence. To this end, a second pump chamber that is missing its transferring optical structure was utilized. That means the pump profile across the active medium was not optimized in the reference pump chamber. The reference pump chamber is given as CAD drawings in Figure 6.1. The resonator configurations of the laser sources for both pump chambers are the same.

In this design, the pump beam is directly delivered to the gain medium without a transferring optical structure. The distance between laser diode-stacks and the gain medium is 5mm by which diverged beam from the diode-stacks is almost coupled to the crystal. The Nd:YAG crystal is cooled from its top and bottom symmetrically.
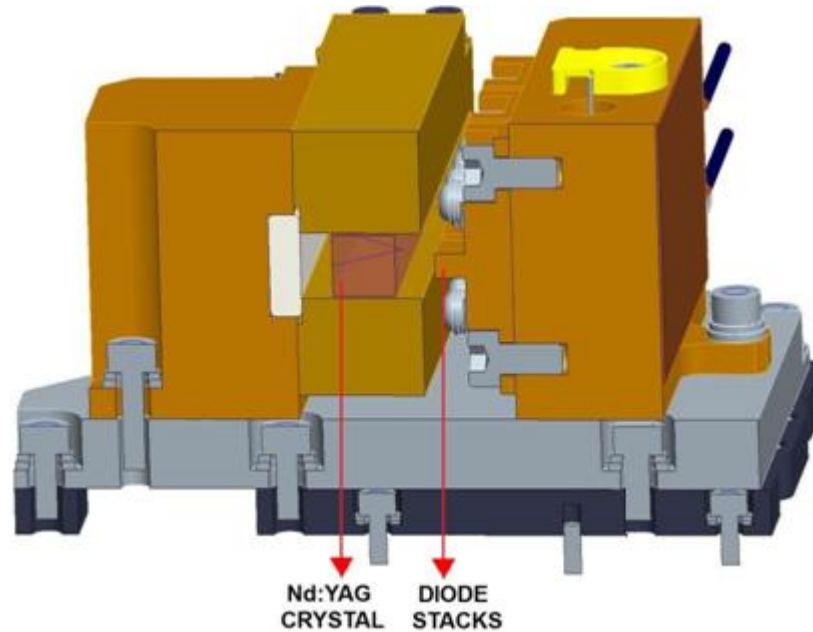
Figure 6.1: The Pumping Structure that is Missing Transferring Optical Structure

6.1. Studied Measurements for Comparing the Relevant Laser Sources

After manufacturing the mechanical and the optical parts of both laser source designs, measurements were performed in order to compare the designs and see the consistency between the computations and the measurements. First, the uniformities of the pump profiles in both designs were measured and compared. Then the improvement in far-field laser beam divergence and the wavefront distortion because of thermal lens effect were investigated.

6.1.1. Investigation of the Fast-Axis Pump Profiles in both Designs

Directed Pumping:

The fast-axis beam profiles were investigated only at the entrance surfaces of the gain medium since they keep their shapes across the gain medium. The beam profile of the reference laser source at the entrance surface of the gain medium is the beam profile of the laser diode-stack since there is not transferring optical structure in this configuration. In section 3.2.1.1 the fast-axis beam profile measurements of the same model diode-stack were carried out and in Figures 5.5 and 5.6 it is shown that the fast-axis beam profiles of the diode-stack model in ZEMAX matches perfectly with the measured ones. For this reason, the fast-axis pump profile of the reference laser source at the entrance surface of the gain medium can be obtained from ZEMAX simulation as shown in Figure 6.2 and as plotted in Figure 6.3.
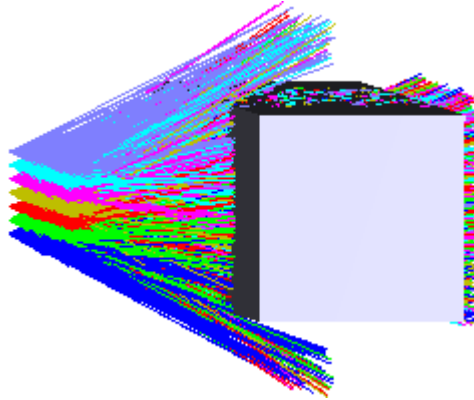
Figure 6.2: Shaded Model of the Reference Laser Source that is Used for Comparison
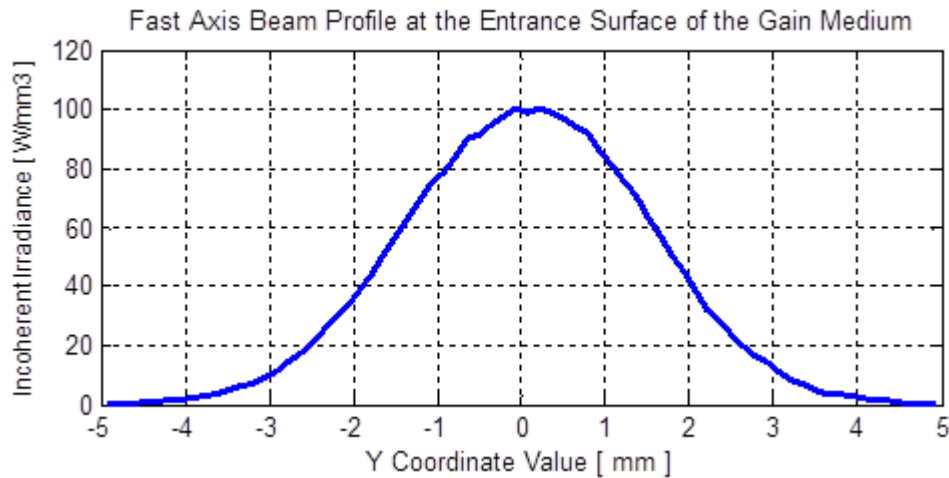
Figure 6.3: Fast Axis Beam Profile at the Entrance Surface of the Gain Medium – The Reference Laser Source

A small part of the pump is not coupled into the crystal as observed in Figure 6.2 and brings a loss that is approximately 3.8%. Normalized absolute numerical derivative inside 90% of the total energy is given in Figure 6.4 together with the normalized pump distribution. The uniformity of the given pump distribution was found to be 0.3068.

Reflector Pumping:

The pump uniformity of the designed pump chamber that is given in Figure 5.26 was investigated by means of a setup shown in Figure 6.5 and Figure 6.6. The setup was similar to the one explained in section 3.2. The same optical-fiber, PIN detector, ODE filter and the scope was used. The voltage at the position of the entrance surface of the crystal was obtained by means of the optical-fiber, the PIN

detector and the scope. At fixed positions on the z and x axes, the fast-axis was scanned using a moving stage, that has micrometer positioning sensitivity, on the y-axis.
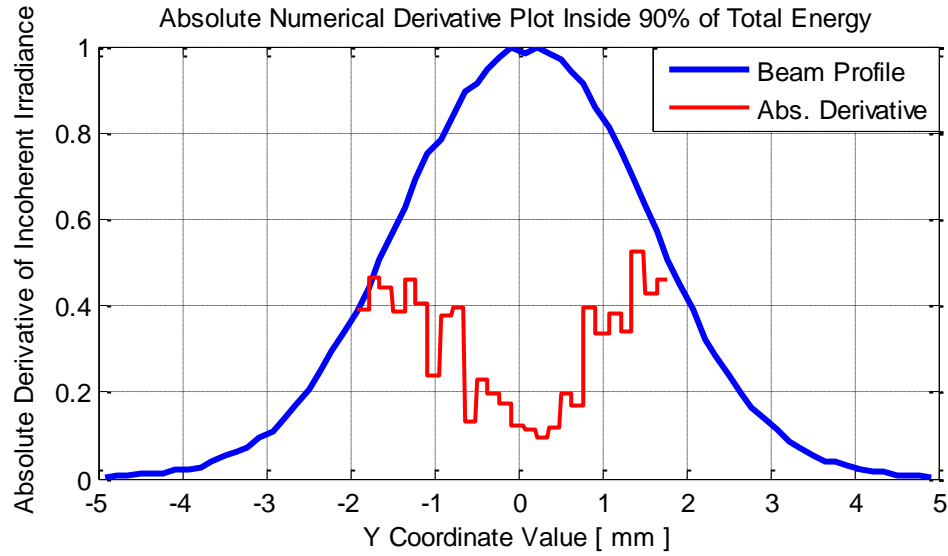
Figure 6.4: Normalized Absolute Numerical Derivative – The Reference Laser Source

Figure 6.5: The Pump-Beam Uniformity Measurement Setup for the Designed Pump Chamber – Overall View

ODE filter was used in front of the PIN detector, as shown in Figure 6.7, in order to weaken the signal that comes along with the fiber and get rid of the saturation of the detector. The detected signal voltage then read by means of the scope. The laser diode-stacks were driven with 5 Hz repetition rate, 230µs pulse duration and 43 ºC TEC temperature.
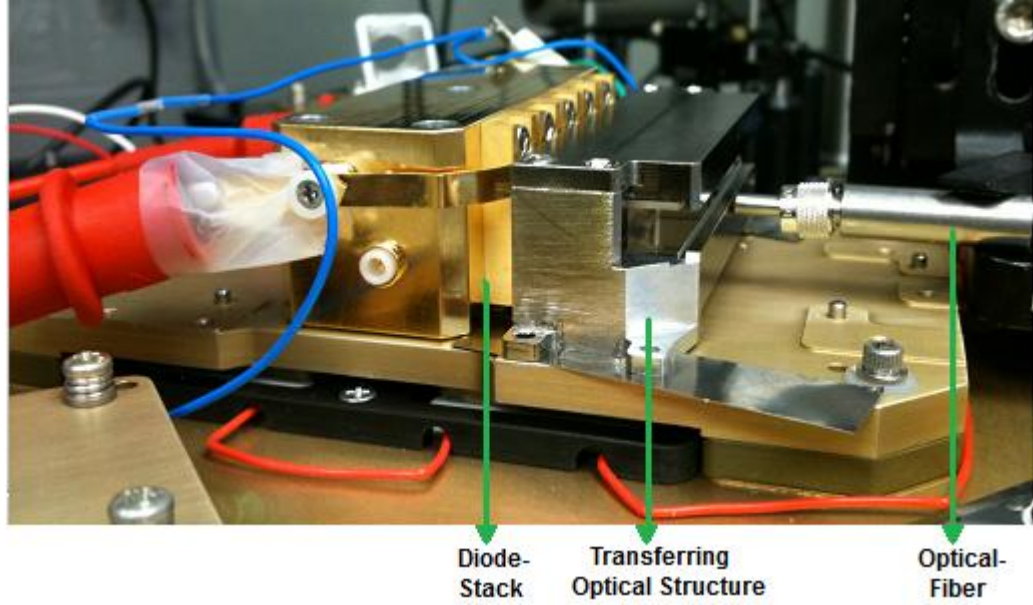
Figure 6.6: The Pump-Beam Uniformity Measurement Setup for the Designed Pump Chamber –
Pump Chamber View
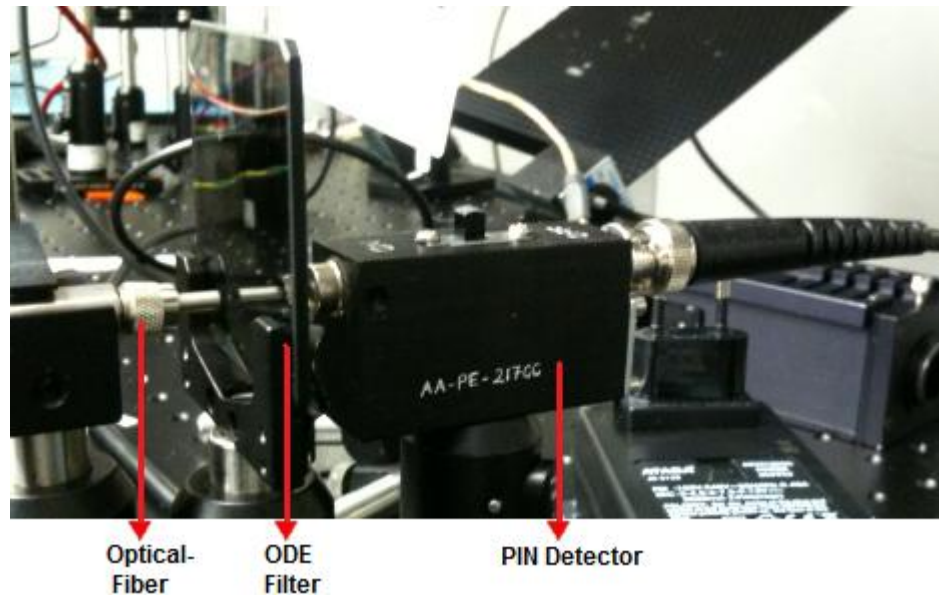
Figure 6.7: The Pump-Beam Uniformity Measurement Setup for the Designed Pump Chamber – ODE
Filter and the PIN Detector

The measurements were taken on a z-axis position where the fiber tip is at the crystal entrance surface position. On this position, it was expected that the two configurations, which are with and without plano-concave lens mentioned in chapter 5, result with almost the same uniformity value as observed from Figure 5.24. For the small "d" distances given in Figure 5.15, the design with lens will absolutely yield better uniformities. As explained before, in this study, the pump chamber was manufactured with a "d" distance that was found for the without lens configuration in order to gain from pump energy. However, the lens was also incorporated in the design in order to compare both configurations on this z-axis position to verify the simulations in chapter 5, and to use the same reflector holder structure for the future works that have small d distances.

First, the measurements were carried out without lens and then repeated with the lens. The fast-axis beam profiles were derived on two different x-axis positions in order to make sure that the beam profiles are the same along the x-axis. Then two 100μm metal shims were placed under the transferring optical structure, as shown in Figure 6.6, in order to see whether the system works with

100μm decenter tolerance of the reflector structure or the laser diode-stacks, and the fast-axis beam profile measurement was repeated. These three measurements are plotted in Figure 6.8.
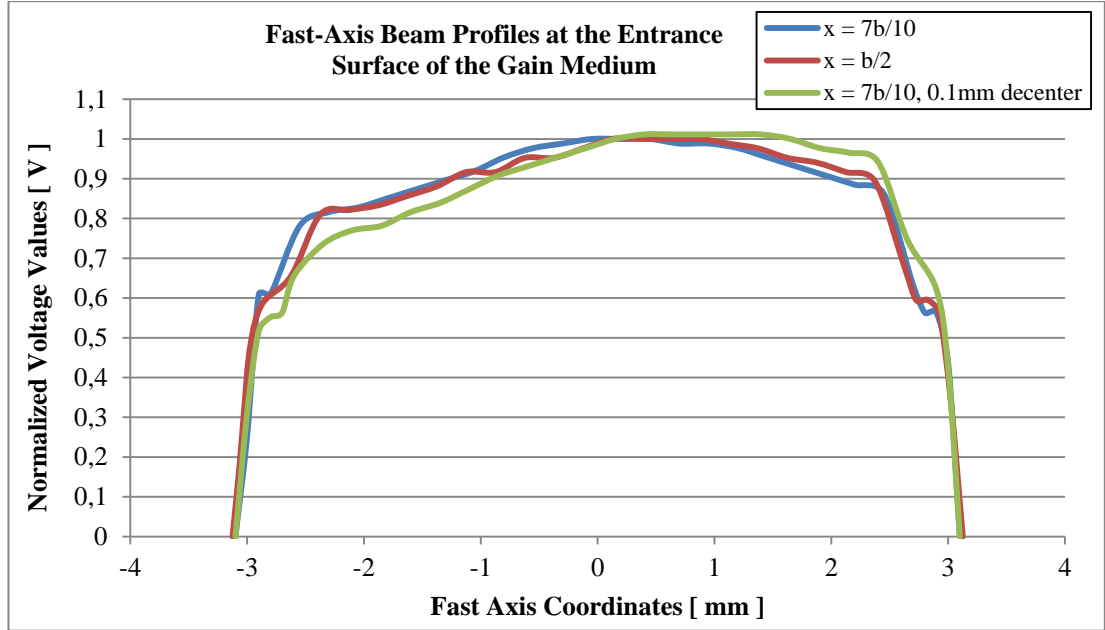
Figure 6.8: Measured Fast-Axis Beam Profiles at the Entrance Surface of the Gain Medium - The Designed Pump Chamber

As observed from the figure, the fast-axis beam profiles are the same at different x positions and with 100μm decenter of the reflectors. The beam profile is very similar to the expected theoretical one given in Figure 5.19. Only half of the beam profile, that is close to the reflector at the top side, shows a small nonuniformity as observed in Figure 6.8. The measurement was repeated with a different top reflector and it was observed that this small nonuniformity is not because of the reflector by comparing with the previous one as plotted in Figure 6.9. The reason can be the different emission powers of the diode arrays in a stack.
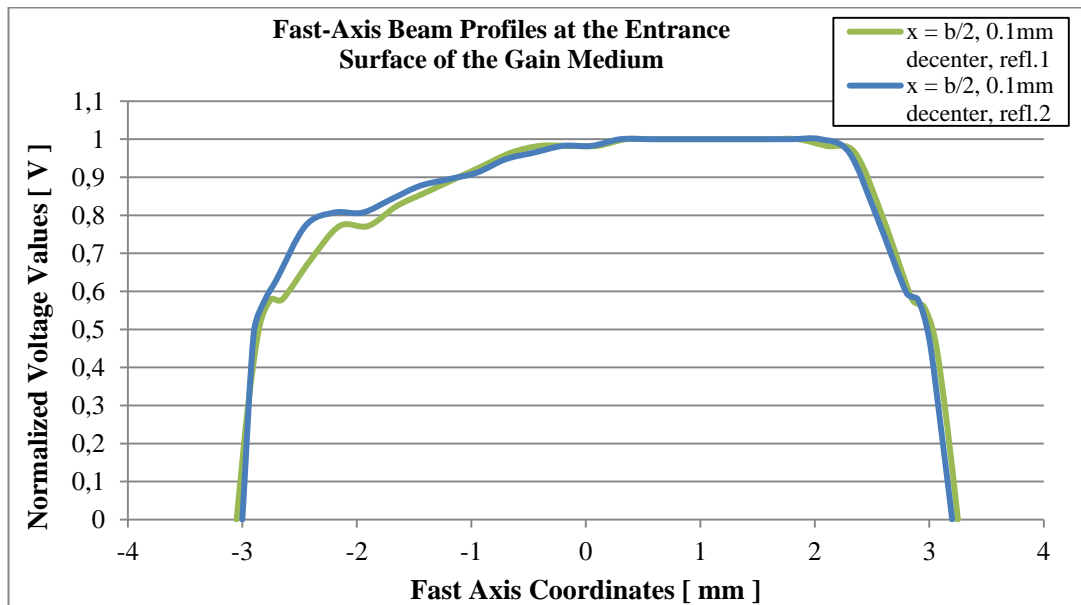
Figure 6.9: Comparison of the Fast-Axis Beam Profiles with two Different top Reflectors - The Designed Pump Chamber

The normalized absolute numerical derivative plot inside 90% of total energy of the measured pump distribution is given in Figure 6.10. The uniformity was calculated to be 0.062 by means of equation

5.1. The derived uniformity is almost the same as the theoretical one which is 0.0632 given in section 5.3. By comparing the pump-beam uniformity of the reference laser, the uniformity of the pump distribution of the designed pump chamber is almost 5 times better.

The measurements were repeated by mounting the plano-concave lens. The measured fast-axis pump profile at constant x and z axes positions was compared to the without lens configuration as plotted in Figure 6.11. It is observed from the figure that both uniformity values are almost the same on this z-axis position as expected. But indicating again, on small "d" distances on the z-axis, the configuration with lens will yield more uniform beam profiles as compared to the configuration without lens. However, the beam profiles on small distances could not be measured in this study.
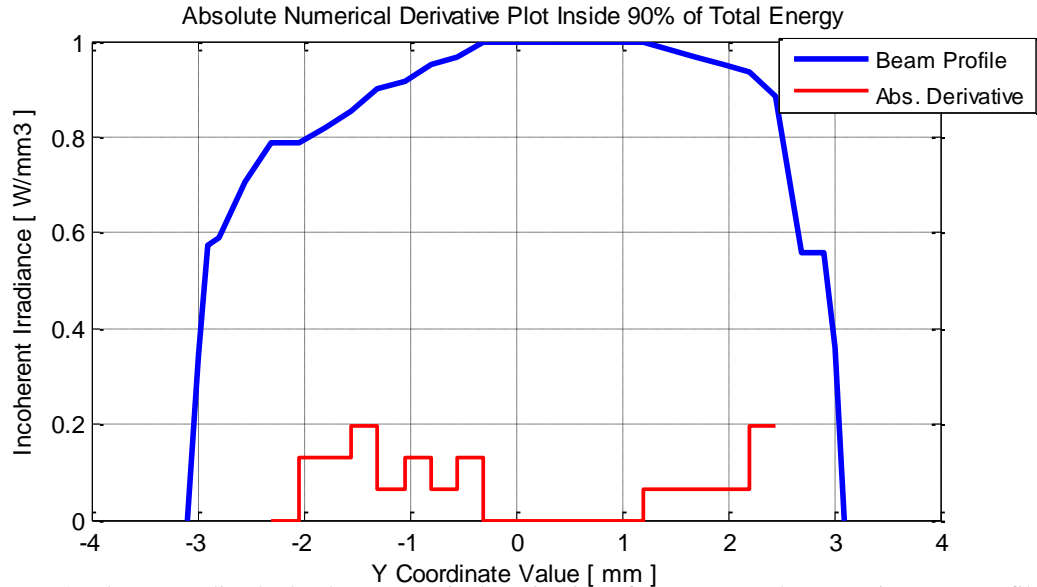
Figure 6.10: The Normalized Absolute Numerical Derivative of the Measured Fast-Axis Beam Profile - The Designed Pump Chamber
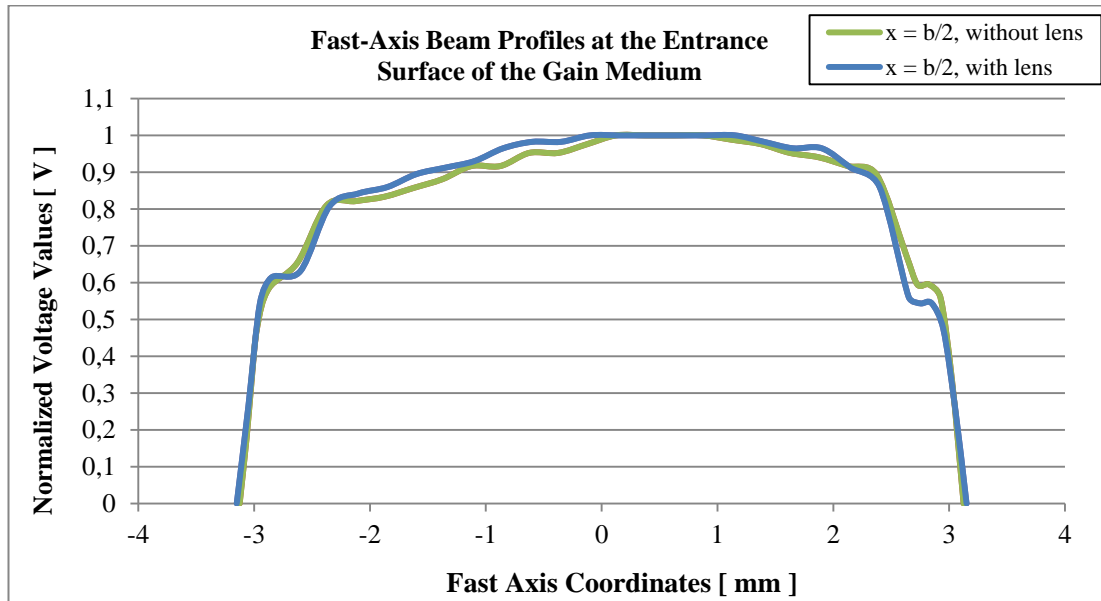
Figure 6.11: The Comparison of the Measured Fast-Axis Beam Profiles of the relevant Two Configurations, with & without Plano-Concave Lens, - The Designed Pump Chamber

There are some losses in pump energy in the designed pump chamber because of three reasons. The first loss stems from the reflections from HR reflectors that could not be manufactured with 100% reflection. In the theoretical design, there is 0.5mm opening between the HR reflectors and the crystal on the z-axis as shown in Figure 5.15 and Figure 5.21. HR reflectors were manufactured from

microscope lamelles in order to expedite the process and reduce the cost. However, in order to mounting the lamelles in the design, the relevant opening was extended to 2.5mm, as shown in Figure 6.13, which brings a loss. The third loss stems from the opening between the diode stacks and the reflector structure in the design without cylindrical lens as observed in Figure 6.12, and from the back-reflections from the concave surface of the lens in the design with cylindrical lens, as observed in Figure 6.13, although there is AR coating on the surface with ±35º angle of incidence. As mentioned before, the design was manufactured for the without lens configuration in distance, d, as given in Figure 5.15. However, the lens was also imported to the mechanical design. Thus, there is an opening, between the diode-stacks and the reflectors, by which there is a loss when removing the cylindrical lens as observed in Figure 6.12.
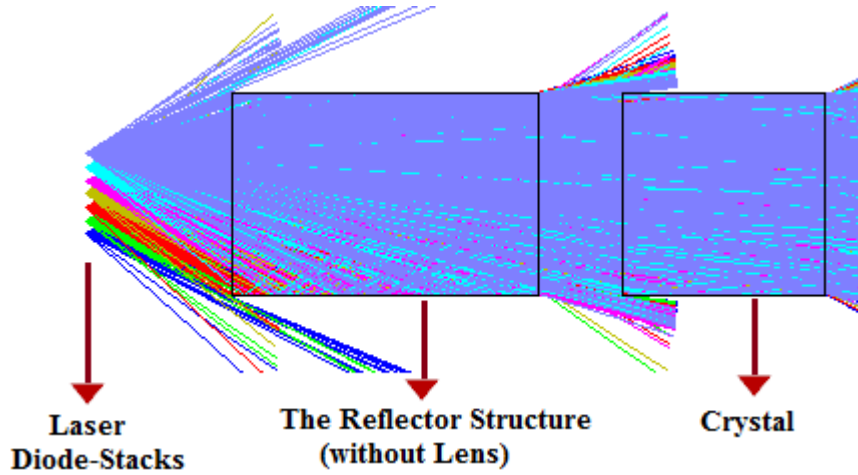
Figure 6.12: The Opening Losses in the Designed Pump Chamber without Lens

Since the design was manufactured according to the without lens configuration, mainly the results will be based on this configuration. The amount of the opening losses was derived by means of ZEMAX simulations without importing the lens. The simulation setup is given in Figure 6.14. There are four rectangular detectors by means of which total pump powers on those surfaces were obtained. The simulation results of the four detectors are given from Figure 6.15 to Figure 6.18.
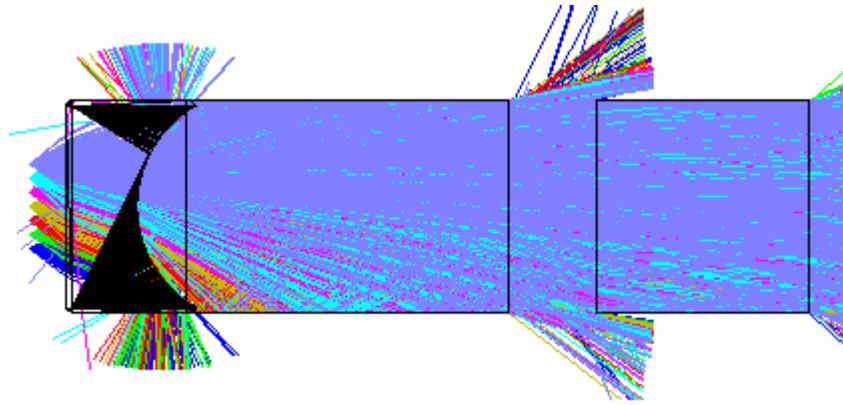
Figure 6.13: The Back Reflections from the Concave Surface of the Cylindrical Lens

65
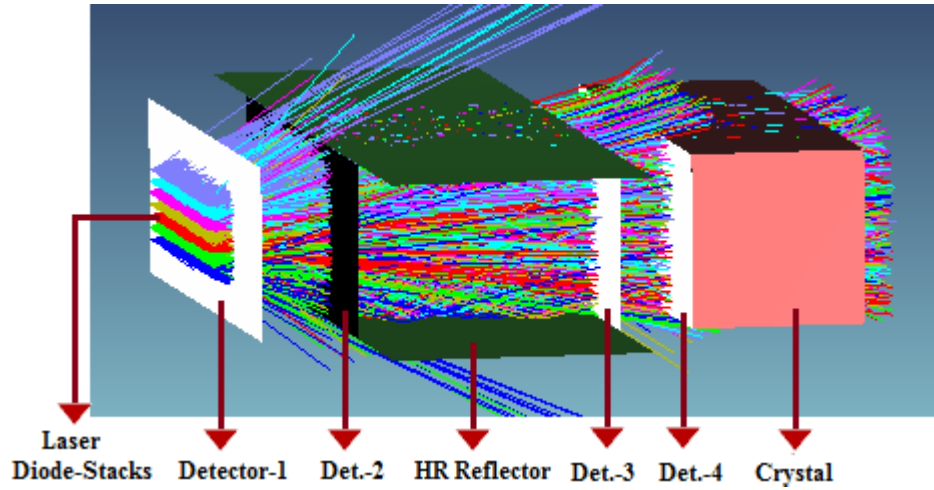
Figure 6.14: ZEMAX Simulation Setup for Deriving the Opening Losses in the Designed Pump Chamber without Cylindrical Lens

DETECTOR IMAGE: INCOHERENT IRRADIANCE

PEAK IRRADIANCE : 2.7422E+003 WATTS/CM^2
TOTAL POWER   : 7.0480E+002 WATTS
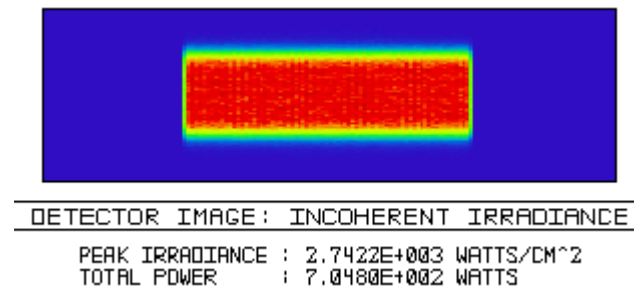
Figure 6.15: ZEMAX Simulation Result of the Detector-1, Given in Figure 6.14

DETECTOR IMAGE: INCOHERENT IRRADIANCE

PEAK IRRADIANCE : 2.3097E+003 WATTS/CM^2
TOTAL POWER   : 6.8953E+002 WATTS
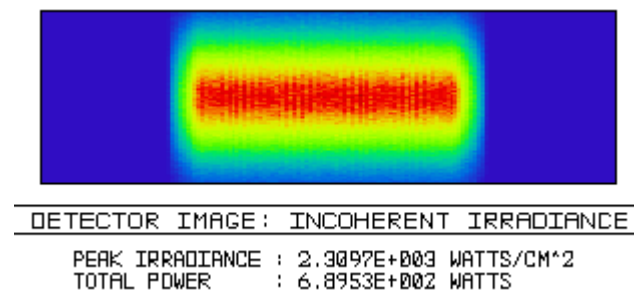
Figure 6.16: ZEMAX Simulation Result of the Detector-2, Given in Figure 6.14

DETECTOR IMAGE: INCOHERENT IRRADIANCE

PEAK IRRADIANCE : 1.2786E+003 WATTS/CM^2
TOTAL POWER   : 6.6733E+002 WATTS
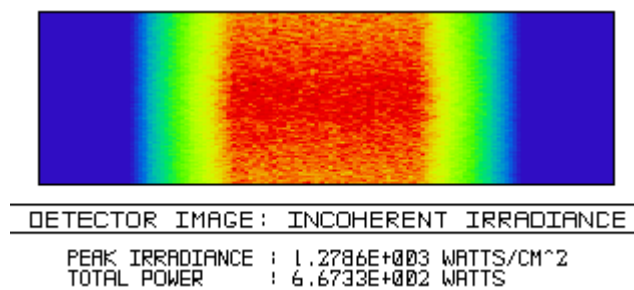
Figure 6.17: ZEMAX Simulation Result of the Detector-3, Given in Figure 6.14
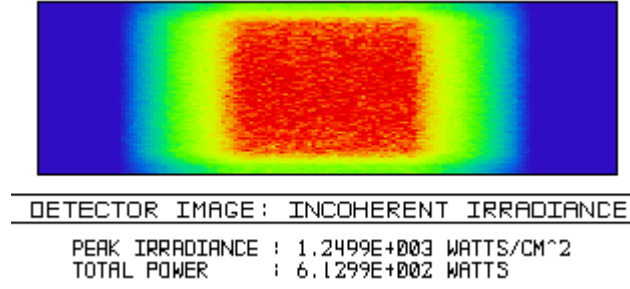
Figure 6.18: ZEMAX Simulation Result of the Detector-4, Given in Figure 6.14

The opening loss between the laser diode-stacks and the reflector structure was found by using the results of detector-1 and detector-2, i.e.:

$$Opening\ Loss\ 1 \cong \frac{705W - 689.5W}{705W} \times 100 \cong 2.2\% \tag{6.1}$$

The opening loss between the reflector structure and the crystal was found by using the results of detector-3 and detector-4, i.e.:

$$Opening\ Loss\ 2 \cong \frac{667W - 613W}{667W} \times 100 \cong 8.1\% \tag{6.2}$$

which brings a total loss 10.3% only because of the openings. There are also losses from the reflections on the HR reflectors as mentioned before. Therefore, the total loss of this pump chamber configuration will be greater than the found value. The losses in the design with cylindrical lens are not given since the AR coating on the lens could not be exactly modeled in the simulation. The total losses in both designs can be reduced by means of better overlapping mechanical structures. Note that there is one laser diode-stack in the simulations which gives the same loss values as the five diode-stacks.

6.1.2. Improvement in terms of the Far-Field Laser Beam Divergence

First, the far-field laser beam divergence of the reference laser source was investigated. The laser diode-stacks were driven with 230µs pulse duration, 20Hz repetition rate and different current values in order to observe the change in beam divergence with respect to the output energy. The TEC temperature was 43 ℃ and the output coupler reflectance was 55%. The laser beam divergence was observed at far-field, so that the laser output was focused onto a camera by means of a 1m-convex mirror. The camera was "COHU4812" model of Spiricon Inc., the energy-meter was "Lab Max Top" model and the energy-meter head was "J-50MB-YAG" model of Coherent Inc. The measured results are summarized in Table 6.1. The diode-stack current values were changed from 60A to 120A as given in the table. The relevant far-field beam-profiles are given in Appendix-D.

Table 6.1: The Reference Laser Source Far-Field Laser Beam Divergence Measurements

Applied Current [A]	Output Energy [mJ]	Y-Divergence [mrad]
60	50.6	4.3
70	85	5.1
80	121	5.6
90	160	5.9
100	200	6.2
110	240	6.3
120	281	6.5

As observed from the table, there is a dramatic increase in the fast-axis (y-axis) far-field laser beam divergence by increasing the laser diode-stack current values.

The same procedure was repeated for the laser source with the designed pump chamber. The measurements were carried out with the same resonator structure and at the same conditions. The comparison of the far-field laser beam divergences of the relevant two pump sources should be done by comparing the divergence values with the same output energies. The two configurations (with and without cylindrical lens) of the designed pump chamber yield the same results by comparing the far-field laser beam divergences at the same laser output energies. For this reason, only the results of the configuration without cylindrical lens were given in this study. The results are summarized in Table 6.2. The far-field beam profiles of the laser source are given in Appendix-E.

Table 6.2: The Laser Source with the Designed Pump Chamber - Far-Field Laser Beam Divergence Measurements

Applied Current [A]	Output Energy [mJ]	Y-Divergence [mrad]
60	25	3.1
70	50	3.7
80	78	3.9
90	108	4.2
100	139	4.4
110	170	4.8
120	200	5
130	230	5.3

The results of the far-field laser beam divergence values for both laser sources are given as a function of the laser output energies in Figure 6.19. It is observed from the figure that at the same output energy, especially on the high energies, the laser source with the designed pump chamber is 1.25 times better in the far-field beam divergence. That means the laser source with the pump chamber is 25% better than the one without pump-transferring optics in far-field beam divergence. It can be also said that the beam expander of the laser source with designed pump chamber will be 25% smaller in volume. If a polynomial is fitted to each curve as plotted in the same figure, it is observed that the curves tend to attain the lowest value at above 2.5mrad with minimum pumping. That means the theoretical limit for the far-field laser beam divergence is above 2.5mrad. Therefore the improvement in laser beam divergence is more than the found value, 25%.
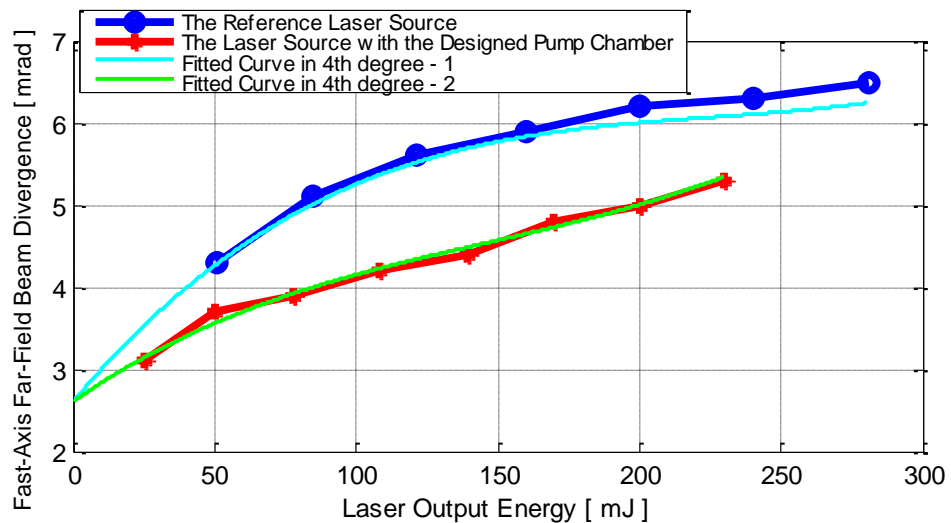
Figure 6.19: Far-Field Laser Beam Divergence versus Laser Output Energy of two Laser Sources

The far-field mode shapes of two laser sources are given from Figure 6.20 to Figure 6.23. The improvement is obvious by also observing the far-field mode shapes at the same output energies of the laser sources.
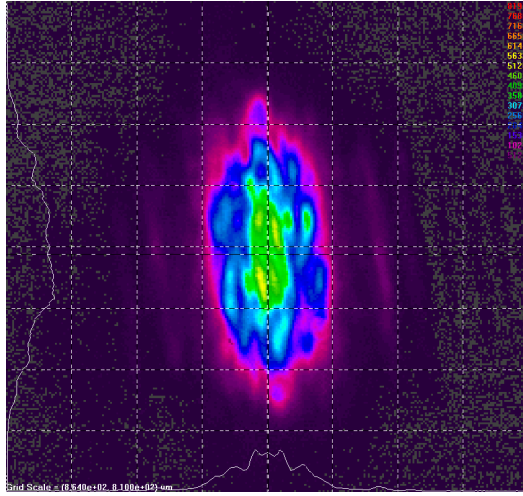
Figure 6.20: Far-Field Mode, Reference Laser Source, 50mJ Output Energy
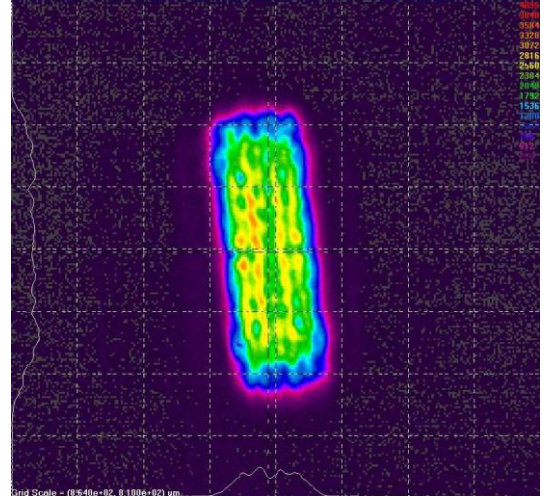
Figure 6.21: Far-Field Mode, Investigated Laser Source, 50mJ Output Energy
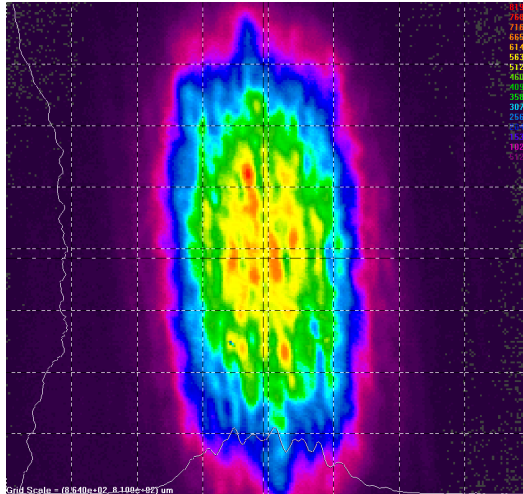
Figure 6.22: Far-Field Mode, Reference Laser Source, 200mJ Output Energy
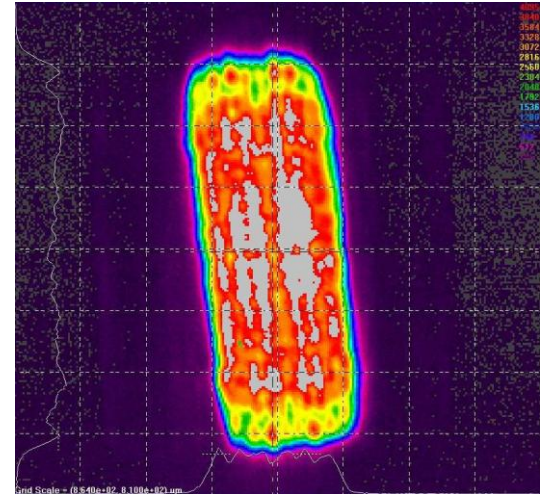
Figure 6.23: Far-Field Mode, Investigated Laser Source, 200mJ Output Energy

6.1.3. Improvement in terms of the Wavefront Distortion on the Laser Beam

The generated thermal lens because of nonuniform thermal profile inside the laser crystal distorts the wavefront of the laser beam. In this study, the wavefront distortion was investigated in terms of the fast-axis laser beam radius. The objective was observing the effect of pumping profile to the generated thermal lens inside the crystal. To this end, a He-Ne laser beam in 633nm was passed through the crystal while pumping continues and without a resonator configuration. So that the laser beam radius is also the thermal lens radius generated inside the crystal. The output He-Ne beam that emerged from the crystal was observed by means of a wavefront analyzer to derive the beam radius with a setup given in Figure 1.11.

First, the pump chamber of the reference laser source was investigated in terms of generated thermal lens inside the crystal. The crystal was pumped with 5 serially-connected laser diode-stacks as indicated before. The diode-stacks were driven with 20Hz repetition rate, 230μs pulse width, at 43ºC TEC temperature. The laser beam radius values were obtained as a function of the current values that the diode-stacks driven with. The setup of the measurement is given in Figure 6.24. The wavefront

69

analyzer is "SID4 – 4 wave shearing interferometer device" of Phasics Inc. company. 1.5 ODE filter was placed in front of the wavefront analyzer to get rid of saturation.
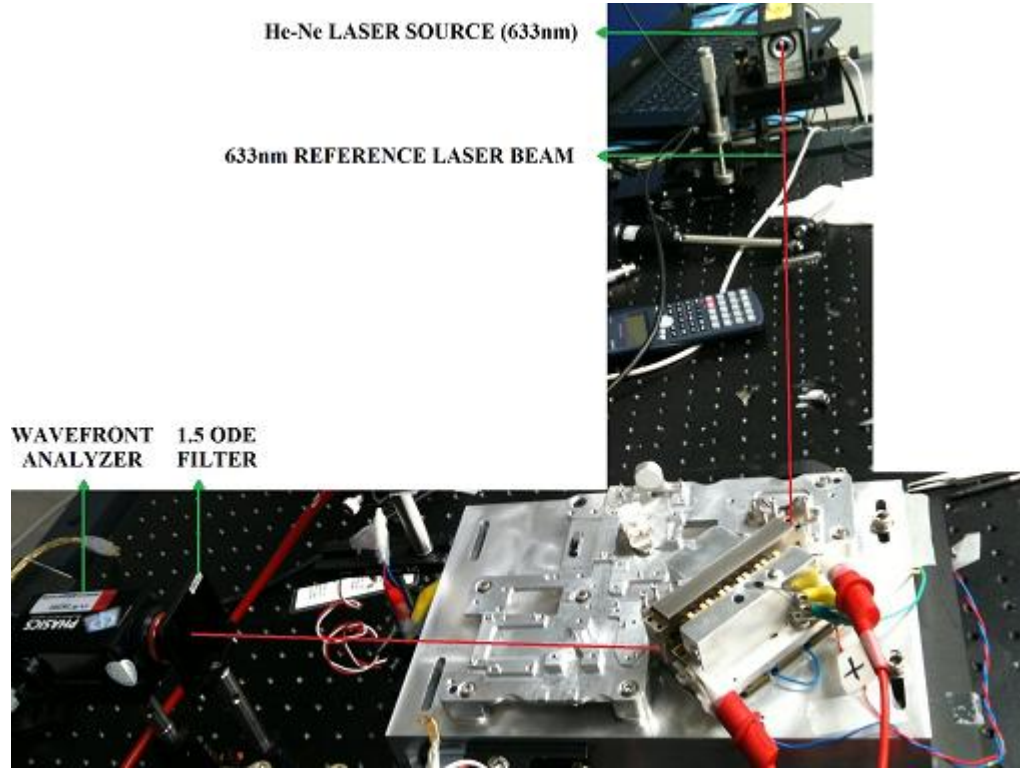
Figure 6.24: Laser Beam Distortion (Radius) Measurement Setup – The Reference Laser Source

After that, the designed pump chamber was investigated in terms of generated thermal lens inside the crystal at the same conditions as given in Figure 6.25. Again a He-Ne beam was passed through the crystal while pumping continues, and the wavefront distortion in terms of laser beam radius as a result of the formed thermal lens inside the crystal was observed by means of the wavefront analyzer. The measurement was carried out for two configurations (with and without cylindrical lens) of the designed pump chamber.

At least 4 laser beam radius values were taken with each diode-stack current value in all the measurement setups. Then the average laser beam radius was calculated for a diode current value. The resulting laser beam radius values of the relevant two laser sources should be compared with the same heat load inside the crystal. However, since there are pump losses in the designed pump chamber, the same diode-stack current values of the laser sources cannot form the same heat loads inside the crystal. Moreover, the heat load inside the crystal cannot be measured. A more realistic approach is the comparison of the laser beam radius values of the laser sources at the same output energies that were obtained with the resonator structure in section 6.1.2. Figure 6.26 shows the measured laser beam radius values of the two laser sources as a function of the output laser energies of the resonator structures. There is average 0.9m improvement in measured radius of curvature, namely in thermal lens, when comparing at the same output energies. In other words, the difference between the curves at the same output energy shows the improvement in laser beam quality. The results of the designed pump chamber configurations (with and without cylindrical lens) were the same, therefore only the results of the design without lens were given.
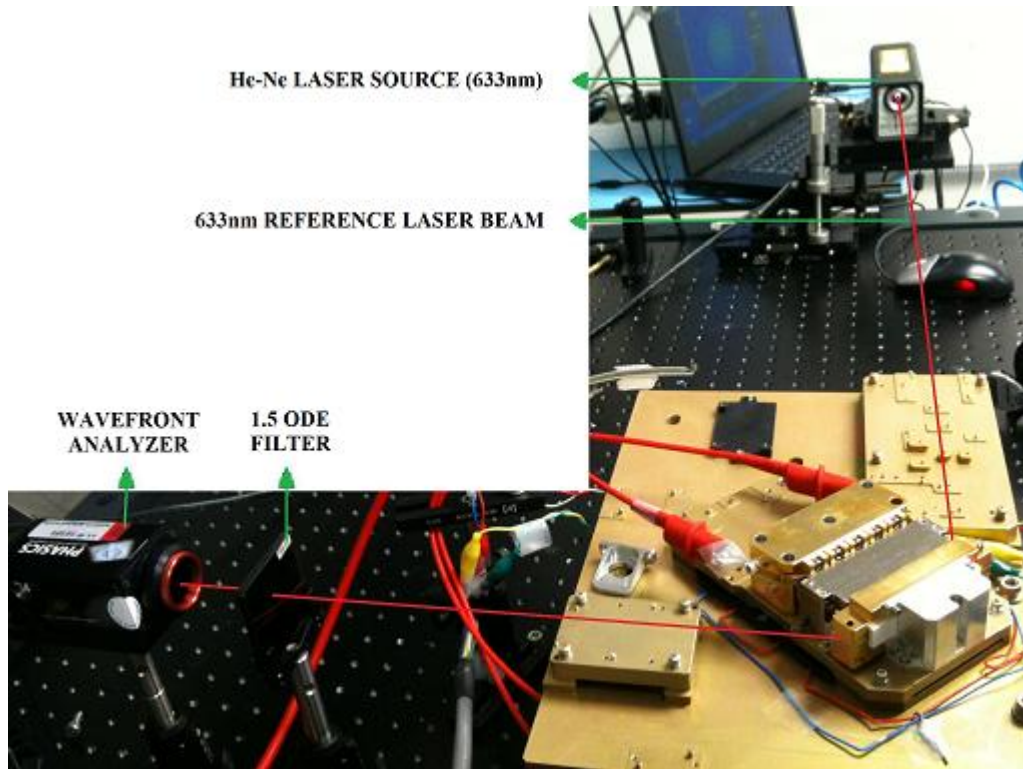
Figure 6.25: Laser Beam Distortion (Radius) Measurement Setup – The Laser Source with the Designed Pump Chamber
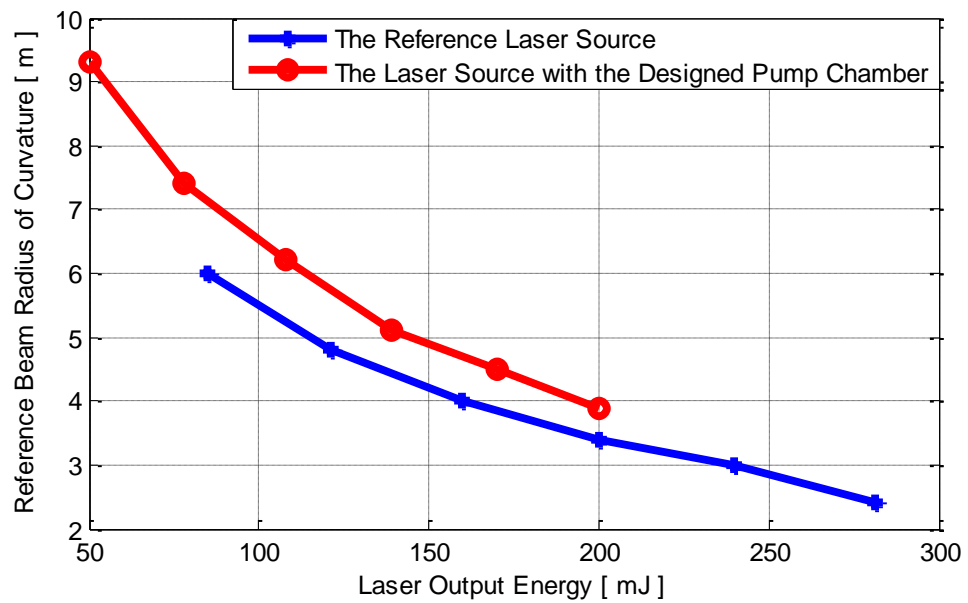

Figure 6.26: Measured Laser Beam Radius Values versus the Laser Output Energies with the Resonator Structures of the Laser Sources

CHAPTER 7

DISCUSSIONS AND CONCLUSIONS

7.1. Summary and Conclusions

In this study, a method for computer aided pump chamber design in diode-pumped solid-state lasers was developed. The design criteria and the objective of the study was the maximum laser beam quality and the system efficiency with reduced thermal lens effect formed in the gain medium. The investigated method includes numerical and analytical computations, and also empirical measurements. The amount of generated thermal lens inside the laser crystal was obtained and then its negative effects were reduced by optimizing the pump profile across the crystal by means of a pump chamber design, while keeping the system efficiency at a desired level. The computations and the measurements are carried out for the fast-axis (y-axis) since the thermal lens forms on this axis. 1.1% doped Nd:YAG crystal was used as the gain medium throughout the study.

The first step in pump chamber design was the characterization of laser diode-stacks that were used as the pump sources. In the computer aided pump chamber design, the designer needs to know the divergence angles of the pump source in the horizontal and the vertical axes. The fast-axis beam profiles should be also known for deriving the thermal loading coefficient in order to calculate the amount of generated heat inside the crystal.

For the diode characterization, a beam scanning method using an optical fiber was developed. The method was verified by comparing the scanned beam profile of a single diode-emitter by the optical fiber with the recorded one by means of a CCD camera. Then the method was utilized in characterization of laser diode-stacks which were used as the pump source. The slow-axis and the fast-axis beam profiles were obtained as a function of repetition rate (5Hz, 10Hz, 20Hz) and the diode-stack input currents (80A, 100A, 120A) at a constant position. It's observed that the beam profiles were independent from the repetition rate and diode-stack input current. Then the slow-axis beam profiles were derived with respect to the optical-fiber position on the pump axis (z-axis) in order to compute the beam divergence. The beam divergence on the slow-axis was found to be 8.23º by using the measured beam widths. The same procedure was repeated for the fast-axis and the beam divergence on the fast-axis was calculated to be 27.23º. Finally, the percentage absorption was derived as a function of temperature values of the laser diode-stack in order to know the optimum working temperature of the diode-stack with respect to the absorption band of Nd:YAG crystal.

After the characterization of laser diode-stack, thermal loading coefficient, that gives the generated heat from the absorbed pump power, was calculated. By the knowledge of this coefficient, temperature distribution across the crystal, the refractive index profile by means of dn/dT effect and the laser beam divergence can be calculated. The dimensions of Nd:YAG crystal was 70mm x 5mm x 12mm on the x, y, z axes, respectively. The computation consists of two steps. In the first step, the crystal was pumped with a diode-stack that kept a temperature of 45 ºC and driven with 230µs pulse duration, 100A current. The temperature distribution of the crystal cross section per uniform time intervals were recorded by means of a thermal camera as thermographic data with 10 Hz and 20 Hz repetition rates. Then using previously measured beam profiles and the near field beam divergence of the diode-stack, the absorbed beam profiles inside the crystal were calculated. In the second step, by importing these absorbance profiles into FLUENT software, the temperature distribution across the crystal was simulated by CFD method and each with different thermal loading coefficient. The

thermal loading coefficient values were changed from 0.3 to 0.4 since the reported values are between in this range. After each simulation, the derived temperature distributions across the crystal per unit time intervals were compared to the measured one. The procedure was iteratively repeated until obtaining the best match between the measured and the simulated temperature distributions. As a result, thermal loading coefficient was found to be 0.39. By the accomplishment of this part, the temperature distribution, the refractive index profile, wavefront distortion and the laser beam divergence could be calculated for any known pump profile across the gain medium.

After the computation of thermal loading coefficient, the optimum temperature distribution and the relevant pump profile that result with the desired beam quality and system efficiency could be calculated. Then a computer aided pump chamber design was carried out with the objective of obtaining the desired pump profile. The optimum pump profile is the one that results in a uniform fast-axis temperature distribution across the crystal in order to eliminate the thermal lens effect. However, the pump chamber which yields the pump profile for such a uniform temperature distribution was going to be a complicated and probably an expensive design. It was seen that obtaining a uniform pump profile across the gain medium also yields the desired beam quality and the system efficiency theoretically. For this reason, in this study, the objective of the computer aided pump chamber design was obtaining a uniform top hat pump profile across the crystal. The design was studied in ZEMAX by trying three different configurations by optimizing each configuration for the merit of the given objective. The comparison of the configurations was carried out by the resulting pump uniformities across the crystal. In the final design, the emitted pump beams from the laser diode-stacks was first diverged by a plano-concave lens to interfere each other and transferred to the gain medium by two parallel mirrors. The plano-concave lens was used to obtain the uniform pump profile in a small distance, that was called "d", between the diode stacks and the crystal. It was found that the uniform pump profile was obtained in a distance, d = 11mm, by using the plano-concave lens. The same uniformity without using the lens was obtained in a distance, d = 16mm. There is 5mm difference which is very important in laser source designs to reduce the total volume. But the lens brings extra cost and the lost in pump energy the amount of which could not be foreseen in advance. In this study, the distance d was chosen for the design without the lens and the HR reflectors were produced by coating the microcope lamelles. However, the lens was also imported in the mechanical design in order to obtain total loss stems from the lens and to observe whether there was a difference between the pump profiles of both configurations on the crystal entrance surface to verify the simulations.

After the manufacturing of the laser source with the designed pump chamber was completed, the laser source was compared with another reference laser source, of which resonator structure is the same, in order to observe the improvement. The comparison was carried out for the pump uniformity across the gain medium, laser beam divergence at the far-field and the wavefront distortion in terms of laser beam radius. In beam uniformity measurements, it was seen that the pump profile of the design pump chamber across the crystal was five times more uniform than the one of the reference laser source. The improvement in beam divergence was found to be 25%. Thus it can be said that the beam expander, that will be designed to reduce the beam divergence at the output of the laser source, will be 25% smaller in volume. The derivation of the improvement in laser beam quality was carried out by measuring the laser beam radius by means of a wavefront analyzer. The comparison of the laser beam radius values should be done for the same heat loads inside the crystals of both laser sources. However, there are some losses in the designed pump chamber and therefore the same current values of the diode-stacks of both laser sources cannot yield the same heat load inside the crystal. For this reason, the improvement in the laser wavefront was carried out by comparing the measured radius of curvature values at the same output energies that were measured in previous step with the resonator structure. There is approximately 0.9m difference in radius of curvature, which can also be called thermal lens radius, of the laser sources at the same output energy levels of the relevant resonator structures.

In conclusion, a pump chamber that minimizes thermo-optical distortions by reducing the generated thermal lens inside the crystal, and maximizes the system efficiency by obtaining a top hat pump profile was designed. The formed thermal lens inside the crystal was reduced by optimizing the pump profile by a computer aided pump chamber design. The system efficiency was maximized by pumping the gain medium with a uniform top hat beam profile by means of which the gain profile across the crystal was maximized. The designed pump chamber was manufactured, tested and compared with a

reference laser source in order to observe the improvements in the most crucial parameters for a laser source, namely the pump uniformity, laser beam divergence and the laser beam quality.

7.2. Recommendations

All the tools and instruments that were used in the measurements throughout this study were chosen as the present ones in the laboratories. There was not any mechanical measurement setup that was manufactured in order to increase the accuracy. In laser diode-stack characterization, the calculated pump divergence values between two different intervals were expected to be the same. But it was not the case, although the differences in pump divergence angles were small. For solving this problem, a more precise measurement setup with an optical-fiber that has smaller core diameter may be manufactured for the future works in order increase accuracy. Also more data may be taken in small intervals especially on the fast-axis. Thus a more accurate beam profiles can be achieved for the computation of thermal loading coefficient and for the pump-beam divergence calculation in order to import the source model in computer aided pump chamber design.

In the thermal loading coefficient computation, there was approximately 1 °C temperature difference between the time dependent measured and simulated plots. In order to reduce this difference, the previously derived fast-axis beam profiles may be measured more accurately. Moreover, the setup that was used in the measurements could not be exactly modeled in the CFD simulations. For instance, the measurements were carried out in a clean room there was an air flow that may affect the generated heat distribution inside the crystal. In order to get rid of such effects, the measurements may be executed in more controlled conditions.

In the pump chamber design, the gain medium was pumped with five serially connected laser diode-stacks. Although the diode-stacks are of the same model, there may be a small difference in their beam divergence and the emitted power in their diode-arrays. But in diode characterization step, only one of the diode-stacks was characterized, and the imported pump source properties in ZEMAX belong to this diode-stack. This may create a change in the simulations and optimization of the pump chamber. Characterization of all the diodes and importing their properties into ZEMAX may yield more accurate designs.

The heat sink structure of the designed pump chamber was the same as the one of the reference laser source in order to observe the improvement by pumping the gain medium with a top hat pump profile. And as mentioned before, the HR reflectors were manufactured by coating microscope lamelles, that were present in the laboratory, in order to expedite the manufacturing process. Because of using the mentioned heat sink structure and mounting tolerances of the HR reflectors, there were 2.5mm opening between the reflectors and the crystal in pumping axis. This opening brings approximately 8.1% loss in pump energy.

The design was manufactured for the configuration without cylindrical lens. However, the lens was also imported to the design and as a result, when removing the lens there occurs an opening between the reflector structure and the diode stacks. This opening causes an extra 2.2% loss in pump energy. In future designs, the configuration of the design should be fixed in advance, i.e. with or without lens according to the desired distance between the diode-stacks and the crystal. Thus the mentioned openings will be closed.

Moreover, the lamelles were not coated in a precision manner and there were scratches on the coatings which bring losses in again pump energy. In the future works, such high reflector materials may be produced with precision coatings. By reducing the explained losses in pump energy, since the gain profile across the crystal is uniform by means of uniform pumping, the laser output energy will be greater as compared to the direct pumping of the gain medium besides the improvements in thermal lens, laser beam divergence and the beam quality.

REFERENCES

[1]   U.S. Patent 3,353,115

[2]   Koechner, W., Bass, M., "Solid-State Lasers: A Graduate Text", Springer, p.1, 2003

[3]   http://www.photonics.com/edu/Handbook.aspx?AID=25099, Last Visited in 28 December 2012

[4]   S.Biswal, J.Nees, G.Mourou, "A simple technique to remove thermal distortions in pulsed solid-state lasers", OSA TOPS, Vol.10, 1997

[5]   Makki, S., Leger, J., "Solid-State Laser Resonators with Diffractive Optic Thermal Aberration Correction", IEEE Journal of Quantum Electronics, Vol.35, No.7, p.1075, 1999

[6]   Ofitserov, E. N., "Investigation of the Thermo-Optical Distortions in the Active Element and of Quality of Generated Radiation of the Axially-Diode Pumped Solid State Laser", CAOL 2005, p.234

[7]   Nishida, Y., Yamanaka, M., "Development of a Two-Dimensional Birefringence Distribution Measurement System in Laser-Diode Pumped Solid-State Laser Material", American Ins. of Phys. - Review of Scientific Instruments, Vol.72, Iss.5, p.2387-2391, 2009

[8]   Lyashedko A.D., Bufetova, G.A., "Thermo-Optical Distortions in a Nd: YAG Slab With a Zigzag Beam Propagation", CLEO 2011, p.1

[9]   Payne, S., Beach, R., Bibeau, C., Ebbers, C., "Diode Arrays, Crystals, and Thermal Management for Solid-State Lasers", IEEE Journal of Quantum Electronics, Vol.3, No.1, p.71, 1997

[10]   T.Y.Fan, "Heat Generation in Nd:YAG and Yb:YAG", IEEE Journal of Quantum Electronics, Vol.29, No.6, p.1457-1459, 1993

[11]   T.S.Chen, V.L.Anderson, O.Kahan, "Measurements of Heating and Energy Storage in Diode-Pumped Nd:YAG", IEEE Journal of Quantum Electronics, Vol.26, No.1, p.6-8, 1990

[12]   A.Sennaroglu, "Experimental determination of fractional thermal loading in an operating diode-pumped Nd:YVO minilaser at 1064nm", Applied Optics, Vol.38, No.15, p.3253-3257, 1999

[13]   J.Meng, W.Chen, X.Hou, Q.Hu, "Comparison of different side-pumping configurations for high power laser diode pumped solid-state laser", Chinese Optics Letters, Vol.1, No.9, p.538-540, 2003

[14]   Shuichi, F., Furuta, K., Yasui, K., "Highly Efficient and High Quality Beam Generation of a Diode-Stacks-Pumped Nd:YAG Rod Laser", CLEO 2001, p.422

[15]   Hou, J., Wang, S., "Modeling of Efficiency and Uniformity of Different Pumping Structures of Slab Lasers", SOPO 2009, p.1-3

[16]   Koshel, R.J., Walmsley, I.A., "Optimal Design of Optically Side-Pumped Lasers", IEEE Journal of Quantum Electronics, Vol.33, No.1, p.94, 1997

[17]   http://www.rp-photonics.com/lasers.html, Last Visited in 28 December 2012

[18] Koechner, W., Bass, M., "Solid-State Lasers: A Graduate Text", Springer, p.59, 2003

[19] Thirumaleshwar, M., "Fundamentals of Heat & Mass Transfer", Pearson Education, 2nd Edition, p.43, 2006

[20] Jacinto., C., "Thermal lens and heat generation of Nd:YAG lasers operating at 1.064 and 1.34 μm", Optics Express, Vol.16, No:9, 2008

[21] Koike, A., Sugimoto, N., "Temperature Dependences of Optical Path Length in Inorganic Glasses", Reports Res. Lab. Asahi Glass Co. Ltd., p.56, 2006

[22] Phasics Inc., "4-wave Shearing Interferometer Device – SID4 Software User Handbook", p.126.

[23] VLOC Inc., http://www.vloc.com/PDFs/YAGBrochure.pdf, Last Visited in 28 December 2012

[24] Coherent Inc., http://www.coherent.com/Products/index.cfm?343/Single-Emitter-Diode-Lasers, Last Visited in 15 January 2013

[25] Trager, F., "Springer Handbook of Lasers and Optics of Lasers", Springer, p.638

[26] Svelto, O., Hanna, D., "Principles of Lasers", Springer, 4th Edition, p.584, 1998

APPENDIX A

THE FAST-AXIS BEAM PROFILE MEASUREMENTS OF THE LASER DIODE-STACK THAT USED IN THE STUDY
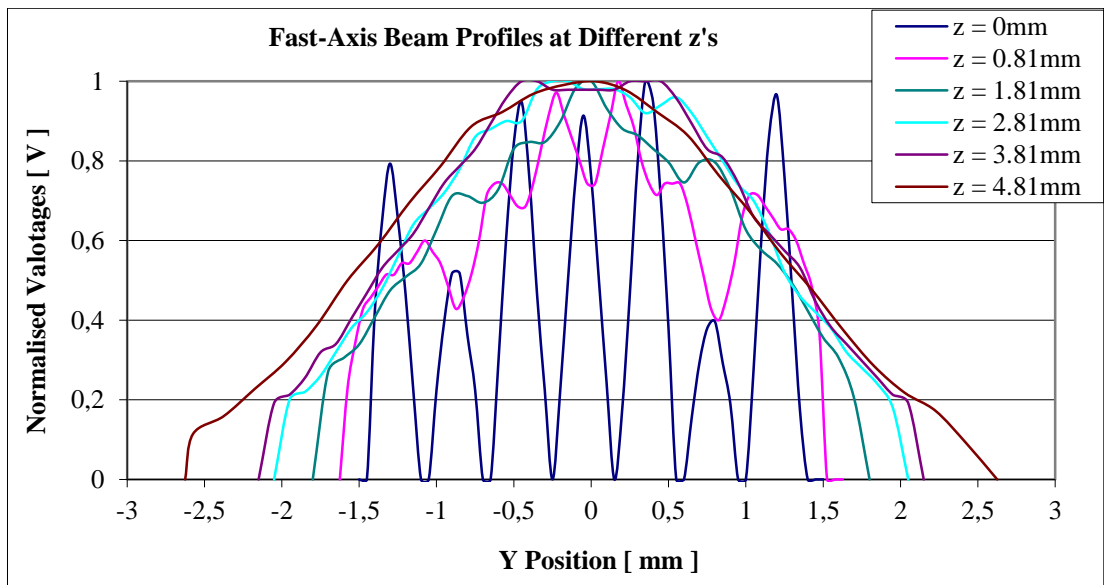
Figure A.1: Normalized Fast-Axis Beam Profiles vs. Optical Fiber Positions, 0 - 4.81mm
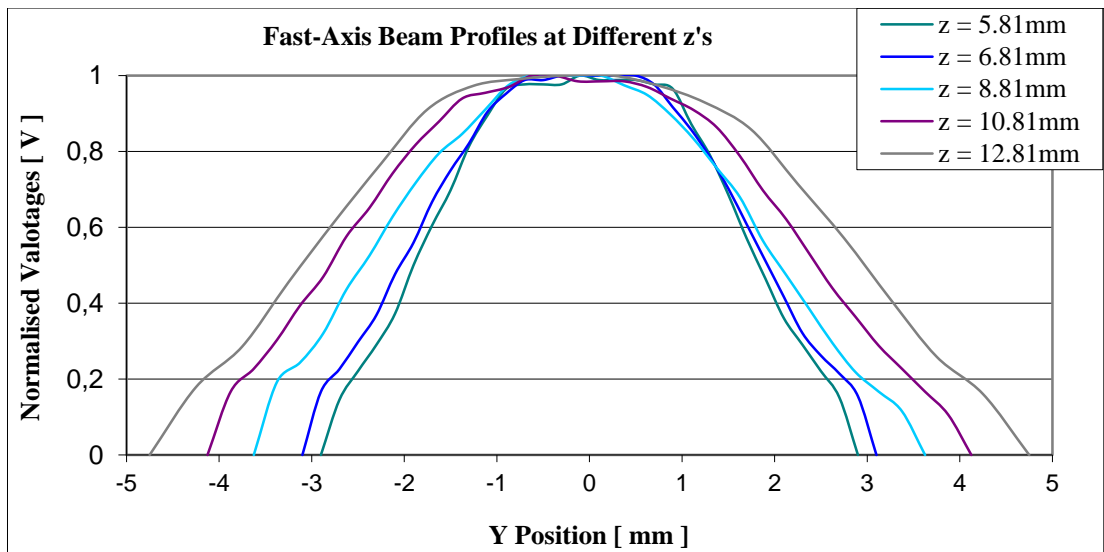
Figure A.2: Normalized Fast-Axis Beam Profiles vs. Optical Fiber Positions, 5.81 - 12.81mm

APPENDIX B

GLAD SOURCE CODE FOR THE FAR-FIELD DIVERGENCE CALCULATION IN UNIFORM PUMPING CASE

```
write/off
nbeam 1
array/set 1 256*2
wavelength/set 1 1.064

macro/define lenses/overwrite
        prop 30 1
         lens 1 f_lens
        prop 35 1
macro/end

f_lens = 762
r_beam = 0.3
C ***********
 gaussian/cir/res 1 100 r_beam
 macro/run lenses/4

c ****** divergence calculation *******
focal_length = 100
lens 1 focal_length
prop focal_length 1

encircled/level 1 0.9
variables/set/parameter spot_radius 1 fitencir
divergence= atan(spot_radius/focal_length)
full_divergence_mrad =2*divergence/1e-3
plot/watch focus.plt
plot/l 1 xrad=spot_radius*2 nslice=1024

write/on
C
C  beam divergence with 90 percent encircled energy
C
full_divergence_mrad =
C
```

GLAD SOURCE CODE FOR THE FAR-FIELD DIVERGENCE CALCULATION IN NONUNIFORM PUMPING CASE

```
write/off
nbeam 1
array/set 1 256*2
wavelength/set 1 1.064

macro/define lenses/overwrite
        prop 30 1
          lens 1 f_lens
        prop 35 1
macro/end

f_lens = 435
r_beam = 0.3
C ***********
 gaussian/cir/res 1 100 r_beam
 macro/run lenses/4

c ****** divergence calculation *******
focal_length = 100
lens 1 focal_length
prop focal_length 1

encircled/level 1 0.9
variables/set/parameter spot_radius 1 fitencir
divergence= atan(spot_radius/focal_length)
full_divergence_mrad =2*divergence/1e-3
plot/watch focus.plt
plot/l 1 xrad=spot_radius*2 nslice=1024

write/on
C
C  beam divergence with 90 percent encircled energy
C
full_divergence_mrad =
C
```

APPENDIX D

REFERENCE PUMP CHAMBER FAR-FIELD MODE SHAPES
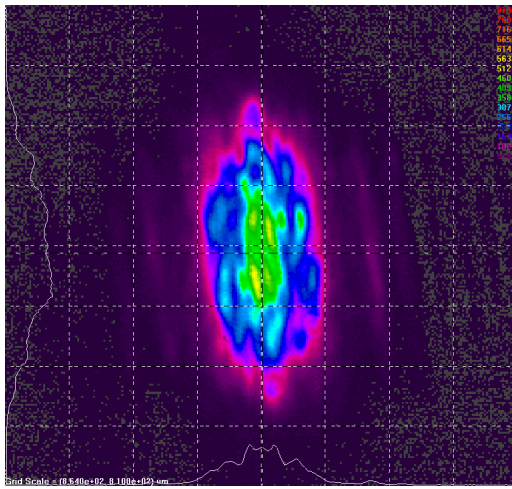
Figure D.1: Reference Laser Source,
60A Far-Field Laser Beam Divergence
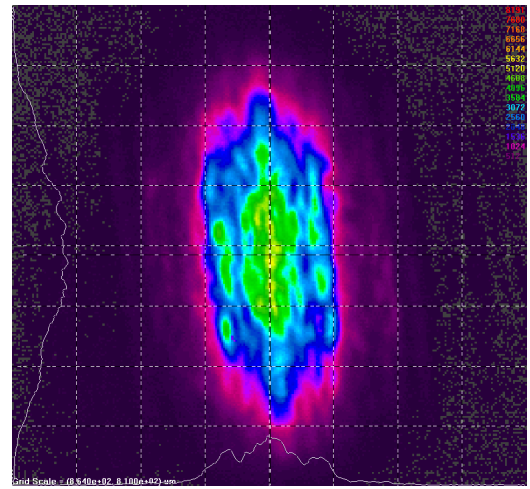
Figure D.2: Reference Laser Source,
70A Far-Field Laser Beam Divergence
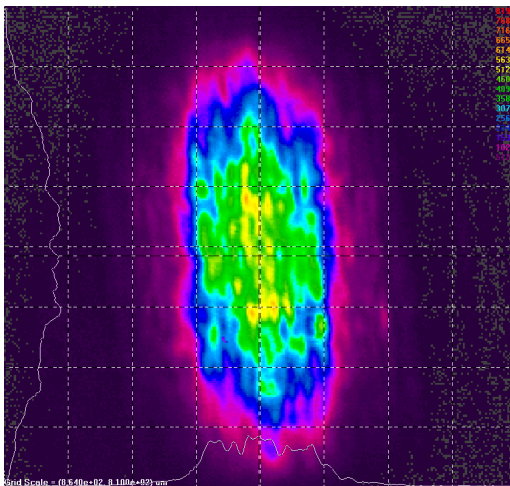
Figure D.3: Reference Laser Source,
80A Far-Field Laser Beam Divergence
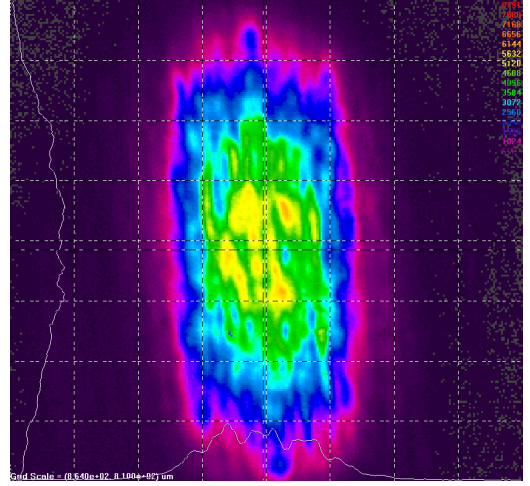
Figure D.4: Reference Laser Source,
90A Far-Field Laser Beam Divergence
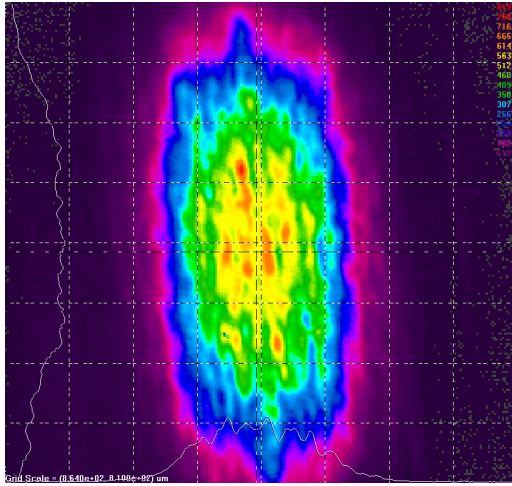
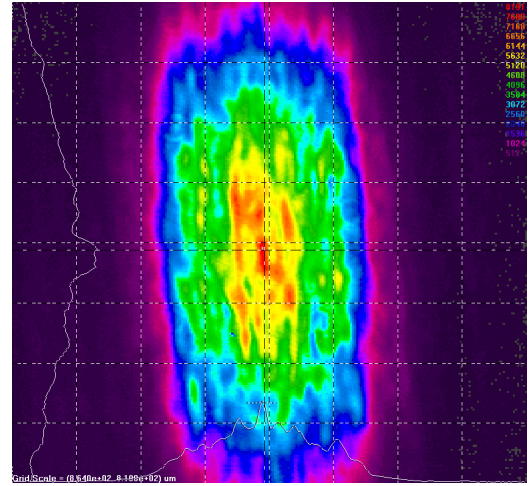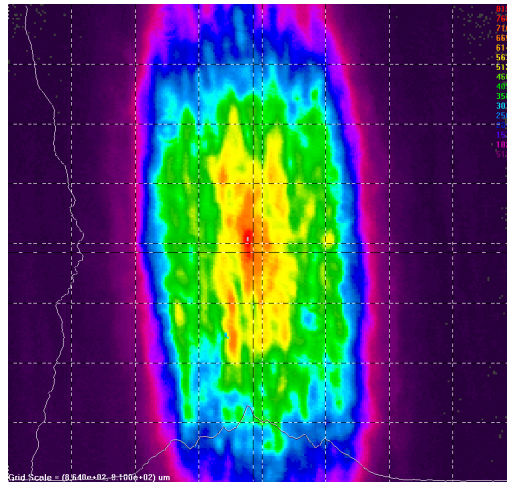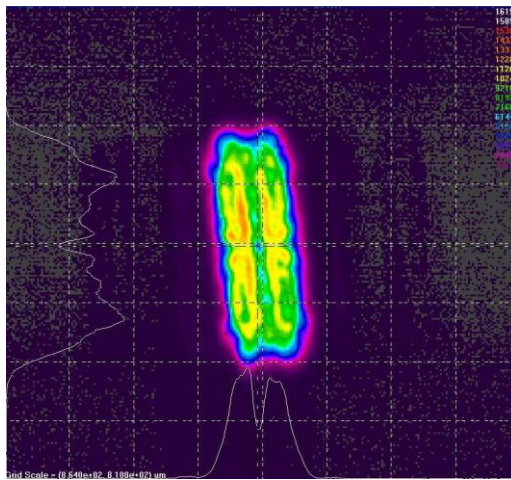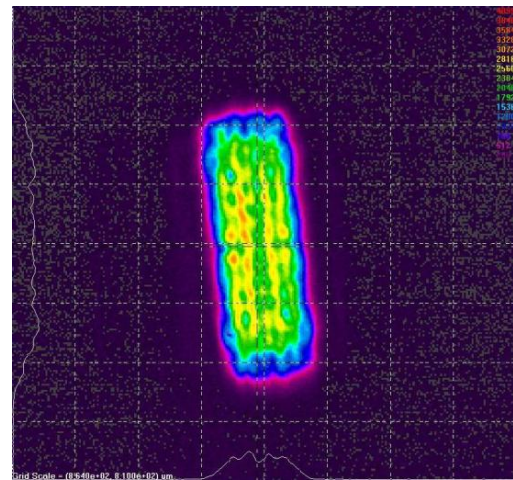Figure D.5: Reference Laser Source,
100A Far-Field Laser Beam Divergence

Figure D.6: Reference Laser Source,
110A Far-Field Laser Beam Divergence

Figure D.7: Reference Laser Source, 120A Far-Field Laser Beam Divergence

APPENDIX E

DESIGNED PUMP CHAMBER FAR-FIELD MODE SHAPES

Figure E.1: Investigated Laser Source,
60A Far-Field Laser Beam Divergence

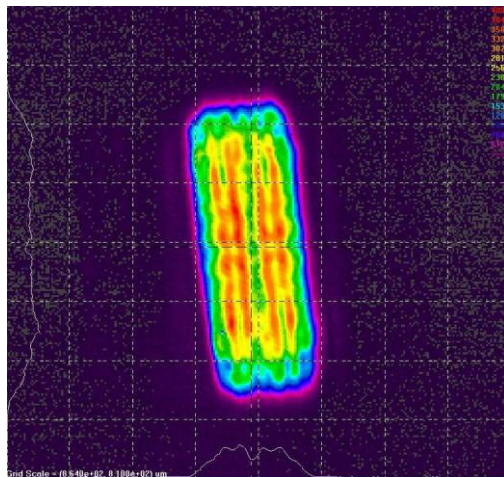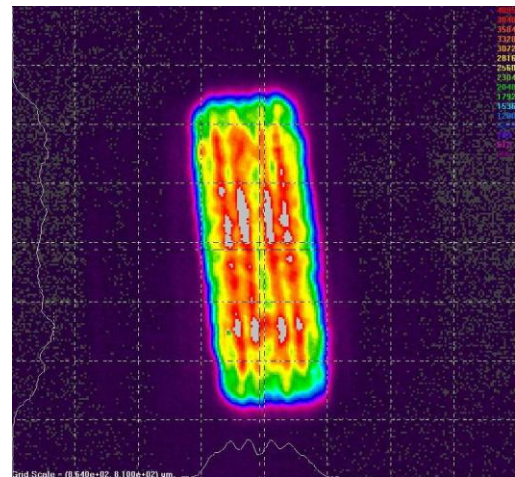Figure E.2: Investigated Laser Source,
70A Far-Field Laser Beam Divergence

Figure E.3: Investigated Laser Source,
80A Far-Field Laser Beam Divergence

Figure E.4: Investigated Laser Source,
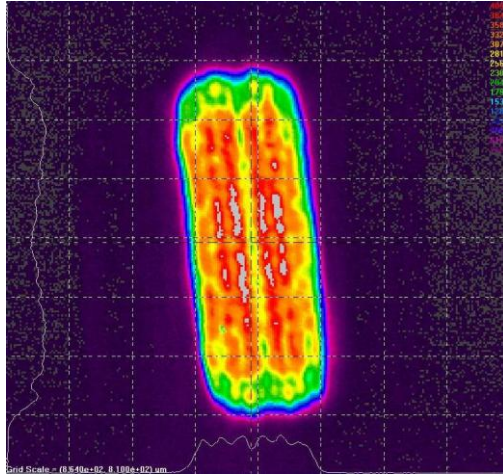90A Far-Field Laser Beam Divergence

Figure E.5: Investigated Laser Source,
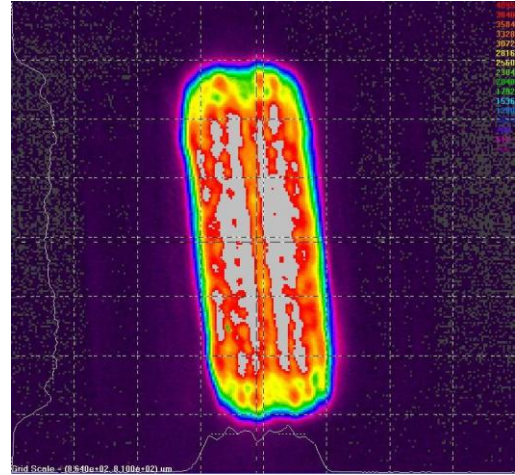100A Far-Field Laser Beam Divergence

Figure E.6: Investigated Laser Source,
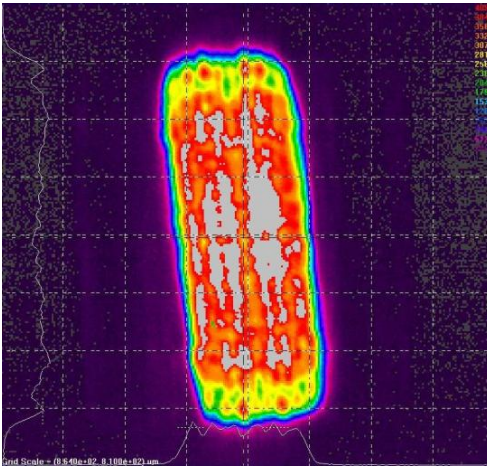110A Far-Field Laser Beam Divergence

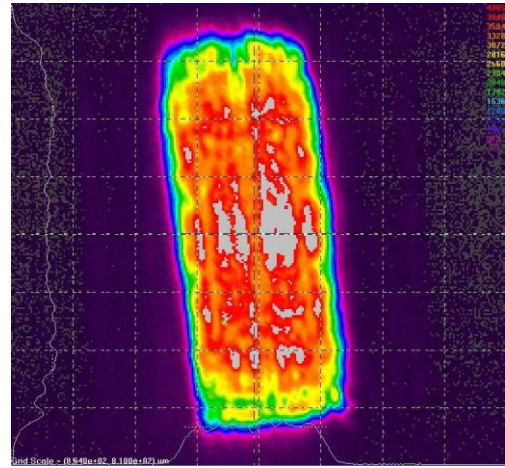Figure E.7: Investigated Laser Source,
120A Far-Field Laser Beam Divergence

Figure E.8: Investigated Laser Source,
130A Far-Field Laser Beam Divergence